Master of Science Thesis

Integral boundary layer analysis of vortex generator induced flow on a flat plate

Ashok Kumar Nedumaran

May 2, 2016

Faculty of Aerospace Engineering · Delft University of Technology

Integral boundary layer analysis of vortex generator induced flow on a flat plate

Master of Science Thesis

For obtaining the degree of Master of Science in
Aerospace Engineering at Delft University of Technology and in
Engineering Wind Energy at Technical University of Denmark.

Ashok Kumar Nedumaran

May 2, 2016

European Wind Energy Master - EWEM
DUWIND - Delft University of Technology
DTU Wind Energy, - Denmark Technical University

European Wind Energy Master - EWEM
Of
Rotordesign Track

The undersigned hereby certify that they have read and recommend to the Delft University of Technology, Department of Wind Energy and Technical University of Denmark, Department of Wind Energy for acceptance a thesis entitled **"Integral boundary layer analysis of vortex generator induced flow on a flat plate"** by **Ashok Kumar Nedumaran** in partial fulfillment of the requirements for the degree of **Master of Science**.

Dated: May 2, 2016

Supervisor: _____
dr.ir. Carlos Simão Ferreira of Delft University of Technology

Supervisor: _____
ir. Daniel Baldacchino of Delft University of Technology

Supervisor: _____
dr.ir. Néstor Ramos García of Denmark Technical University

Summary

Vortex generators (VGs) are flow control devices commonly applied in wind turbine blades, among other applications. A significant advance in the design of wind turbine blades would be the integration of vortex generators in the aerofoil optimisation process. Currently, aerofoil optimisation relies on either computational fluid dynamics or viscous-inviscid solvers, for instance, XFOIL. However, the latter tools lack a formulation for the effect of VGs. The purpose of this thesis is to get a step closer towards aerofoil optimisation process including VGs. Lag dissipation integral boundary-layer formulation of Drela [14], Drela and Giles [16] is considered. Stereoscopic particle image velocimetry measurement (Baldacchino et al. [6]) and numerical simulation based on Menters two-equation $k - omega$ SST turbulence (Florentie et al. [18]) of counter-rotating VG configuration based on Godard and Stanislas [22] optimisation on a flat plate in turbulent flow regime is studied.Vortex generator induced flow, VGIF exhibit quasi-uniform effect only after twelve times the boundary layer thickness downstream of the device. An approach to modifying the slip velocity concept to incorporate VGIF is proposed. Recommendations for direct wall shear stress and comprehensive drag measurements for VG induced flow are argued to validate the claim.

Keywords: Vortex generator, flat plate, two-dimensional integral boundary layer relations, skin-friction coefficient, dissipation coefficient, effective slip velocity parameter.

Acknowledgements

I wish to thank the following persons. Dr.ir. C.J. Simao Ferreira for setting up the master thesis and supervision. Ir. D. Baldacchino for valuable pieces of advice, guidance and motivation. Dr.ir. R.G. Néstor for constant support to finish the thesis work smoothly. Ir. L. Florentie for providing required material and promptly responding to queries.

On a personal level, I thank fellow students in 5.18, 6.08 LR and my housemates. Thesis work is an embodiment of all the people I have met throughout in academic, professional and personal sphere. The big and small things mattered. Of course, there are favourites; you know who you are.

Delft, The Netherlands
May 2, 2016

Ashok Kumar Nedumaran

Contents

Summary v

Acknowledgements vii

List of Figures xvii

List of Tables xix

Nomenclature xxi

I Introduction 1

1 Introduction 3
1.1 Background information . . . 3
1.2 Thesis motivation . . . 4
1.2.1 Primary objective and preliminary approach . . . 5

II Materials and Method 7

2 Dataset, reduction techniques and preliminary data validation 9
2.1 Dataset . . . 9
2.1.1 Vortex generator configuration . . . 9
2.1.2 Experimental measurements . . . 10
2.1.3 Numerical simulations . . . 11
2.2 Reduction Techniques . . . 11
2.2.1 Determining the wall position for experimental measurements . . . 11
2.2.2 Determining the boundary layer edge velocity . . . 12
2.3 General flow field characteristics . . . 13

3 Methodology **17**

3.1 Brief introduction to two dimensional integral boundary layer solution methods . . . 17

3.1.1 Integral thickness interpretation and shape parameters . . . 19

3.1.2 Determining integral parameters from discrete data . . . 19

3.2 Drela and Giles [16] turbulent closure relations . . . 21

3.3 Skin Friction . . . 22

3.3.1 Limited survey of estimation methods and closure relations . . . 22

3.3.2 Limited survey of velocity profile expressions . . . 22

3.3.3 Skin-friction coefficient closure relations compared using Österlund database . . . 24

3.4 Dissipation coefficient . . . 24

3.5 The most relevant flow quality or qualities that describe a vortex generator induced flow . . . 29

3.6 Detailed approach . . . 30

III Results and Discussion **31**

4 Integral Parameters' Estimations and Approximations from Experimental and Numerical Dataset **33**

4.1 Skin-friction coefficient estimation for vortex generator induced flow using velocity profile . . . 33

4.1.1 Using Kendall and Koochesfahani [25] method . . . 34

4.1.2 Using Swafford [49] closure relation . . . 36

4.1.3 Should we consider upstream effects for determining C_f for VGIF ? 36

4.2 Downstream development of integral parameters of interest . . . 40

5 Testing integral boundary layer relations for vortex generator induced flow using numerical dataset **61**

5.1 Chapter Terminology . . . 61

5.2 Uncertainty in determining $C_f[\mathcal{R}]$ and $C_{\mathcal{D}}[\mathcal{R}]$ . . . 63

5.2.1 Error due to non-uniform grid spacing . . . 63

5.2.2 Error due to boundary layer edge velocity detection method . . . 63

5.3 Results and discussion . . . 66

5.3.1 The conditioning effect: Is 2D or 3D mechanism predominant? . . . 69

5.4 Key integral parameter . . . 69

5.4.1 Inputting the correct effective slip velocity parameter . . . 72

IV Conclusion **77**

6 Conclusion **79**

V Appendix 81

A Skin-friction coefficient estimation method comparison 83

B Dimensionless Profile 89

C Swafford profile comparison 95

D Coles Law of Wake 97

E Boundary Layer Edge Velocity 103

F Velocity, Total shear and Reynolds shear stress profile 105

G Wall and wake layer contribution for dissipation coefficient 113

References 119

List of Figures

2.1 Coordinate system. 10
2.2 Vortex generator array configuration schematics for experimental measurements. Schematics reproduced from Baldacchino et al. [6]. 11
2.3 A snapshot of mesh (structured, 1.6 million cells) generated for numerical simulations. 12
2.4 Vortex generators as seen from above. 13
2.5 Streamwise velocity profile for uncontrolled flow. 14
2.6 Streamwise, wall-normal and spanwise velocity profile and Reynold's shear stress for vortex generator induced flow. At 10 device heights downstream of the VGs and spanwise position, $z/D = 0$ 15
2.7 Streamwise, wall-normal and spanwise velocity profile and Reynold's shear stress for vortex generator induced flow. At 10 device heights downstream of the VGs and spanwise position, $z/D = 0.208$ 15
2.8 Streamwise, wall-normal and spanwise velocity profile and Reynold's shear stress for vortex generator induced flow. At 10 device heights downstream of the VGs and spanwise position, $z/D = 0.333$ 16
2.9 Streamwise, wall-normal and spanwise velocity profile and Reynold's shear stress for vortex generator induced flow. At 10 device heights downstream of the VGs and spanwise position, $z/D = 0.5$ 16

3.1 Interpretation of the integral thickness for incompressible flow, in terms of the geometry of the normalised velocity profile (u/u_e). Schematic inspired from Drela [15] and García [20] 20
3.2 Representation of velocity profile for different shape parameter and momentum thickness using Swafford velocity profile relation 20
3.3 Error in determining skin-friction coefficient using gradient method for different wall units,y^+ as upper limit. 25
3.4 28

4.1 Percentage error of skin-friction coefficient for vortex generator induced flow from numerical dataset. Skin-friction coefficient obtained using gradient method is considered as true value and from Kendall and Koochesfahani [25] as estimated value. 35

4.2 36
4.3 Comparison of velocity profile for VG test case [numerical dataset] at $(x - x_{VG})/h = -15$ with Coles' wall-wake formula at different spanwise locations. 37
4.4 Comparison of velocity profile for VG test case [numerical dataset] at $(x - x_{VG})/h = 10$ with Coles' wall-wake formula at different spanwise locations. 37
4.5 Displacement thickness development in streamwise direction 42
4.6 Spanwise averaged displacement thickness development in streamwise direction 43
4.7 Momentum thickness development in streamwise direction 44
4.8 Spanwise averaged momentum thickness development in streamwise direction 45
4.9 Kinetic energy thickness development in streamwise direction 46
4.10 Spanwise averaged kinetic energy thickness development in streamwise direction 47
4.11 Skin-friction coefficient development in streamwise direction 48
4.12 Spanwise averaged skin-friction coefficient development in streamwise direction 49
4.13 Shear stress coefficient development in streamwise direction 50
4.14 Spanwise averaged shear stress coefficient development in streamwise direction 51
4.15 Effective slip velocity development in streamwise direction 52
4.16 Spanwise averaged effective slip velocity development in streamwise direction 53
4.17 Dissipation coefficient development in streamwise direction 54
4.18 Spanwise averaged dissipation coefficient development in streamwise direction 55
4.19 Shape parameter development in streamwise direction 56
4.20 Spanwise averaged shape parameter development in streamwise direction . 57
4.21 Kinetic energy shape parameter development in streamwise direction . . . 58
4.22 Spanwise averaged kinetic energy shape parameter development in streamwise direction 59

5.1 Error due to non-uniform grid spacing. $x, [m]$ is the streamwise distance in meters. $dx, [m]$ is the differential streamwise distance in meters. $(x - x_{vg})/h$ [-] is the dimensionless streamwise distance, where x_{vg} is location of trailing edge VG, and h is the VG height. 63
5.2 Interpolated skin-friction coefficient downstream development against unique data points. 64
5.3 Interpolated dissipation coefficient downstream development against unique data points. 64
5.4 Uncertainty in determining skin-friction coefficient due to boundary edge velocity detection method. 65
5.5 Uncertainty in determining dissipation coefficient due to boundary edge velocity detection method. 65
5.6 Dissipation coefficient, $C_{\mathcal{D}}$ [-] development in streamwise direction. Streamwise distance, x is dimensionalised by VG trailing edge location, x_{vg} and VG height, h. For legend details, please refer to section 5.1 and table 5.1 . 66

5.7 Dissipation coefficient, $C_{\mathcal{D}}$ [-] development in streamwise direction. Streamwise distance, x is dimensionalised by VG trailing edge location, x_{vg} and VG height, h. For legend details, please refer to section 5.1 and table 5.1 67
5.8 . . . 68
5.9 . . . 68
5.10 Dissipation coefficient obtained using only turbulent closure relations . . . 71
5.11 Performance comparison. Using only turbulent closure relations . . . 71
5.12 Dissipation coefficient obtained using only turbulent closure relations with corrected skin-friction value . . . 72
5.13 Performance comparison.Using only turbulent closure relations with corrected skin-friction value . . . 73
5.14 Dissipation coefficient obtained using only turbulent closure relations with corrected effective slip velocity parameter value. . . . 74
5.15 Dissipation coefficient obtained using only turbulent closure relations with corrected effective slip velocity parameter value. . . . 74
5.16 . . . 75

A.1 Skin-friction coefficient, C_f [-] development in streamwise direction for vortex generator, (VG) case from numerical dataset obtained using gradient method, $[GM]$ (see 3.3.1) is compared with C_f obtained from Swafford's closure relation, $[SCR]$ (see 3.2). Comparison is done at different spanwise locations, $(z/D = 0, 0.208, 0.333, 0.487)$ and spanwise averaged value. Streamwise distance, x is dimensionalised by VG trailing edge location, x_{vg} and VG height, h. . . . 84
A.2 . . . 85
A.3 . . . 85
A.4 . . . 86
A.5 . . . 86
A.6 . . . 87

B.1 Comparison of velocity profile for VG test case [numerical dataset] at $(x - x_{VG})/h = -10$ with Musker profile at different spanwise locations. . . . 90
B.2 Comparison of velocity profile for VG test case [numerical dataset] at $(x - x_{VG})/h = -5$ with Musker profile at different spanwise locations. . . . 90
B.3 Comparison of velocity profile for VG test case [numerical dataset] at $(x - x_{VG})/h = 0$ with Musker profile at different spanwise locations. . . . 91
B.4 Comparison of velocity profile for VG test case [numerical dataset] at $(x - x_{VG})/h = 5$ with Musker profile at different spanwise locations. . . . 91
B.5 Comparison of velocity profile for VG test case [numerical dataset] at $(x - x_{VG})/h = 15$ with Musker profile at different spanwise locations. . . . 92
B.6 Comparison of velocity profile for VG test case [numerical dataset] at $(x - x_{VG})/h = 25$ with Musker profile at different spanwise locations. . . . 92
B.7 Comparison of velocity profile for VG test case [numerical dataset] at $(x - x_{VG})/h = 50$ with Musker profile at different spanwise locations. . . . 93
B.8 Comparison of velocity profile for VG test case [numerical dataset] at $(x - x_{VG})/h = 75$ with Musker profile at different spanwise locations. . . . 93

B.9 Comparison of velocity profile for VG test case [numerical dataset] at $(x - x_{VG})/h = 100$ with Musker profile at different spanwise locations. 94

D.1 Comparison of velocity profile for VG test case [numerical dataset] at $(x - x_{VG})/h = -10$ with Coles' wall-wake formula at different spanwise locations. 98

D.2 Comparison of velocity profile for VG test case [numerical dataset] at $(x - x_{VG})/h = -5$ with Coles' wall-wake formula at different spanwise locations. 98

D.3 Comparison of velocity profile for VG test case [numerical dataset] at $(x - x_{VG})/h = 0$ with Coles' wall-wake formula at different spanwise locations. 99

D.4 Comparison of velocity profile for VG test case [numerical dataset] at $(x - x_{VG})/h = 5$ with Coles' wall-wake formula at different spanwise locations. 99

D.5 Comparison of velocity profile for VG test case [numerical dataset] at $(x - x_{VG})/h = 15$ with Coles' wall-wake formula at different spanwise locations. 100

D.6 Comparison of velocity profile for VG test case [numerical dataset] at $(x - x_{VG})/h = 25$ with Coles' wall-wake formula at different spanwise locations. 100

D.7 Comparison of velocity profile for VG test case [numerical dataset] at $(x - x_{VG})/h = 50$ with Coles' wall-wake formula at different spanwise locations. 101

D.8 Comparison of velocity profile for VG test case [numerical dataset] at $(x - x_{VG})/h = 75$ with Coles' wall-wake formula at different spanwise locations. 101

D.9 Comparison of velocity profile for VG test case [numerical dataset] at $(x - x_{VG})/h = 100$ with Coles' wall-wake formula at different spanwise locations. 102

F.1 Velocity, total shear and Reynolds shear stress profile for VG test case [numerical dataset] at $(x - x_{VG})/h = -15$ for different spanwise locations compared with spanwise averaged profile. 106

F.2 Velocity, total shear and Reynolds shear stress profile for VG test case [numerical dataset] at $(x - x_{VG})/h = -10$ for different spanwise locations compared with spanwise averaged profile. 106

F.3 Velocity, total shear and Reynolds shear stress profile for VG test case [numerical dataset] at $(x - x_{VG})/h = -5$ for different spanwise locations compared with spanwise averaged profile. 107

F.4 Velocity, total shear and Reynolds shear stress profile for VG test case [numerical dataset] at $(x - x_{VG})/h = 0$ for different spanwise locations compared with spanwise averaged profile. 107

F.5 Velocity, total shear and Reynolds shear stress profile for VG test case [numerical dataset] at $(x - x_{VG})/h = 5$ for different spanwise locations compared with spanwise averaged profile. 108

F.6 Velocity, total shear and Reynolds shear stress profile for VG test case [numerical dataset] at $(x - x_{VG})/h = 10$ for different spanwise locations compared with spanwise averaged profile. 108

F.7 Velocity, total shear and Reynolds shear stress profile for VG test case [numerical dataset] at $(x - x_{VG})/h = 15$ for different spanwise locations compared with spanwise averaged profile. 109

F.8 Velocity, total shear and Reynolds shear stress profile for VG test case [numerical dataset] at $(x - x_{VG})/h = 25$ for different spanwise locations compared with spanwise averaged profile. 109

F.9 Velocity, total shear and Reynolds shear stress profile for VG test case [numerical dataset] at $(x - x_{VG})/h = 50$ for different spanwise locations compared with spanwise averaged profile. 110

F.10 Velocity, total shear and Reynolds shear stress profile for VG test case [numerical dataset] at $(x - x_{VG})/h = 75$ for different spanwise locations compared with spanwise averaged profile. 110

F.11 Velocity, total shear and Reynolds shear stress profile for VG test case [numerical dataset] at $(x - x_{VG})/h = 100$ for different spanwise locations compared with spanwise averaged profile. 111

G.1 Comparison of $C_{\mathcal{D}}$ from dissipation integral compared with effective slip velocity method [U_s and C_τ determined from numerical dataset] at $z/D = 0.500$ in streamwise direction. 114

G.2 Comparison of $C_{\mathcal{D}}$ from dissipation integral compared with effective slip velocity method [U_s and $C_{\tau,eq}$ determined from [16] closure relations] at $z/D = 0.500$ in streamwise direction. 114

G.3 Comparison of $C_{\mathcal{D}}$ from dissipation integral compared with effective slip velocity method [U_s and C_τ determined from numerical dataset] at $z/D = 0.333$ in streamwise direction. 115

G.4 Comparison of $C_{\mathcal{D}}$ from dissipation integral compared with effective slip velocity method [U_s and $C_{\tau,eq}$ determined from [16] closure relations] at $z/D = 0.333$ in streamwise direction. 115

G.5 Comparison of $C_{\mathcal{D}}$ from dissipation integral compared with effective slip velocity method [U_s and C_τ determined from numerical dataset] at $z/D = 0.208$ in streamwise direction. 116

G.6 Comparison of $C_{\mathcal{D}}$ from dissipation integral compared with effective slip velocity method [U_s and $C_{\tau,eq}$ determined from [16] closure relations] at $z/D = 0.208$ in streamwise direction. 116

G.7 Comparison of $C_{\mathcal{D}}$ from dissipation integral compared with effective slip velocity method [U_s and C_τ determined from numerical dataset] at $z/D = 0$ in streamwise direction. 117

G.8 Comparison of $C_{\mathcal{D}}$ from dissipation integral compared with effective slip velocity method [U_s and $C_{\tau,eq}$ determined from [16] closure relations] at $z/D = 0$ in streamwise direction. 117

List of Tables

2.1 Vortex generator properties. 9
2.2 Geometrical terminology. 10

3.1 Comparison of velocity profile relations w.r.t to Österlund dataset 24
3.2 Comparison of skin-friction coefficient estimation methods. 25
3.3 Comparison of dissipation coefficient, $C_{\mathcal{D}}$ using different relations. Upstream data (15 device height behind trailing edge of VGs) from numerical dataset is used. 27

5.1 Terminology exclusive for chapter 5 62
5.2 Maximum tolerable adverse pressure gradient 75

Nomenclature

Latin Symbols

$\mathcal{A}$	G-beta constant for equilibrium turbulent flow	$[-]$
$\mathcal{B}$	G-beta constant for equilibrium turbulent flow	$[-]$
$C_{\mathcal{D}}$	Dissipation coefficient	$[-]$
C_D	Drag coefficient	$[-]$
C_f	Skin-friction coefficient	$[-]$
C_τ	Shear stress coefficient	$[-]$
$\mathcal{D}$	Dissipation integral	$[-]$
D	Drag	$[-]$
G	Clauser shape parameter	$[-]$
H	Boundary layer shape parameter	$[-]$
H^*	Kinetic energy shape parameter	$[-]$
Re_θ	Momentum thickness Reynolds number	$[-]$
Re	Reynolds number	$[-]$
u_e	Boundary layer edge velocity	$[m/s]$
U_s	Effective slip velocity	$[-]$
u	Cartesian x-velocity component	$[m/s]$
v	Cartesian y-velocity component	$[m/s]$
w	Cartesian z-velocity component	$[m/s]$
x	Cartesian streamwise (axial, longitudinal) axis	$[-]$
y	Cartesian wall-normal axis	$[-]$

z	Cartesian spanwise (transverse, lateral) axis	$[-]$

Greek Symbols

β	Clauser pressure gradient parameter	$[-]$
δ^*	Displacement thickness	$[m]$
μ	Viscosity	$[kg/(m.s)]$
μ_t	Eddy viscosity	$[kg/(m.s)]$
ν	Kinematic viscosity	$[m^2/s]$
ρ	Density	$[kg/m^3]$
θ	Momentum thickness	$[m]$
θ^*	Kinetic energy thickness	$[m]$

Subscripts

$_\infty$	Freestream
$_e$	At edge of boundary layer
$_{TE}$	At trailing edge
$_w$	At wall

Abbreviations

$\mathcal{R}$	Reminder
2D	Two Dimnesional
AILC	Apparent Inner Layer Contribution
AOLC	Apparent Outer Layer Contribution
APG	Adverse Pressure Gradient
BL	Boundary Layer
CFD	Computational Fluid Dynamics
DCR	Drela's Closure Relation
Exp	Experimental
GM	Gradient Method
IBLP	Integral Boundary Layer Parameter
IBL	Integral Boundary Layer
LCOE	Levelised Cost of Energy
LTCR	Ludwieg and Tillmann Closure Relation

Num	Numerical
PIV	Particle Image Velocimetry
RANS	Reynolds Averaged Navier Stokes
SBVG	Subboundary-layer vortex generator
SCR	Swafford's Closure Relation
TBL	Turbulent Boundary Layer
UCF	Uncontrolled Flow
UC	Uncontrolled
VGIF	Vortex Generator Induced Flow
VG	Vortex Generator
ZPG	Zero Pressure Gradient

Part I

Introduction

Chapter 1

Introduction

The primary objective of the thesis is to determine the most relevant parameter/parameters for the validation of a two-dimensional integral boundary layer solution method for vortex generator induced flow. This chapter is the introduction to the thesis work carried out. First some background information on problem is discussed in section 1.1. Then, in section 1.2 the motivation for the thesis is argued, based on that main objective and preliminary approach is formulated.

1.1 Background information

Climate change is real and the need to take positive steps to mitigate it is gaining popular opinion. The positive sentiment by general media and public on Paris agreement, Leonardo DiCaprio Oscar speech and "yuge "(huge) young voters support for presidential candidate Bernie Sanders's pro-clean energy policies. These could be considered as the major social indicators at present period. However, the levelised cost of energy, LCOE is an important driver.Humankind has used the wind over a millennium to pump water, grind grain, sail ships. In the early 1900s, the wind was used to generate electricity at widespread scale all over Europe and to electrify rural homes and farms in America (Pasqualetti et al. [43]). It was a convenient and cheap form of energy. With a boom in fossil fuels, utilisation of wind energy diminished. However, in 1973 when The Organization of Petroleum Exporting Countries (OPEC) enforced an oil embargo, causing oil prices to increase a precarious level. Rekindled enthusiasm in renewable energy, particularly in developing large wind turbine systems (For instance the *Great California Wind Rush*). However, the excitement was short-lived as they were not cost competitive with systems using fossil fuels the early 1990s. Interestingly around the same time, United Nations Framework Convention on Climate Change (UNFCCC) was negotiated at the Earth Summit in Rio de Janeiro in 1992 with an objective to stabilise greenhouse gas concentrations. It took another thirteen years for Kyoto protocol (an extension of UNFCC) to enter into force.The Global Wind Energy Outlook report [1] state that the wind power could reach 2000GW by 2030, and supply up to $17 - 19\%$ of global electricity.

Annual Energy Outlook 2015 [2] predict for 2020, that wind turbine (onshore) as the lowest LCOE for non-dispatchable energy. Closely behind geothermal, natural gas-fired in dispatchable energy. It is an opportune moment for wind energy to make a come back and reducing LCOE further will ensure it.

Delaying or preventing flow separation is an important parameter in many technical applications, to enhance the performance. It is also applicable for modern day wind turbines. A typical horizontal axis wind turbine have thick aerofoils at the root section to ensure it can withstand a high out-of-rotor-plane-loading. Also, due to manufacturing and transportation constraints, the blade cannot be twisted to adapt to the direction of the local flow velocity. Which leads to separation at the root section of wind turbines, and it may also cause separation in the entire blade. Also, most wind turbines face aerodynamic performance losses due to the accumulation of bugs and dirt at the leading edge of the rotor blades. Leads to early boundary layer transition resulting in a higher drag coefficient and can cause early stalling of the aerofoil. Hence, by delaying or preventing flow separation the aerodynamic efficiency increases and material usage reduce due to decreased loads. Thus, bringing down the LCOE.

Most elegant way to mitigate separation would be to find an optimal body shape to control the pressure rise. It would indicate a streamlined shape however due to constraints discussed before it is hard to implement. Hence, a need for some form of boundary layer control mechanism to decrease the retardation of the boundary layer due to adverse pressure gradients. In principle, there are two ways to achieve it, either add high momentum or remove low momentum air in the bottom of the boundary layer. By suction through slots or porous wall, the low momentum air is removed from the wall. Or by blowing air through a tangential slot in the wall or by mixing the air with the free stream, high momentum air added to the wall. Other techniques exist such as active unsteady blowing. It controls the effects of separation by manipulation of the separated shear layers.

Passive vortex generators (VGs) as flow control device is considered for the thesis. Vortex generators are a popular choice as they are easy to fabricate and install on the wind turbine blades. Also, they are relatively cheap. Moreover, they can be retrofitted to blades that do not perform as designed. Vortex generator through streamwise (longitudinal) vortices re-energies the flow by mixing high momentum air from the outer flow. Thus, the flow is more resilient to the retardation effect of adverse pressure gradients. Unanimously all the scientific literature on VGs credit the wind tunnel group of the United Aircraft Corporation Taylor [50] for the initial design. They used VGs to eliminate boundary layer separation of their wind tunnel. First scientific study on VGs is done by Schubauer and Spangenberg [45]. Genesis of VGs is not clear, however in nature, one can see some evidence. Low profile/submerged VGs in sharks, mackerels to keep flow attached and large VGs in bottlenose dolphin for the purpose of thermoregulation (Bechert et al. [7]).

1.2 Thesis motivation

Sullivan [48] is the first scientific evidence of VGs implemented on the wind turbine. VGs were tested on a two bladed MOD-2 wind turbine and determined the VGs has little effect at low wind speeds, at higher wind speed VG's delays stall and improves power generating capability. Using 70 % VGs (blade span), wind speed required to produce rated power is

decreased by 2.2 m/sec and annual energy increase of 11% is projected. Moreover, using 100 % VGs reduced rate wind speed by 0.5 m/sec and projected annual energy capture by an additional 9 %. Projected annual energy calculation is not mentioned explicitly. Another widely cited evidence is Øye [42], where 25% increase in power at rated wind speed.

Vortex generators can delay flow separation, aerodynamic stalling and considerable improve the aerodynamic performance of rough blades. However, in other conditions if VGs are not configured optimally, may have adverse aerodynamic performance due to increase in drag (Gaunaa et al. [21]). Drag due to adding VGs and additional drag due to energizing the boundary drag. The effectiveness of VGs in wind turbine application can be measured as delaying/preventing separation with minimal drag increase.

Vortex generator array has different configuration parameters such as general shape, height, length, angle to the main flow direction and location on the wind turbine blade (spanwise spacing and chordwise location). The optimal configuration could be determined by extensive experimental measurements, which is expensive and time-consuming due to number of optimisation parameters. Computational fluid dynamics, CFD for aerofoil with VGs is more time consuming than uncontrolled aerofoil due to the increased number of grid points around VGs and need for computing three spatial dimensions. Researchers have replaced the geometries with volume forces mimicking vortices behind the VGs, (Stillfried et al. [47], spanwise averaging the Navier-Stroke equation and extra source terms Nikolaou et al. [38]) to reduce the computation time. All the methods conclude the result is qualitatively similar, quantitatively failing. Methods still, solve the nonlinear partial differential equations which are challenging and hence time-consuming. An easier method is to solve the integrated forms of the equations, hence just ordinary differential equations. Considerable simplification arises when the non-linear partial differential equations are integrated across the boundary layer. However, they are quite accurate and computationally efficient.

McLean [34] claims that the researchers at QinetiQ, Ltd, based on experimental studies by Ashill et al. [3, 4] have developed a 2D integral boundary-layer code to simulate the effects of low-profile VGs. They have simulated by considering VGs effect in spanwise-averaged terms. Unfortunately, no information is available about the modelling technique and performances. Kerho et al. [26] modified the XFOIL boundary layer formulation by enhancing the turbulence production to mimic vortex generators. Their research objective is to extend the laminar run and use the VGs to eliminate separation bubble, by a thin turbulent boundary layer with a minimal increase in drag. They formulate for a very specific model, which exhibit quasi-uniform properties. Numerous literature indicates VGs do not exhibit quasi-uniform properties. See review article of [5] more references.

1.2.1 Primary objective and preliminary approach

The success of 2D dimensional integral boundary layer solution methods for VGIF gives an impetus to pursue it. Conditional spanwise averaging or spanwise averaging with source term of VGIF also has met with some success.

The principal objective of the thesis is formulated as:

Determine the most relevant parameter/parameters for the validation of a two-dimensional integral boundary layer solution method for vortex generators induced flow.

To determine the main objective, as a preliminary approach following things needs to be identified:

1. The parameters used in two-dimensional integral boundary layer method solution methods.
2. The most relevant flow quality or qualities that describe a vortex generator induced flow.

Part II

Materials and Method

Chapter 2

Dataset, reduction techniques and preliminary data validation

As discussed in section 1.1, experimental measurements and numerical simulations are difficult to perform for vortex generator induced flow as well as time-consuming. Experimental measurements and numerical simulations were performed for the classical vane-type counter-rotating vortex generators on a flat plate. Vortex generator configuration, experimental measurements and numerical simulations are discussed in section 2.1. Reduction techniques and preliminary data validation are discussed in sections 2.2 and 2.3 respectively.

2.1 Dataset

2.1.1 Vortex generator configuration

Vortex generator dimensions were designed according to the recommendations of Godard and Stanislas [22] and are summarized in table 2.1.

Parameter	Value	Size in factor of VG height, h
h	$5mm$	1
h/δ	≈ 0.25	
d	$12.5mm$	$2.5h$
L	$12.5mm$	$2.5h$
D	$30mm$	$6h$
β	$18°$	–

Table 2.1: *Vortex generator properties.*

Godard and Stanislas [22] performs optimisation study based on the skin friction, C_f improvement at the location where C_f reaches minimum for uncontrolled case (smooth

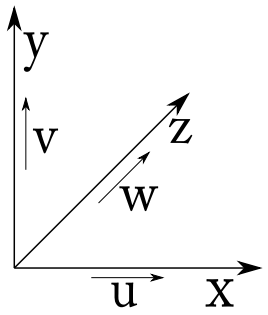

Figure 2.1: *Coordinate system.*

Axis	Axis name
x	streamwise (axial, longitudinal)
y	wall-normal
z	spanwise (lateral, transverse)

Table 2.2: *Geometrical terminology.*

wall). It implies the optimisation is done for which VG configuration viscous dissipation of the vortices is the most rapid. This behaviour is only beneficial for flow-control application with substantially reduced height, for instance, S-duct ([29]).

Moreover, skin-friction coefficient may be an important parameter to determine the effectiveness for counter-rotating VGs, definitely not for co-rotating VGs (see section 3.5). Godard and Stanislas [22] does not mention about drag measurement method, but drag at few places: "Moreover the triangular shape is better in term of drag penalty "; "In this test, the hypothesis was made that, when the VG height increase above 0.2δ, the device drag increases without a significant increase of $\Delta\tau/\tau_0$ ".

Author speculates the hypothesis was based on the paper of [30]. It claims increasing device height will only increase drag without significantly increasing the pressure recovery.

Godard and Stanislas [22] gives an optimal h/δ of 0.37 for counter rotating VGs. Implements *Schlichting* shape factor equation (see equation 2.1) to determine the adverse pressure gradient effect on the boundary layer.

$$H = 0.5442 \times H_{23}\sqrt{\frac{H_{23}}{H_{23} - 0.5049}} \tag{2.1}$$

It is based on so-called *one parameter equations* which gets the adverse pressure gradient capability based on a power law. The validity of such are under question for separated flows, let alone for VG induced flows (see 3.4). It is also interesting in the later editions of the book this equation is not mentioned.

Right-handed Cartesian coordinate system as illustrated in figure 2.1.1 is used for current thesis work. The corresponding geometrical terminology is tabulated in table 2.1.1. For streamwise coordinate, x the leading edge of the flat plate is chosen as the origin, with the positive sign towards the trailing edge. For wall-normal coordinate, y the upper surface of the wall is chosen as the origin, with the positive sign towards the upstream velocity. For spanwise coordinate, z the plane of symmetry is chosen as the origin, with the positive sign towards the right-hand side (top view).

2.1.2 Experimental measurements

Stereoscopic particle image velocimetry (SPIV) experiments were carried out in 1.5×0.25 m^2 boundary layer wind tunnel (5.6 m length) at velocity of $u_\infty = 15$ m/s (refer to

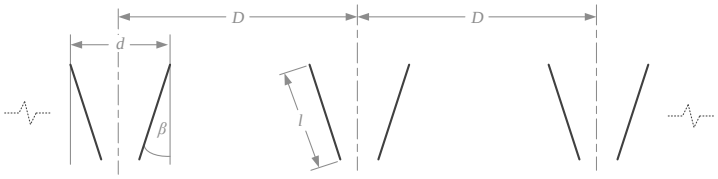

Figure 2.2: *Vortex generator array configuration schematics for experimental measurements. Schematics reproduced from Baldacchino et al. [6].*

Baldacchino et al. [6] more details). Two LaVision Imager Pro LX 16 Mpix cameras equipped with Nikon Micro-Nikor 105 mm lenses and Scheimflug adapters were used for imaging. Quantel Evergreen Nd:Yag laser system with 200mJ/pulse output provided illumination. After average correlation processing a resolution of 7 vectors/mm with a final interrogation area of 16×16 txl (0.2×0.2 mm^2) and spatial overlap of 50 percent was obtained. A total of 15 vortex generator pairs were mounted during the tests, spanning a total of $420mm$, with the mid-span of the array centred at the test section centre of the wind tunnel. Measurements were taken at mid-span of the array to a spanwise extent of $1.5D$.

2.1.3 Numerical simulations

Steady incompressible Reynolds-averaged Navier-Stokes (RANS) simulations with OpenFOAM were performed (refer to Florentie et al. [18] for starting basis of the numerical simulations), using a fully resolved boundary layer ($y^+ < 2$) and Menter's $k - \omega$ Shear Stress Transport (SST) Turbulence Model. The RANS equations are solved using the Semi-Implicit Method for Pressure-Linked Equations (SIMPLE) algorithm and the governing equations are solved using first order upwind discretization schemes for the convective terms. The linear systems arising from the equation discretization are solved using the preconditioned (bi-) conjugate gradient method with diagonal incomplete Cholesky and diagonal incomplete LU preconditioners for the symmetric and asymmetric systems respectively. Only one pair of VGs was simulated, the influence of the other VGs was considered by symmetry boundary conditions.

2.2 Reduction Techniques

2.2.1 Determining the wall position for experimental measurements

Kendall and Koochesfahani [25] method is implemented to determine the wall position as well as wall friction the for uncontrolled case. The method utilises the fit of the measured velocity data to a Musker [35] profile. Kendall and Koochesfahani [25] itself critiques that the validity of the method depends on accurateness of the model velocity profile. Even for Musker [35] profile the van Kármán constants inputted alters the accuracy.

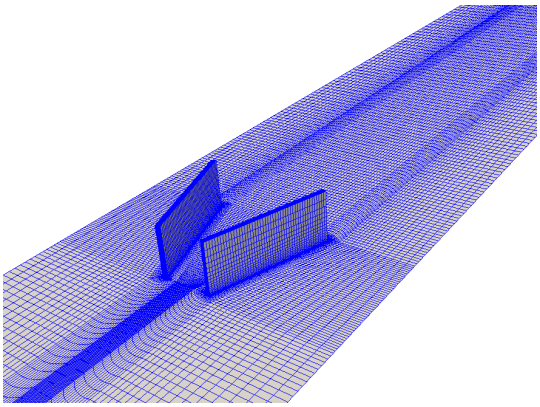

Figure 2.3: *A snapshot of mesh (structured, 1.6 million cells) generated for numerical simulations.*

However, Örlü et al. [39] analysed the Kendall and Koochesfahani [25] method and concluded that results have a bias. Bias being that Kendall and Koochesfahani [25] have not assessed the performance of optimisation routine when the near wall data reaches the upper limit viscous sublayer. Moreover, stated accuracy, mentioned in Kendall and Koochesfahani [25] is only achievable if the measurement points as close as 5 wall units are available. The bias stated by Örlü et al. [39] on the Kendall and Koochesfahani [25] method is verified. However, 5 wall units term is not universal as the Österlund [40] dataset is used for analysis (See section 3.3.3). Rodríguez-López et al. [44] have stated more robust method, with van Kármán constants also as additional optimisation parameters. Method claims, it can accurately predict the wall position even with first data points as far as 10 wall units. In principle (retrospectively) investigations have a resolution of approximately 4.2 wall units for the uncontrolled case. So, the maximum distance should be 4.2 wall units. Wall position obtained for the uncontrolled case is used for the vortex generator case. There is some uncertainty in employing this technique. Nevertheless, it is implemented.

2.2.2 Determining the boundary layer edge velocity

It is common practice to define the edge of the boundary layer $U_e = 0.99U_\infty$. To automate the process, method used in Velte [54] is implemented. The method argues that boundary layer could be defined as the part of the flow contained by vortices generated due to the presence of wall. Therefore, the boundary layer edge can be determined where the value of the vorticity is reduced to a value much smaller than the maximum value. Velte [54] further argues that by magnitude analysis if u and x are order of 1, then v and y are of order δ. Hence, the second term is quadratically larger than the first term. Therefore, boundary layer edge velocity was determined from the velocity profile. In principle, $U_e = 0.99U_\infty$ indicates that the $du/dy \approx 0$. However, experimental dataset the data is a bit noisy. Hence, it was visually checked at different points. For the numerical dataset, the process was automated. At few locations, the automation process is cross verified

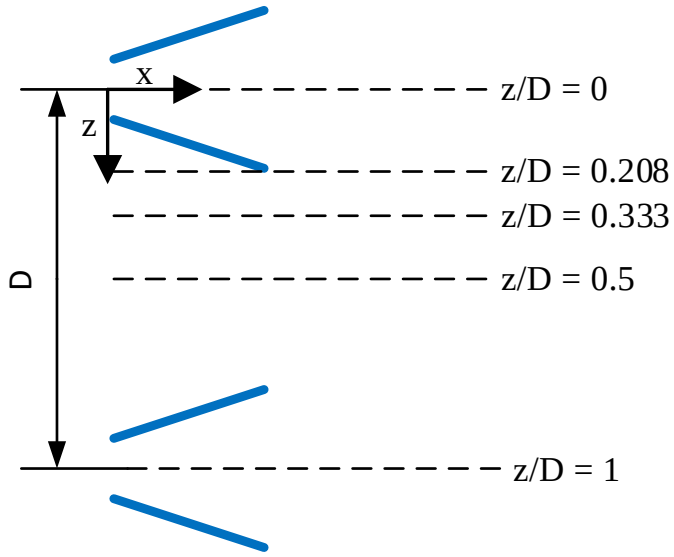

Figure 2.4: *Vortex generators as seen from above.*

where the Reynold's shear stress also approaches zero.

$$\omega_z = \frac{1}{2}\left(\underbrace{\frac{\partial v}{\partial x}}_{\frac{\delta}{1}} - \underbrace{\frac{\partial u}{\partial y}}_{\frac{1}{\delta}}\right) \tag{2.2}$$

2.3 General flow field characteristics

Due to streamwise vortices, the high-momentum fluid is carried down to wall inside the VG pair ($z/D = 0$,$z/D = 0.208$) and low-momentum fluid is pushed away from the wall between VG pairs ($z/D = 0.5$,$z/D = 0.333$). From figures, it is clearly observed by negative values of wall-normal velocity, v inside the VG pair and positive values of wall-normal velocity, v between VG pairs. At downstream location, $x/h = 10$ wall-normal velocity is higher at $z/D = 0.333$, as we proceed downstream wall-normal velocity is higher at $z/D = 0.5$. Also, as we proceed downstream magnitude of wall-normal velocity decreases indicating decrease in momentum exchange. The exchange of high and low flow momentum fluid results in a fuller streamwise velocity,u profile inside the VG pair indicating higher skin friction and vice-versa. This is quite consistent with counter-vortex generator mechanism and other studies.

Customarily experimenters verify the two-dimensionality of the flow if the spanwise variation of the friction velocity, μ_τ is very low. However, inherently the VGIF will result in

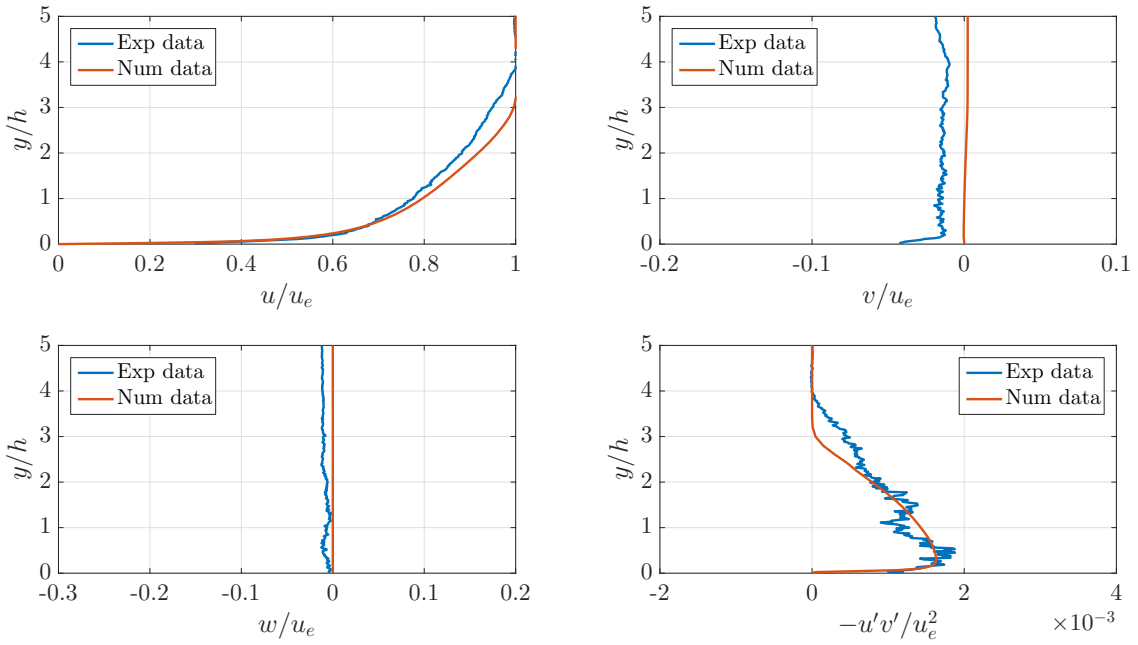

Figure 2.5: *Streamwise velocity profile for uncontrolled flow.*

significant spanwise variations in friction velocity. Same is the case for dataset used for this thesis work (please refer to figure 4.11).

Also for the mean flow structure to be two-dimensional following conditions has to be satisfied,

$$\overline{w} = 0 \quad \frac{\partial w}{\partial z} = 0$$

From figures 2.6, 2.7, 2.8 and 2.9 one can observe spanwise velocity, w is non zero inside the VG pair ($z/D = 0$,$z/D = 0.208$). From these two observations, it is evident the flow field is three dimensional in nature. However, skin friction variation in spanwise direction is symmetrical thus giving further impetus to proceed with integral layer modelling in spanwise-averaged terms.

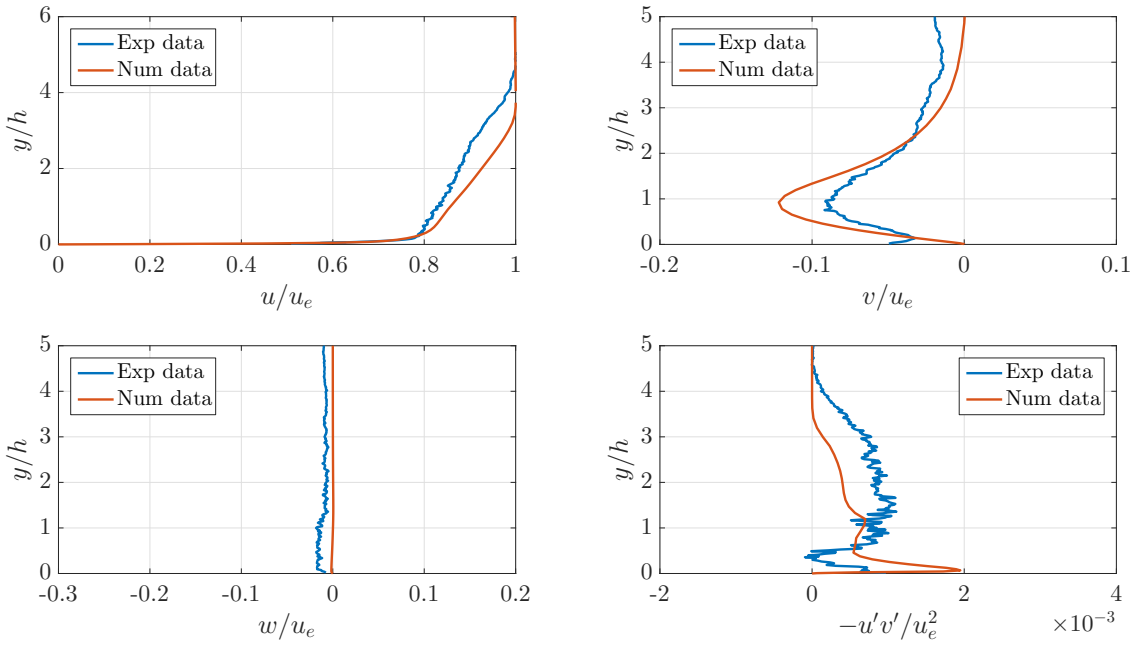

Figure 2.6: *Streamwise, wall-normal and spanwise velocity profile and Reynold's shear stress for vortex generator induced flow. At 10 device heights downstream of the VGs and spanwise position, $z/D = 0$*

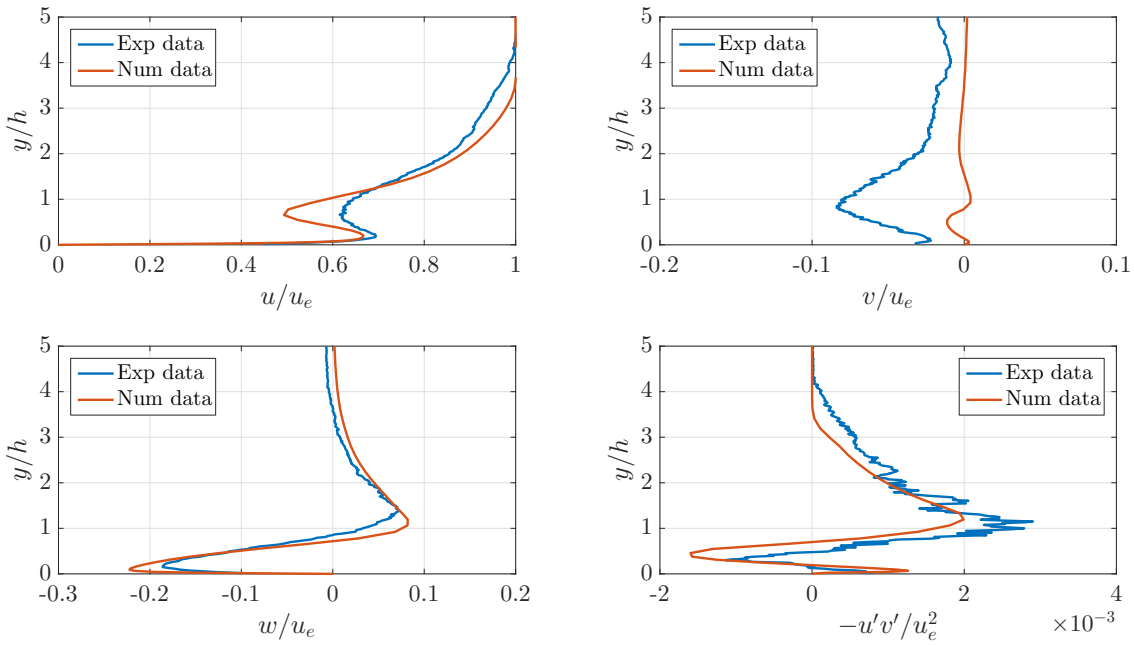

Figure 2.7: *Streamwise, wall-normal and spanwise velocity profile and Reynold's shear stress for vortex generator induced flow. At 10 device heights downstream of the VGs and spanwise position, $z/D = 0.208$*

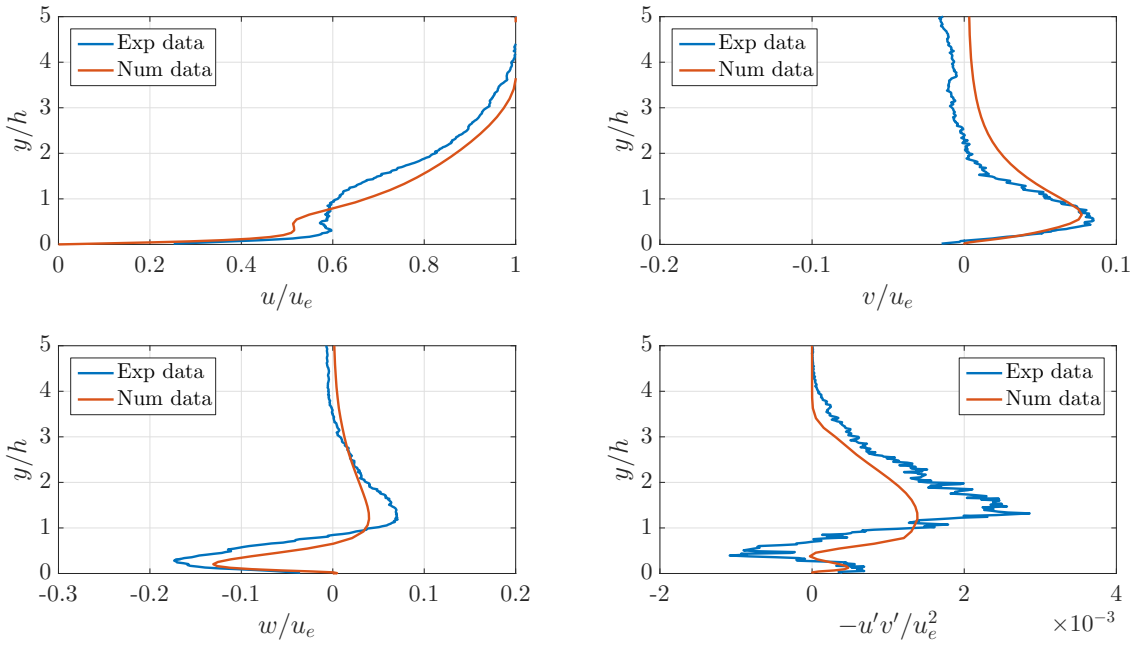

Figure 2.8: *Streamwise, wall-normal and spanwise velocity profile and Reynold's shear stress for vortex generator induced flow. At 10 device heights downstream of the VGs and spanwise position,* $z/D = 0.333$

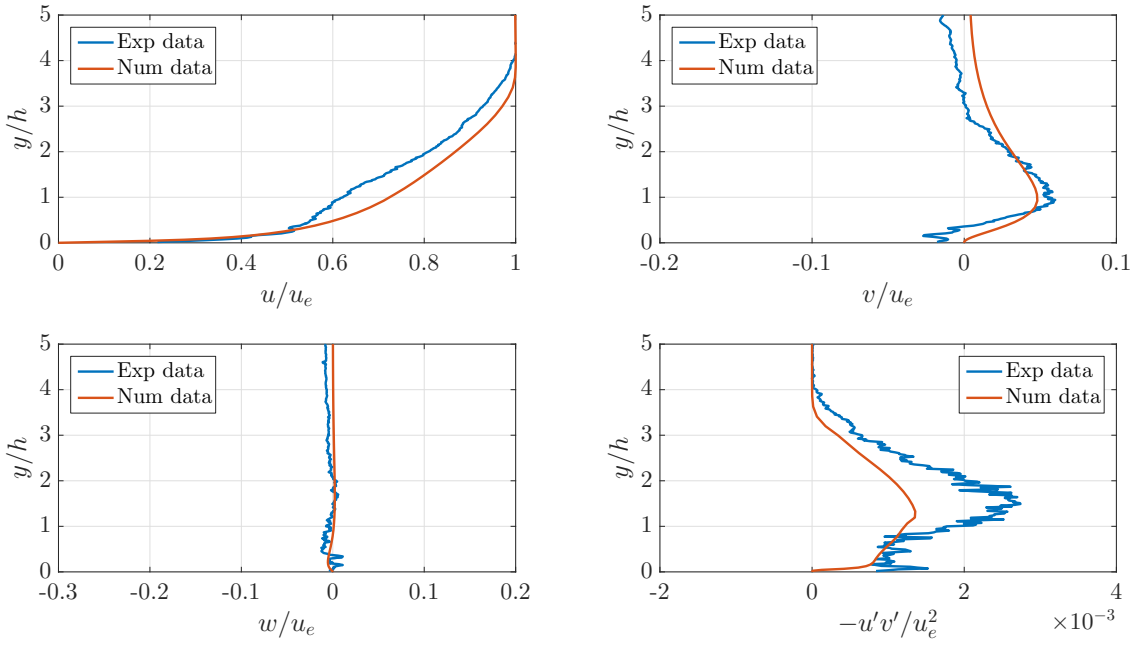

Figure 2.9: *Streamwise, wall-normal and spanwise velocity profile and Reynold's shear stress for vortex generator induced flow. At 10 device heights downstream of the VGs and spanwise position,* $z/D = 0.5$

Chapter 3

Methodology

This chapter will examine two-dimensional integral boundary layer (IBL) solution methods and identify the relevant IBL parameters. Another major goal is to examine different estimation methods and closure relations of the relevant IBL parameters. The widely accepted dimensionless integral boundary layer relations for the steady, incompressible flow with no mass transfer of the both relations are considered. A detailed approach is laid out.

3.1 Brief introduction to two dimensional integral boundary layer solution methods

The integral momentum relation first derived by Kármán [24] and the integral kinetic energy relation first derived by Leibenson [28] are presented as equations 3.1 and 3.2 respectively.

$$\frac{d\theta}{dx} + (H+2)\frac{\theta}{u_e}\frac{du_e}{dx} = \frac{C_f}{2} \tag{3.1}$$

$$\frac{d\theta^*}{dx} + (3)\frac{\theta^*}{u_e}\frac{du_e}{dx} = 2C_{\mathcal{D}} \tag{3.2}$$

The dimensionless parameters have been defined as,

θ, momentum thickness

$$\theta \equiv \int_0^{y_e} \frac{u}{u_e}\left(1 - \frac{u}{u_e}\right)dy \tag{3.3}$$

δ^*, displacement thickness

$$\delta^* \equiv \int_0^{y_e} \left(1 - \frac{u}{u_e}\right) dy \tag{3.4}$$

H, shape parameter

$$H \equiv \frac{\delta^*}{\theta} \tag{3.5}$$

C_f, skin-friction coefficient

$$C_f \equiv \frac{\tau_w}{0.5 \times \rho u_e^2} \tag{3.6}$$

θ^*, kinetic energy thickness

$$\theta^* \equiv \int_0^{y_e} \frac{u}{u_e} \left(1 - \frac{u^2}{u_e^2}\right) \tag{3.7}$$

H^*, kinetic energy shape parameter

$$H^* \equiv \frac{\theta^*}{\theta} \tag{3.8}$$

$C_{\mathcal{D}}$, dissipation (viscous) coefficient

$$C_{\mathcal{D}} \equiv \frac{\mathcal{D}}{\rho u_e^3} \tag{3.9}$$

where,

$$\mathcal{D} = \int_0^{y_e} \tau \frac{\partial u}{\partial y} dy = \int_0^{y_e} (\mu + \mu_t) \left(\frac{\partial u}{\partial y}\right)^2 dy \tag{3.10}$$

Classical integral boundary layer methods so called *one-equation integral methods* (for instance the correlation method of Thwaites, White's equilibrium method) integrate the momentum equation for the solution. Later, so called *two-equation integral methods* (for instance Le Balleur [27], Whitfield et al. [57], Drela and Giles [16]) were developed which integrate both the momentum equation (3.1) and also the kinetic energy equation (3.2) for

representing the behaviour of a separated boundary layer more accurately. Furthermore, *two-equation integral methods* are considered more accurate than the *one-equation integral methods*, especially for turbulent flow (Drela [15]). Other approaches of solving the *two-equation integral methods* are the *entrainment method* (for instance [23]) which based on an entrainment function and *momentum of momentum method* which based on shear stress integral function.

Buschmann [9] compares the *dissipation integral*, *entrainment* and *momentum of momentum* methods to calculate turbulent boundary layer properties. And states that the *dissipation integral* and *momentum of momentum* methods consider the shear stress distribution in the entire boundary layer. Thus, it satisfies the integral balance of kinetic energy. The *entrainment* method considers shear stress distribution only at the outer edge. Dissipation integral method of Drela and Giles [16] is widely analysed and numerically stable. Author admittedly biased from the beginning chooses Drela and Giles [16] method as integral solution method for current thesis work.

Drela and Giles [16] integrates the kinetic energy equation (3.2) by combining [equation (3.2)/θ^*] - [equation (3.1)/θ] which gives the kinetic energy shape parameter equation 3.1.

$$\theta\frac{dH^*}{dx} + \left(H^*\left(1-H\right)\right)\frac{\theta}{u_e}\frac{du_e}{dx} = 2C_D - H^*\frac{C_f}{2} \tag{3.11}$$

3.1.1 Integral thickness interpretation and shape parameters

When a uniform flow field with velocity approaches the leading edge of body/flat plate the due to viscous shear, and a viscous boundary layer is created. The flow near the surface is retarded so that the streamlines must be displaced outwards to satisfy continuity. The distance the solid surface would have to be moved to maintain the same mass flow rate is called the displacement thickness. In principle, the mass flux deficit. Similarly, the total flux loss of the momentum flux is equivalent to the removal of momentum through a distance θ, momentum thickness. The total flux of the kinetic energy flux loss is equal to the elimination of the kinetic energy through a distance, θ^*. Interpretation of the integral thickness for incompressible flow, in terms of the geometry of the normalised velocity profile (u/u_e) is plotted in figure 3.1.

Shape parameters is generally greater than unity based on the definition.

$$1 - \frac{u}{u_e} > \frac{u}{u_e}\left(1 - \frac{u}{u_e}\right)$$

$$\frac{u}{u_e}\left(1 - \frac{u^2}{{u^2}_e}\right) > \frac{u}{u_e}\left(1 - \frac{u}{u_e}\right)$$

3.1.2 Determining integral parameters from discrete data

Titchener et al. [52] states the maximum error in determining the boundary-layer integral parameters due to the discrete nature of datasets is proportional to distance between the

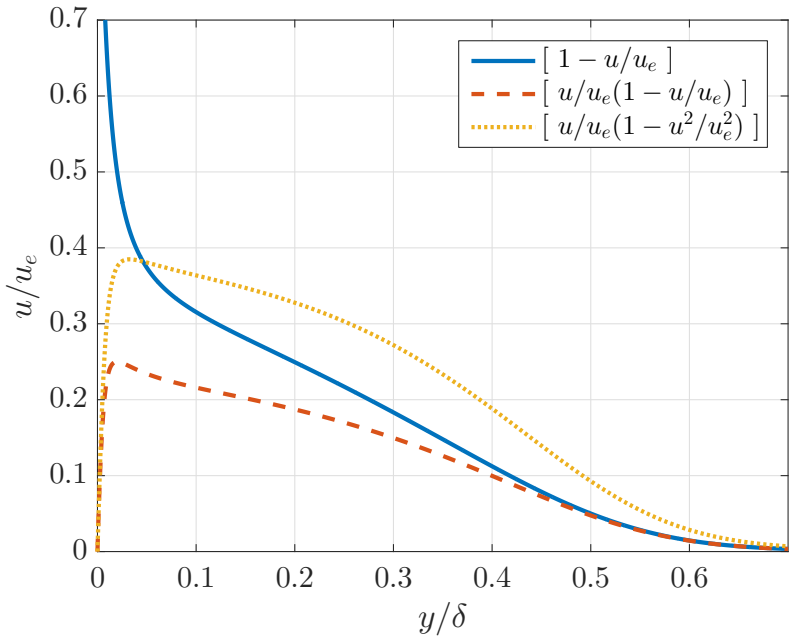

Figure 3.1: *Interpretation of the integral thickness for incompressible flow, in terms of the geometry of the normalised velocity profile (u/u_e). Schematic inspired from Drela [15] and García [20]*

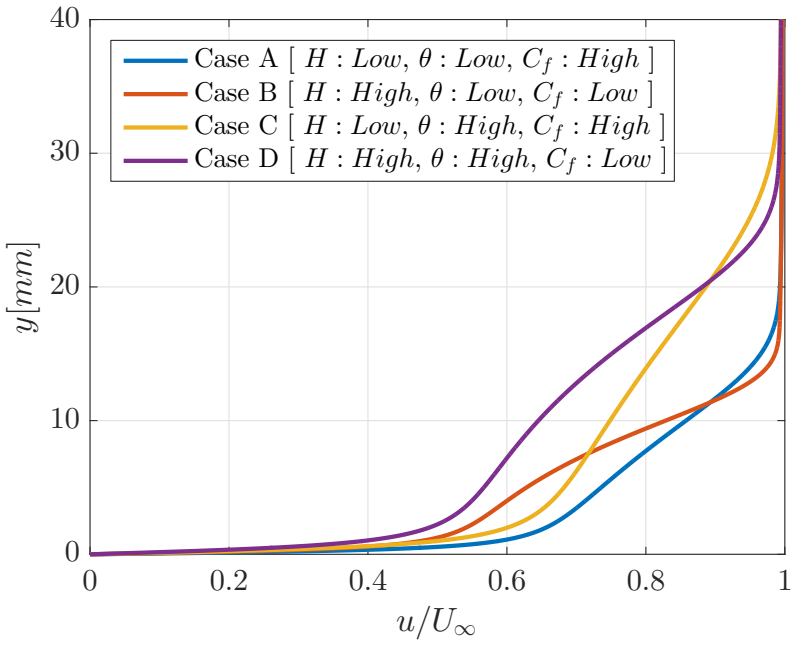

Figure 3.2: *Representation of velocity profile for different shape parameter and momentum thickness using Swafford velocity profile relation*

wall and first data point. It is an important issue for the experimental dataset (see section 2.2). Based on Titchener et al. [52] no-slip condition is enforced and trapezium rule is implemented for integration. Another important factor is choosing finite-difference approximation scheme. As the flow is wall-bounded, only one-sided approaches are possible. The most straight forward way to determine, $\partial u/\partial y$ first-order forward difference scheme. Titchener et al. [52] states if number data points available within control volume 20-40 it is. In the lower range, a logarithmic spacing is preferable. However, problem arises in determining the dissipation coefficient (see section 3.4).

3.2 Drela and Giles [16] turbulent closure relations

Turbulent closure relation used in Drela and Giles [16] is studied in this section.

Kinetic energy shape parameter,

$$\begin{aligned} H^* &= 1.505 + \tfrac{4}{\mathrm{Re}\theta} + \left(0.165 - \tfrac{1.6}{\mathrm{Re}_\theta^{0.5}}\right)\tfrac{(H_0-H_k)^{1.6}}{H}, && H < H_0 \\ &= 1.505 + \tfrac{4}{\mathrm{Re}_\theta} + (H-H_0)^2\left[\tfrac{0.04}{H} + \tfrac{0.007\log \mathrm{Re}_\theta}{(H-H_0+4/\log \mathrm{Re}_\theta)^2}\right], && H > H_0 \end{aligned} \tag{3.12}$$

where,

$$\begin{aligned} H_0 &= 4, && \mathrm{Re}_\theta < 400 \\ &= 3 + \tfrac{400}{\mathrm{Re}_\theta} && \mathrm{Re}_\theta > 400 \end{aligned}$$

$$u^+ = \frac{s}{0.09}\tan^{-1}\left(0.09y^+\right) + \left(u_e^+ - \frac{s\pi}{0.18}\right)\tanh^{1/2}\left[a\left(\frac{y}{\theta}\right)^b\right] \tag{3.13}$$

where, $s = c_f/\left|c_f\right|$, a & b are

Swafford [49]

closure relation for skin-friction coefficient.

$$Statesc_f = \frac{0.3e^{-1.33H}}{(\log_{10}\mathrm{Re}_\theta)^{1.74+0.31H}} + \left(1.1\times10^{-4}\right)\left[\tanh\left(4 - \frac{H}{0.875}\right) - 1\right] \tag{3.14}$$

Skin-friction closure relation is derived by Coles' Law of the Wall-Law of the Wake and empirically fitting.

$$u^+ \approx \frac{1}{k}\ln\left(y^+\right) + B + \frac{2\Pi}{k}f\left(\frac{y}{\delta}\right) \tag{3.15}$$

First term, is White [55] closure relation for skin-friction coefficient, which derived from Coles [13].

Dissipation coefficient closure relation used is discussed in section 3.4), after introducing basic concepts.

3.3 Skin Friction

Skin friction closure relations are quite exhaustive, few relations are chosen. A brute approach of comparing the accuracy each relations using Osterlund database is adopted.

3.3.1 Limited survey of estimation methods and closure relations

Gradient Method

It is a direct method based on the definition, however, it not clear in literature to what extent the upper limit can be considered. It varies from three to eight wall units.

$$\tau_w = \mu \left(\frac{\partial u}{\partial y} \right)_{y=0}$$

Ludwieg and Tillmann [32]

Researchers have moved away from Ludwieg and Tillmann [32] citing the failure in predicting sStateskin-friction coefficient for separated flows. In principle, VGIF should be attached at least in some regions. Validity will be checked for attached flow, if valid. It will be used attached regimes of VGIF, to test if VGIF exhibits similar behaviour as smooth wall-bounded flows.

$$C_f = 0.246 \left(10^{-0.678H}\right) \mathrm{Re}_\theta^{-0.268} \tag{3.16}$$

White [55]

White [55] is derived directly from Coles [13].

$$c_f = \frac{0.3e^{-1.33H}}{\left(\log_{10}\mathrm{Re}_\theta\right)^{1.74+0.31H}} \tag{3.17}$$

3.3.2 Limited survey of velocity profile expressions

Another approach is Kendall and Koochesfahani [25], and it employs a model velocity expression. Hence, it is nice to compare the accuracy of different model velocity expression. Again, model velocity expression are exhaustive; few are chosen and compared with Österlund database. States

Spalding [46]

$$y^+ = u^+ + \exp\left(-kB\right) \left[\exp\left(ku^+\right) - 1 - ku^+ - \frac{\left(ku^+\right)^2}{2} - \frac{\left(ku^+\right)^3}{6} \right] \tag{3.18}$$

Musker [35]

Musker [35] derived a closed-form expression for the velocity distribution over a smooth wall based on the eddy viscosity model. It satisfies both the momentum ad continuity equations near the wall while satisfying the four boundary conditions: $y = 0$, $u = 0$ and $du_+/dy_+ = 1$; $y = \delta$, $u = U_\infty$ and $du/dy = 0$. (For $y = \delta$, $y_+ \longrightarrow \infty$ is regarded as a limiting boundary condition.)

$$\begin{aligned} u^+_{Musker} = 5.424\tan^{-1}\left[\frac{\left(2y^+-8.15\right)}{16.7}\right] + \log_{10}\left[\frac{\left(y^++10.6\right)^{9.6}}{\left(y^{+2}-8.15y^++86\right)^2}\right] - 3.52 \\ +2.44\times\left\{\Pi\left[6\left(\tfrac{y}{\delta}\right)^2 - 4\left(\tfrac{y}{\delta}\right)^3\right] + \left[\left(\tfrac{y}{\delta}\right)^2\left(1-\tfrac{y}{\delta}\right)\right]\right\} \end{aligned} \tag{3.19}$$

Nickels [37]

Schubauer and Spangenberg [45] suggests, the downstream of VGIF acts if upstream had favourable pressure gradient. With Nickels [37] the van Karman constants can be adjusted in the explicit form. Also, it is a more modern velocity profile expression which is well accepted as well.

$$\begin{aligned} &u^+_{Nickels} = y^+_c\left[1-\left(1+2\tfrac{y^+}{y^+_c}\right)+\tfrac{1}{2}\left(3-p^+_x y^+_c\right)\left(\tfrac{y^+}{y^+_c}\right)^2 - \tfrac{3}{2}p^+_x y^+_c\left(\tfrac{y^+}{y^+_c}\right)^3\right] \\ &\times\exp\left(-3\tfrac{y^+}{y^+_c}\right) + \tfrac{\sqrt{1-p^+_x y^+_c}}{6\kappa}\ln\left(\tfrac{1+\left(0.6\left(y^+/y^+_c\right)\right)^6}{1+\eta^6}\right) \\ &+\tfrac{2\Pi}{\kappa}\left[1-\exp\left(-\tfrac{5\left(\eta^4+\eta^8\right)}{1+5\eta^3}\right)\right] \end{aligned} \tag{3.20}$$

where,

$$p^+_x = \frac{\nu}{\rho\mu^3_\tau}\frac{dp}{dx}$$

$$p^+_x y^{+3}_c + y^{d+2}_c - R^2_c = 0 \tag{3.21}$$

Velocity profiles comparison with Österlund database

Percentage error is is determined by equations 3.22 and 3.23. Here n indicates the number of velocity data in the normal direction and m indicates the number of the experimental data set. It is tabulated in Table 3.1.

$$error^j_{model} = \frac{1}{n}\sum_{i=1}^{n}\left|1-\frac{u^+_{i,model}}{u^+_{i,experimental}}\right| \tag{3.22}$$

$$Error_{model}\,(\%) = 100\times\frac{1}{m}\sum_{j=1}^{m} error^j_{model} \tag{3.23}$$

Velocity Profile	Remarks	Error %
Spalding	$k = 0.41$, $B = 5$	3.78%
Musker	$k = 0.41$, $B = 5$	0.53%
Swafford	No-slip condition added Trapezoidal numerical integration	4.39%
Nickels	$k = 0.39$, $B = 4.32$	0.67%

Table 3.1: *Comparison of velocity profile relations w.r.t to Österlund dataset*

It was widely accepted to use von Kármán constant, $k = 0.40 - 0.41$ and the intercept constant, $B = 5.0 - 5.5$. In recent times lot of researchers suggest different values. Interestingly Österlund et al. [41] based on two independent experimental investigations, one being current database used for comparison suggested $k = 0.38$ and $B = 4.1$. However, limits of the log law change with researchers. Musker [35] formulated the analytical expression, with log-law constants $k = 0.41$ and $B = 5$ as recommend by Coles [12] at the Stanford Conference. Nickels [37] suggests to use $k = 0.39$ and $B = 4.32$. Using Österlund et al. [41] constant values, worse results for (4.14 %) Spalding [46] and better results (0.33 %) for Nickels [37] profile. Probably, fit is determined by using the van Karman constants at that time. It makes sense to use the same von Kármán as original research.

3.3.3 Skin-friction coefficient closure relations compared using Österlund database

Österlund database

Österlund [40] conducted experimental investigations for high Reynolds number turbulent boundary layers at zero pressure gradient. The researcher employed an oil-interferometry technique to determine the skin friction, it is independent of the law-of-the-wall. It is a direct and absolute measurement of the skin-friction coefficient. The technique consists of measuring the thinning rate of an oil film as it is being acted upon by the wall shear. Since the database is open, supplemented by direct and independent skin friction measurements. Many researchers (more than 250 citations) have used the experimental database to test scaling laws and methods to extract the skin friction. Percentage error determined by equation 3.24 is tabulated in table 3.2 . Here m indicates number of the experimental data set.

$$Error_{model}\,(\%) = 100 \times \frac{1}{m}\sum_{j=1}^{m}\left|1 - \frac{C^{j}_{f,model}}{C^{j}_{f,experimental}}\right| \tag{3.24}$$

3.4 Dissipation coefficient

The dissipation coefficient $\mathcal{D}$ as per Drela [15] measures the local rate of flow kinetic energy dissipation into heat by the shear stress, τ acting on the fluid which is deforming

Method / Closure Relation	Error %
Kendall and Koochesfahani [25]; Upper limit $y+ <= 500$	0.12%
Kendall and Koochesfahani [25]; Upper limit $y+ <= 50$	−0.16%
Swafford [49]	−1.21%
Ludwieg and Tillmann [32]	−0.73%
White [55]	2.54%

Table 3.2: *Comparison of skin-friction coefficient estimation methods.*

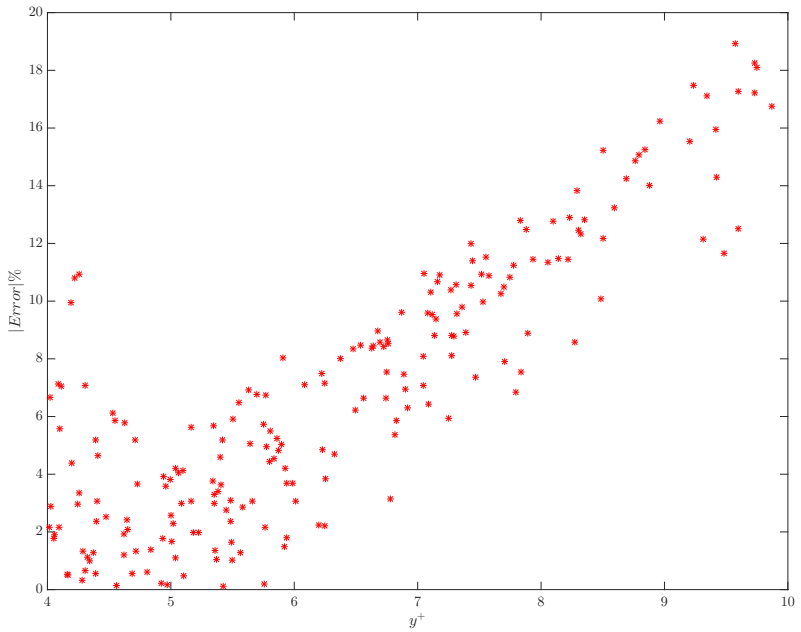

Figure 3.3: *Error in determining skin-friction coefficient using gradient method for different wall units,y^+ as upper limit.*

at the shear strain rate $\partial u/\partial y$. For a 2D steady, incompressible flow with no mass transfer, dissipation integral can be represented as equation 3.25.

$$\mathcal{D} = \int_0^{y_e} \left(\mu \frac{\partial u}{\partial y} - \rho \overline{u'v'} \right) \frac{\partial u}{\partial y} dy \tag{3.25}$$

Dissipation integral consists of the *direct dissipation function* : Depend solely on the velocity gradient of the mean motion and *turbulent dissipation function*: It is energy dissipated by the virtue of the existence of the fluctuations. Classically, dissipation coefficient was determined using empirical closure relations based on $-\rho\overline{u'v'}(du/dy)$. $\mu(du/dy)^2$ is often neglected, considering contribution $C_{\mathcal{D}}$ is small expect close to the wall.

Truckenbrodt [53], empirical dissipation integral coefficient

$$C_{\mathcal{D}} = 0.0056(\mathrm{Re}_\theta)^{-1/6}$$

Dissipation coefficient can be also determined based on *velocity profile models*. Whitfield [56] analytically integrating the inner layer ($0 \leq y^+ \leq 100$) considering $\tau = \tau_w$ and outer layer numerically.

$$C_{\mathcal{D}} = 2 \times \left(0.009 - 0.011 e^{-0.15H^{2.1}} + 3.0 \times 10^{-5} e^{0.117H^2} + A(\mathrm{Re}_\theta)^{-0.574} \right) \tag{3.26}$$

where,

$$A = 0.438 - 280H \, for H \leq 3.5$$

$$A = 0.160(H - 3.5) - 0.550 for H \geq 3.5$$

Le Balleur [27] / Thomas [51] use *slip velocity concept*, it stems from the eddy viscosity formulation of Clauser [11] equilibrium turbulence models. It determines dissipation coefficient as the sum of contributions from the inner(wall) and outer(wake) regions of the boundary layer. For non-equilibrium flow (Large adverse pressure gradient, APG or relaxing flow, where APG is suddenly removed), separated flows *slip velocity concept* using Clauser [11] experimental value fails. Relaxation factor is added to account for the upstream history effects .Drela and Giles [16] also implements the *slip velocity concept* with relaxation, however directly uses the Clauser [11] empirical closure relations.

$$C_D\,[DCR] = \underbrace{\frac{C_f}{2} U_s}_{Wall(Inner)\ layer\ contribution} + \underbrace{C_\tau (1 - U_s)}_{Wake(Outer)\ layer\ contribution} \tag{3.27}$$

$$C_{\tau,eq} = \frac{1}{1 - U_s} \frac{H^*}{2} \left(\frac{H - 1}{H} \right)^3 \frac{1}{A^2 B} \tag{3.28}$$

$$U_s = \frac{H^*}{2} \left(\frac{1}{B \cdot H} + \frac{B - 1}{B} \right) \tag{3.29}$$

$$\beta \equiv \frac{\delta^*}{\tau_w}\frac{dp}{dx} = -\frac{2}{C_f}\frac{\delta^*}{u_e}\frac{du_e}{dx} \tag{3.30}$$

$$G \equiv \frac{H-1}{H}\frac{1}{\sqrt{C_f/2}} \tag{3.31}$$

An empirical expression for this relationship is,

$$G = 6.7\sqrt{1+0.75\beta} \tag{3.32}$$

In Drela [14] uses Green et al. [23] for better predictions of lift and drag near stall conditons.

$$\frac{\delta}{C_\tau}\frac{dC_\tau}{dx} = 5.6\left(C_{\tau,eq}^{1/2} - C_\tau^{1/2}\right) + 2\delta\left\{\frac{4}{3\delta^*}\left[\frac{C_f}{2} - \left(\frac{H_k-1}{6.7H_k}\right)^2\right] - \frac{1}{u_e}\frac{du_e}{dx}\right\} \tag{3.33}$$

From the Green et al. [23],

$$C_\tau = \frac{1}{u_e^2}\left(-\overline{u'v'}\right)_{\max} \tag{3.34}$$

From Drela [14], Drela and Giles [16] it is not quite explicitly, mentioned how to determine effective slip velocity parameter. An assumption is made that U_s at maximum and C_{tau} and is valid (see figure 3.4).

$$U_s = \frac{u_{\left(-\overline{u'v'}\right)_{\max}}}{u_e} \tag{3.35}$$

Upstream data from numerical dataset is used to compare the discussed dissipation coefficient relations. Dissipation coefficient obtained at streamwise location $(x - x_{vg})/h = -15$ and spanwise location $z/D = 0.333$ is tabulated in table 3.3. Similar trends were observed at $z/D = 0.5, 0.208, 0$

Method	Value
Dissipation integral ($\mu(du/dy)$, -$\rho\overline{u'v'}$)	0.001637
Dissipation integral (μ, μ_τ)	0.001559
Drela and Giles [16] (C_τ and U_s using closure relations)	0.001604
Drela and Giles [16] (C_τ and U_s from numerical dataset)	0.001600
[53]	0.001599
LeBaueller/Thomas	0.009096
White	0.003072

Table 3.3: *Comparison of dissipation coefficient, $C_\mathcal{D}$ using different relations. Upstream data (15 device height behind trailing edge of VGs) from numerical dataset is used.*

A first-order rearward difference finite scheme is applied to determine the dissipation integral. Dissipation integral is highly sensitive to scheme applied.

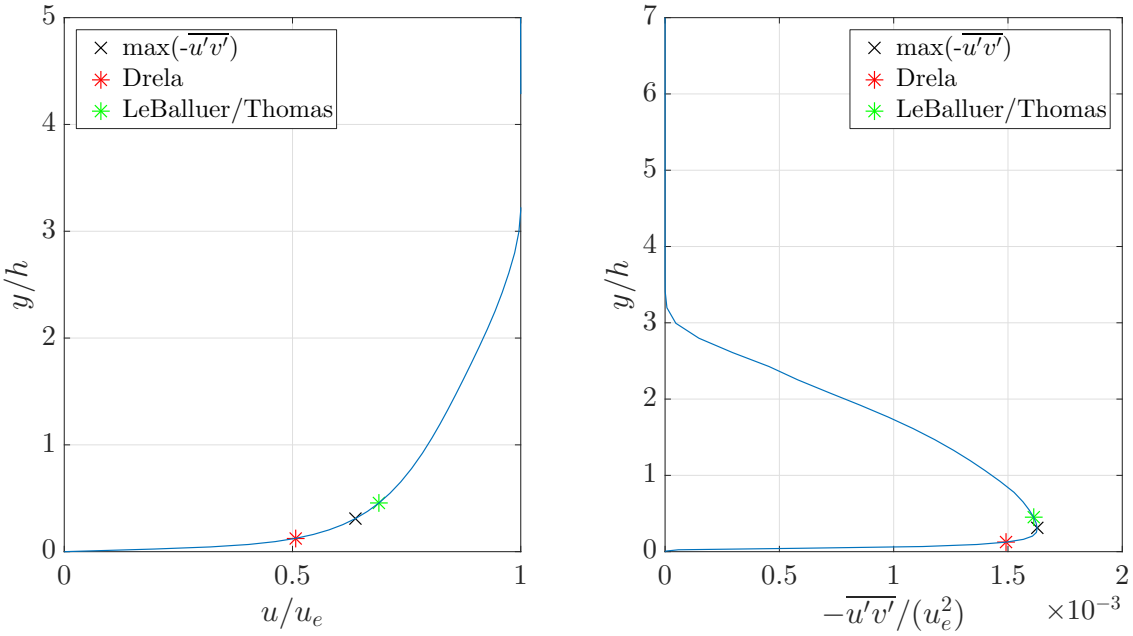
max(-$\overline{u'v'}$)
Drela
LeBalluer/Thomas
y/h
u/u_e
max(-$\overline{u'v'}$)
Drela
LeBalluer/Thomas
y/h
$-\overline{u'v'}/(u_e^2)$
$\times 10^{-3}$

Figure 3.4

3.5 The most relevant flow quality or qualities that describe a vortex generator induced flow

Ashill et al. [5] states that there are two ways to measure the effectiveness of vortex generator induced flow. The first idea, to check decrease of boundary-layer shape factor, H based on [45]. [45] states boundary downstream effect of closely spaced array VG acts in way VG created a favourable pressure gradient. However,Ashill et al. [5] quickly dismiss the idea stating it should have some sort of quasi-uniform effect. Suggests, this quasi-uniform effect can take place of the order of ten boundary-layer thickness. The second concept, based on the strength of the vortices and way the vortices decay downstream. Ashill et al. [3, 4] formulated correlation of non-dimensional circulation through using the idea of a effective device height, h_e. Lin [29] verified the claim and found out it is well correlated for all the VG devices

$$\frac{\Gamma(x)}{\mu_* h} = G\left(h^+, \frac{x - x_{vg}}{h}\right) \tag{3.36}$$

where, μ_* is the wall friction velocity in uncontrolled flow,

$$\mu_* = u_e\sqrt{C_f/2} \tag{3.37}$$

and h^+ is the dimensionless device height

$$h^+ = \frac{h\mu_*}{\upsilon} \tag{3.38}$$

In the review Ashill et al. [5] state that ESDU [17] claim streamwise rate of change of vortex strength or circulation of a single vortex downstream of a VG (or SBVG) is proportional to the lateral velocity induced at the wall by the vortex and local skin-friction coefficient.

$$\frac{d\Gamma}{dx} = -KC_f\frac{\Gamma}{h_v} \tag{3.39}$$

$$\Gamma/\Gamma_t = \exp\left(-KC_f\left(x - x_{vg}\right)/h_v\right) \tag{3.40}$$

Possibly, Kerho et al. [26] used this viewpoint, compared vortex generator enhanced mixing to increased turbulence production. And mimicked shear stress based on the strength of the vortices and way it decays downstream. ESDU [17] states for counter-rotating sub boundary-layer vortex generator configuration wall shear stress plays a more important role for determining the vortex strength and decay.

The key integral parameter:

1. Skin-friction coefficient
2. Shear stress coefficient

3. Effective slip-velocity parameter (Vortex trajectory)

To check for quasi-uniform effect $IBLP^{(u^z(x,y))}$ and $IBLP^z(x)$ should be equal, where

$$IBLP^z(x) = \frac{1}{D}\int_{-D/2}^{D/2} IBLP(x,z)\,dz$$

$$u^z(x,y) = \frac{1}{D}\int_{-D/2}^{D/2} u(x,y,z)\,dz \tag{3.41}$$

3.6 Detailed approach

Step 1 Skin-friction coefficient is an important parameter. Numerical simulations are fully resolved very close to the wall ($y^+ < 2$) and gradient method (see 3.3.1) will be used to estimate skin friction. It is quite accurate (see 3.3.3). However, for the experimental dataset, gradient method would result in an unacceptable level of error. As the first data point is away from the wall as well as uncertainty in determining wall-position. Kendall and Koochesfahani [25] and Swafford [49] will be tested with numerical data. A better method will be used to estimate skin friction from experimental dataset. Another motivation is to check if VGIF exhibit smooth wall bounded turbulence properties.

Step 2 Only Drela and Giles [16] kinetic energy shape parameter, H^* closure relation is considered. This will be tested. Additionally, it verifies if VGIF velocity profile matches Swafford's velocity expression.

Step 3 Effective slip velocity parameter hypothesis is made and verified at upstream location of VGs. Validity of the hypothesis at downstream locations of VGs will be investigated.

Step 4 Dissipation coefficient can be obtained either using Reynolds shear stress or eddy viscosity values. Results will be analysed and one method will be choosen.

Step 5 Integral boundary layer parameters of interest for VGIF will be compared against UCF. It will reveal if the VGIF is quasi-uniform, if the 3D mechanism is more predominant than 2D mechanism or vice versa. Also, will reveal if VGIF is equilibrium or non-equilibrium flow. This investigation will also act as a secondary validation of dataset and methods implemented.

Step 6 Behaviour of van Kármán integral momentum equation 3.1 and Kinetic energy shape parameter equation 3.11 for VGIF will be analysed. Skin-friction and dissipation coefficient obtained from reminder of the equations will be compared against experimental values and closure relations.

Step 7 The key integral parameter will be analysed.

Part III

Results and Discussion

Chapter 4

Integral Parameters' Estimations and Approximations from Experimental and Numerical Dataset

Two estimation methods for determining the skin-friction coefficient, C_f for vortex generator induced flow, VGIF from the numerical dataset are compared in section 4.1. The validity of Drela's closure relation, DCR for kinetic energy shape parameter, H^* is tested by comparing with Swafford velocity profile for VGIF from the numerical dataset in section **??**. Behaviour of effective slip assumption is checked for VGIF, how it effects dissipation coefficient, $C_{\mathcal{D}}$ from DCR **??**. Considering the uncertainties the downstream development of integral boundary layer parameters, (IBLP) is discussed in section 4.2.

4.1 Skin-friction coefficient estimation for vortex generator induced flow using velocity profile

A quote extracted from Örlü et al. [39] [1]

> .. wrongly become known as Galileo's rule about measurements, which states:
>
> Measure what is measurable, and (try to) make measurable what is not so (as yet).

Nagib et al. [36] concluded that the only wall-bounded flow that may not require an independent measurement of the mean shear stress is that of a fully developed pipe flow.

[1] Wrongly: Despite its widespread attribution to Galileo in "a large number of publications, the authenticity of the sentence is highly dubious because no one has ever provided a precise bibliographical reference for where to find it in Galileo's works "

Warns for three-dimensional non-equilibrium flows, the wall shear stress, could be estimated with a high order of inaccuracy by indirect techniques. Vortex generator induced flow is inherently being 3D flow and non-equilibrium (see sections) needs an independent measurement of the wall shear stress. However, drawing motivation from Örlü et al. [39] take on Galileo's rule about measurements. Indirect techniques are implemented on VGIF from numerical dataset to estimate skin-friction coefficient. Then, it is compared against skin-friction coefficient obtained from the gradient method. The comparison will give an indication if the VGIF follow or not follow the smooth wall turbulence properties. A better estimation method will be used to estimate skin-friction coefficient, C_f from experimental data.

Previously research papers that have successfully implemented VG in 2D IBL code Ashill et al. [3, 4] and Kerho et al. [26] do not mention experimental data skin friction coefficient for VGIF. To be fair, the implementation strategy does not require them. Ashill et al. [3, 4] use skin-friction from uncontrolled case. Kerho et al. [26] suggests the flow configuration has quasi-uniform effect hence, Swafford closure relation should be accurate. Lögdberg et al. [31] determined the spanwise-averaged skin-friction coefficient by considering the momentum loss (2D) of VG array. For few test cases, the wall is modelled from $y^+ = 5$ till $y^+ = 50$. This method is discussed more in detail in later section. In this section, two methods (see for motivation 3.6) are investigated.

The two methods are:

- Kendall and Koochesfahani [25] method using Musker [35] velocity expression.
- Swafford [49] closure relation for skin-friction coefficient.

4.1.1 Using Kendall and Koochesfahani [25] method

From section 2.3, there is an indication that the VGIF might not follow smooth wall velocity profile for entire boundary layer. Prospectively, the suspicion is confirmed (see figures). However, a hypothesis is made that will fifty wall units, follow smooth wall turbulent properties. The primary motivation is also Lögdberg et al. [31] used wall modelling and also from visual analysis of the velocity profiles.

A first step, Kendall and Koochesfahani [25] method is to the upper limit of fifty wall units. Increasing the ceiling decreased the accuracy and vice versa. As discussed before, the optimisation routine employs a *fractional difference* method, which gives more weight to points closer to the wall. Hence, decreasing the upper limit is of y^+ is essentially a biassed gradient method. Also, for the experimental measurements, the data points are close not the wall as the numerical simulations. The lower limit is also modified to check the effectiveness. As suspected, increasing the lower limit (more away from the wall) also decreased the accuracy and vice versa. The method is not effective. Nevertheless, it is implemented on the experimental dataset.

For the experimental dataset, the upper limit is varied from $y^+ < 500, 300, 100, 50, 30, 10$. By a cumbersome process [2] of checking the error value and visual inspecting the fit. The upper limit is set for 30 wall units, $y^+ < 30$. The corresponding lower limit range is

[2] By not documenting

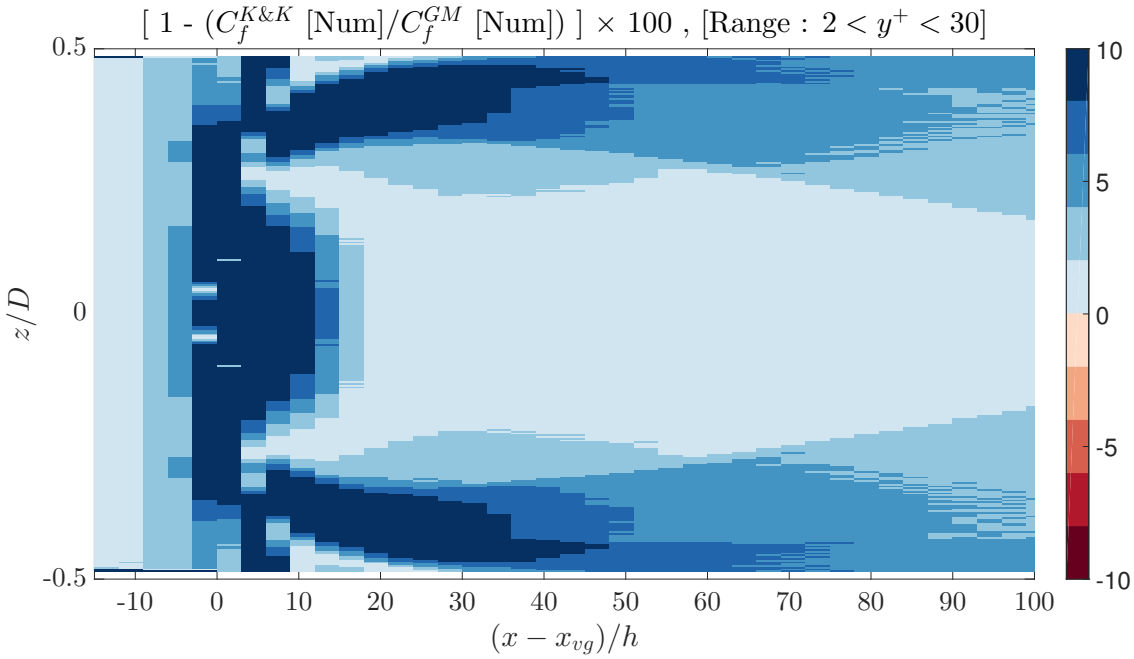

Figure 4.1: *Percentage error of skin-friction coefficient for vortex generator induced flow from numerical dataset. Skin-friction coefficient obtained using gradient method is considered as true value and from Kendall and Koochesfahani [25] as estimated value.*

varying from 4 to 8 wall units are different spanwise locations. K and K implemented with upper limit thirty wall units and a lower limit of two wall units is shown in the figure. Rest of the analysis in Appendix A.

Even though this exercise is not able to predict the skin-friction coefficient with reasonable limits, it has its own merits. Foremost confirming the Nagib et al. [36] warning for non-equilibrium 3D flows. Wall modelling up to fifty wall units by Lögdberg et al. [31] will give a bias. One drawback of this current exercise is using same van Kármán constants k 0.41 and B =5 (see the section for motivation). Nagib et al. [36] suggests van Kármán constants change in streamwise direction for non-equilibrium 3D flows. An attempt was made study the pattern and also to check the [45] hypothesis. The findings are non-conclusive. An important issue being, to which extent to which log law is valid and corresponding van Kármán constants . An effective way would be to measure skin friction independently and utilise Rodríguez-López et al. [44] optimisation routine to determine the variation of van Kármán constants.

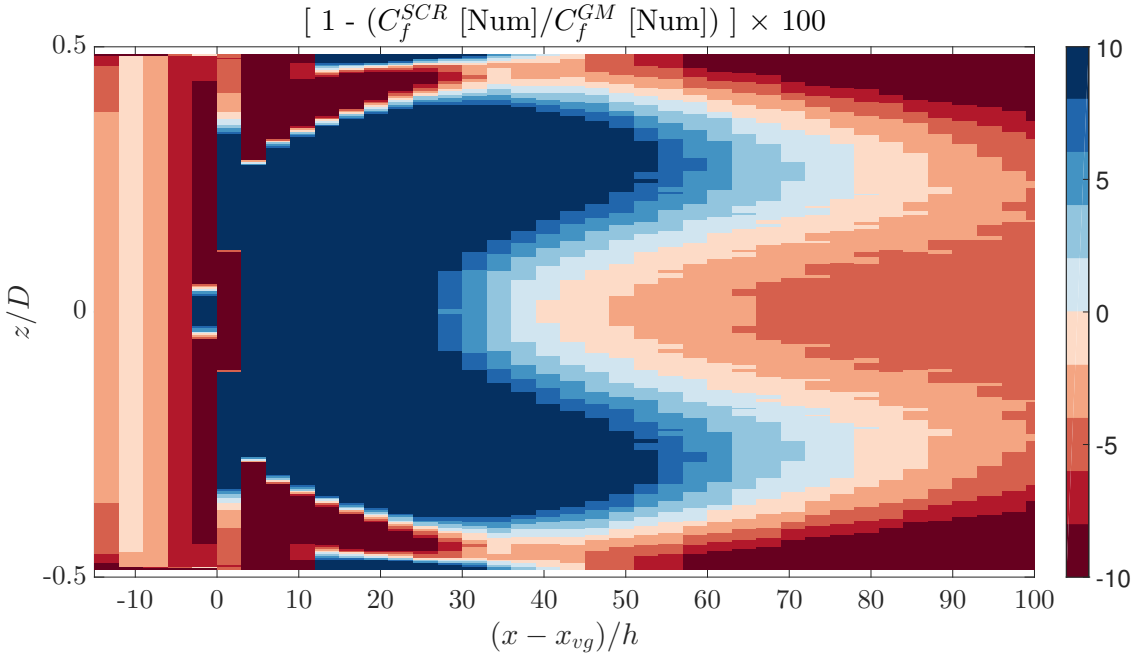

Figure 4.2

4.1.2 Using Swafford [49] closure relation

swafford1983analytical closure relation for skin-friction coefficient fails miserably close to trailing edge of VGs (see figure). Further upstream it is converging. As seen in sections, when the shape parameter, H is relatively high. For attached or separated smooth wall-bounded flow, indicates skin-friction is lower. The empirical relation was formulated using before mentioned data. Hence, higher value of H the skin-friction is lower. Also, swafford1983analytical closure relation main basis is from White (see section). White derived the closure relation basing on Coles' law of the wake (Coles [13]). In principle, the formulation is dependent if the VGIF follow Coles' law of the wake. From from figures it evident the VGIF doesn't follow the Coles [13].

4.1.3 Should we consider upstream effects for determining C_f for VGIF ?

It is widely accepted for smooth wall-bounded flow, the increase/decrease in skin-friction coefficient velocity is due to increase/decrease of near wall velocity rather than by a uniform, across-the-layer increase in eddy viscosity (see for reference, other literature also cite). Also, for smooth wall attached or separated flow, experimental evidence indicate smooth wall is not affected by upstream effects. Hence, closure relation is followed by 2D integral solution methods.

[19] related Reynolds stress distribution to the skin friction in wall-bounded flows, tested for controlled case (uniform wall blowing/suction) and indicated Reynolds stress away from the wall played more vital role compared to smooth wall bounded flow. To recall, Ludwig and Tilaman is discontinued as it was not predicting accurately separated flows.

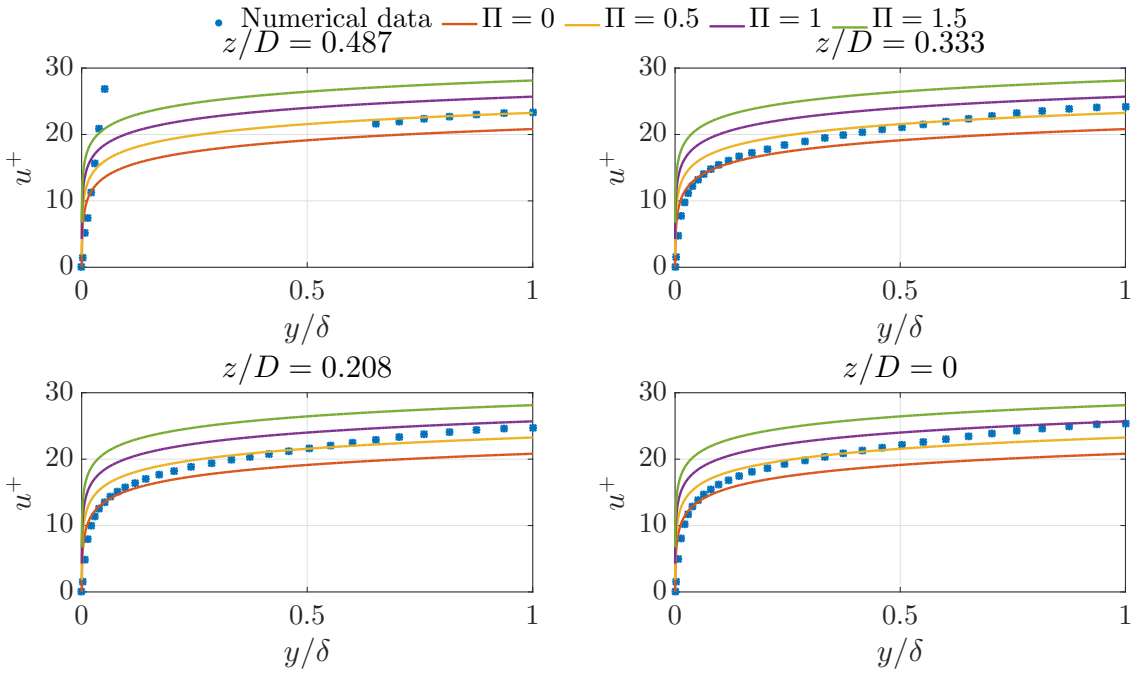

Figure 4.3: *Comparison of velocity profile for VG test case [numerical dataset] at* $(x - x_{VG})/h = -15$ *with Coles' wall-wake formula at different spanwise locations.*

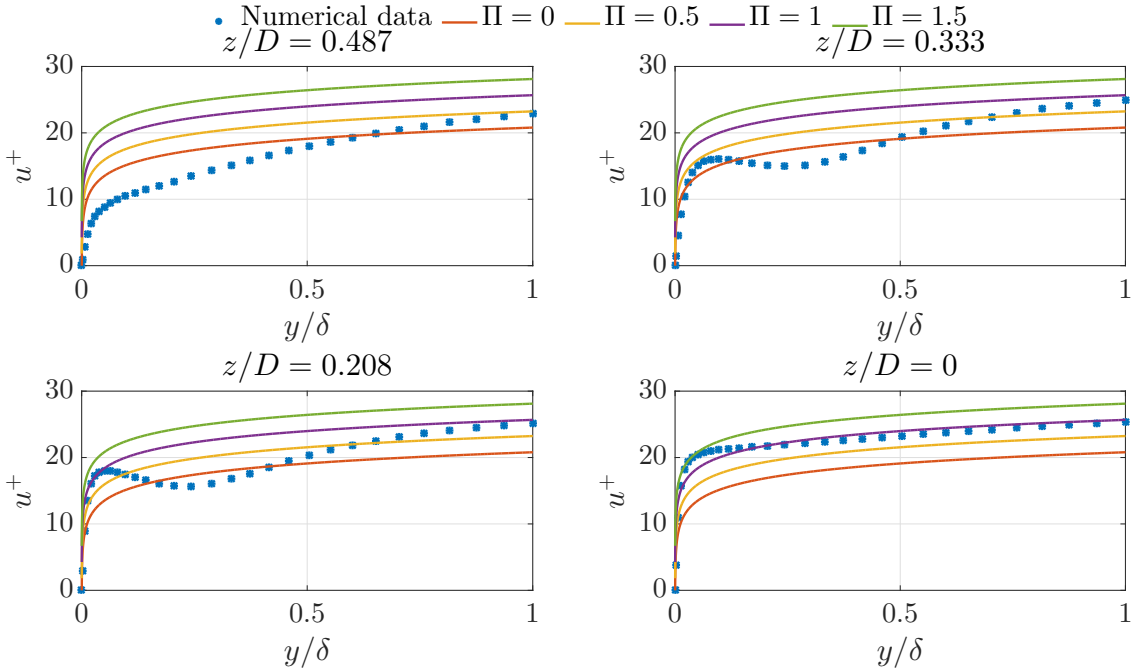

Figure 4.4: *Comparison of velocity profile for VG test case [numerical dataset] at* $(x - x_{VG})/h = 10$ *with Coles' wall-wake formula at different spanwise locations.*

This is tested for VGIF flow, probaly the constants are changed due to. Nagib also States residual history of the upstream two-dimensional turbulent boundary layer still present in the developing 3DTB, no further explanation is provided.

This page is intentionally left blank.

4.2 Downstream development of integral parameters of interest

First, let us consider the integral parameters of interest for the uncontrolled case from the experimental dataset. At downstream locations due to retardation of the flow by viscous forces, the boundary layer grows. Therefore, the integral thickness also increase. It can also be interpreted as dwindling of the turbulent mixing effects, and it reflected in lower shear stress coefficient values. Due to reduced mixing, the high velocity pushed towards the wall also decrease. Thus, the skin-friction coefficient is lower. As the viscous shear and turbulent mixing effect are decreasing the dissipation coefficient decreases as well. It might seem shape parameter, decreasing with the decrease in turbulent mixing effect is wrong. However, it is not.

Drawing inspiration from Kerho et al. [26] [3], enhanced mixing effect of VGs could be compared the difference between laminar to the turbulent regime. Due to enhanced mixing effects, higher speed fluid is brought closer to the wall at a higher rate. Consequently, the skin friction increases, shear stress coefficient increases, dissipation coefficient increase. Displacement thickness would decrease due to higher mixing rate thus bringing down the mass flux deficit. Momentum increases and kinetic energy thickness would increase due to mixing. Skin-friction, shear stress and dissipation coefficient also increase due to mixing. Lower shape parameter, H is expected as displacement thickness reduces and momentum thickness increases. Hence, the closure relations for skin-friction should be at least qualitatively correct.

Let us consider spanwise averaged values of the integral parameters of interest as well integral parameters of interest. For the experimental dataset, VGIF is compared against uncontrolled cases. For numerical dataset, the upstream locations are compared against downstream of VGs. Displacement thickness, contrary to laminar to turbulent transition, is higher and tend to decrease at fifty device heights downstream of trailing edge of VGs. Other integral thickness, increase due to vortex generation and enhanced mixing. Interestingly, both the shape parameters show a reverse trend, only till twenty device height downstream of the VGs. Shear stress coefficient also have a dip around the same downstream location and consequently reflected in the dissipation coefficient.

To check for the quasi-uniform effects, let us compare the spanwise averaged integral parameters against integral parameters obtained from spanwise averaged velocity profiles. Displacement thickness is quasi-uniform but indicating it is different from just enhanced mixing; meaning the streamwise vortices increase the mass flux deficit. Momentum and energy thickness tend to converge at hundred device heights downstream of VGs. Shear stress and dissipation coefficient have strong, effect indicating 3D mechanism.

Non-quasi-uniform properties other the displacement thickness and skin-friction coefficient raises doubts about the wake rake measurements done at the centerline and Squire Young law for VGIF. Ashill et al. [5] raises claim about wake survey technique, both the quotes are extracted from section 3.2.1.3 *Device drag.* "On the other hand, the wake survey technique gives relatively large errors, since it involves the subtraction of two large

[3] In the original paper, for the experimental configuration the flow exhibited quasi-uniform effects. Enhanced mixing effect of VGs was the same as turbulent mixing effect Author is merely using this approach of analysis as the first step

numbers, owing to the way the device [4] affects the spanwise distribution of boundary layer momentum thickness"and "However, regarding relative magnitude of drag, the two sets[5] of results are consistent, bearing in mind the lack of accuracy of the wake survey technique ". For Kerho et al. [26] experiments the flow exhibits quasi-uniform effects, hence in principle wake rake measurements should not effect it. Lin [29] experiments use a force balance method to measure drag.

From previous sections, it quite clear at the plane of symmetry, $z/D = 0$ fuller velocity profile and mid-distance of the devices, $z/D = 0.5$ emptier profile. Consequently, higher skin-friction coefficient, lower skin-friction coefficient at the plane of symmetry and vice-versa. Contrary to uniform enhanced mixing, momentum and kinetic energy show opposite trends. However, it indicates the trend as expected as per counter-rotating VG mechanism.

At plane of the symmetry, the integral thickness increases sharply at the trailing of VGs, then decrease. Ashill et al. [5] explained stating that close to trailing edge of the device the vortex height is similar to VG height. The vortices sweep low energy air from the either side of them into the boundary on the plane of symmetry. Further, downstream ($z/D = 30$), the vortices rise under mutual induction, then vortices pull in higher energy air and lower energy air is pushed out into the main flow.

[4] Vortex Generators

[5] Two sets : skin-friction balance measurements and wake-survey technique same configuration. h/δ are different for two sets due to the experimental configuration, hence refrains from comparing directly.

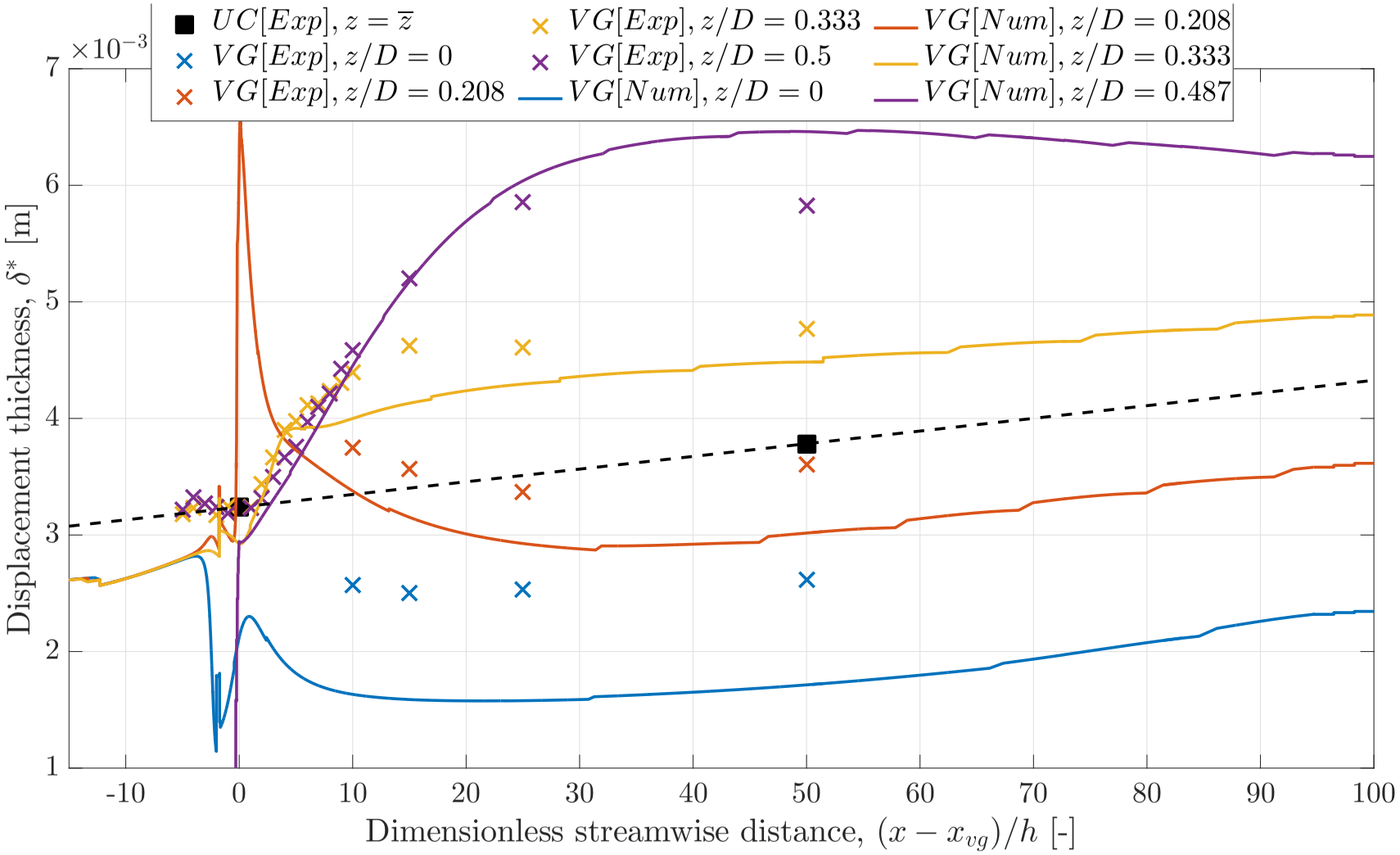

Figure 4.5: *Displacement thickness, δ^* [m] development in streamwise direction for uncontrolled (UC) case and vortex generator (VG) case from experimental (Exp) and numerical (Num) dataset. For UC case from Exp dataset : Spanwise averaged ($z/D = \overline{z}$), for VG case from Exp dataset : ($z/D/D = 0, 0.208, 0.333, 0.5$) and for VG case from Num dataset : ($z/D = 0, 0.208, 0.333, 0.487$). Streamwise distance, x is dimensionalised by VG trailing edge location, x_{vg} and VG height, h.*

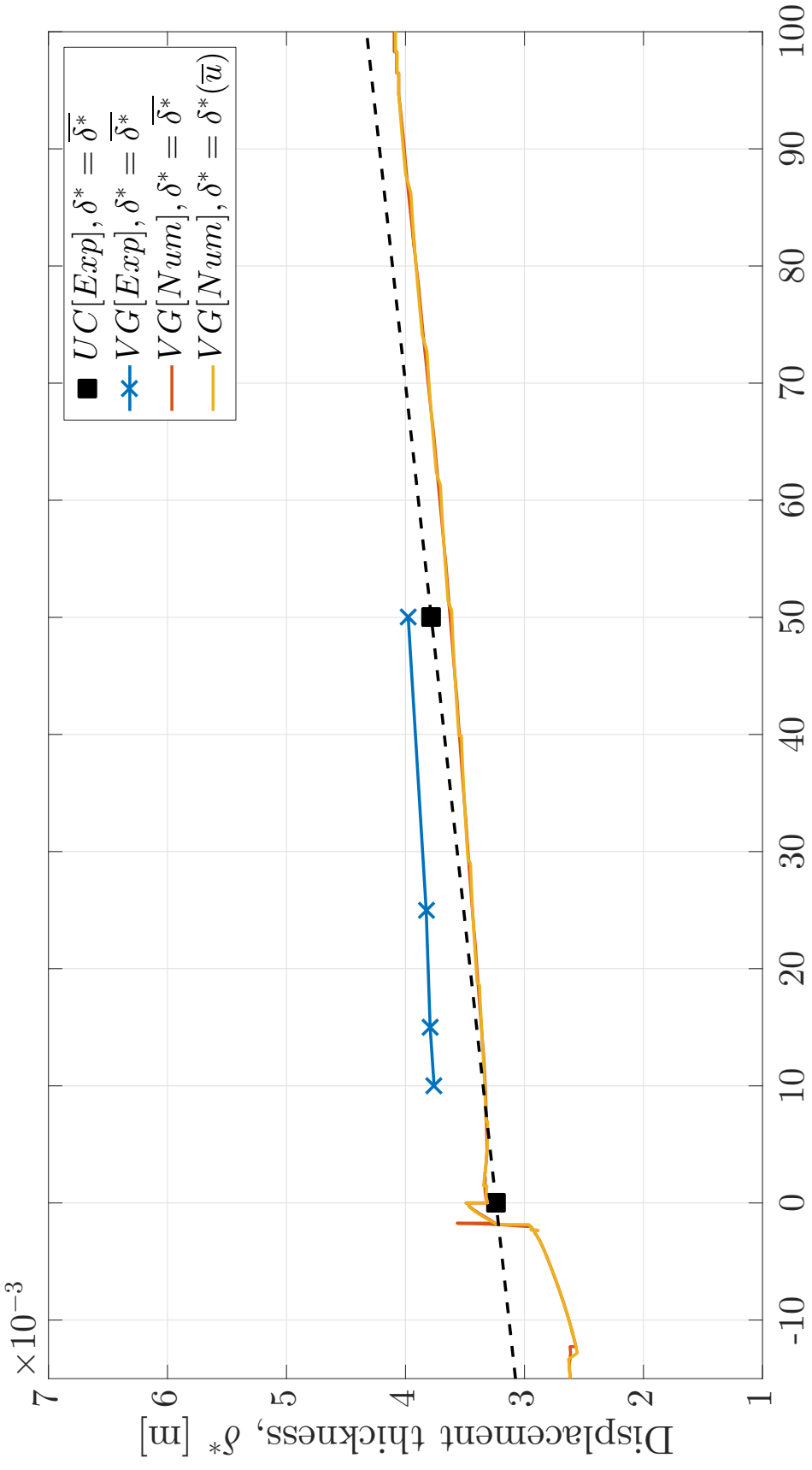

Figure 4.6: *Spanwise averaged displacement thickness, δ^* [m] development in streamwise direction for uncontrolled (UC) case and vortex generator (VG) case from experimental (Exp) and numerical (Num) dataset. For UC case from Exp dataset : Spanwise averaged ($z/D = \overline{z}$), for VG case from Exp dataset : ($z/D = 0, 0.208, 0.333, 0.5$) and for VG case from Num dataset : ($z/D = 0, 0.208, 0.333, 0.487$). Streamwise distance, x is dimensionalised by VG trailing edge location, x_{vg} and VG height, h.*

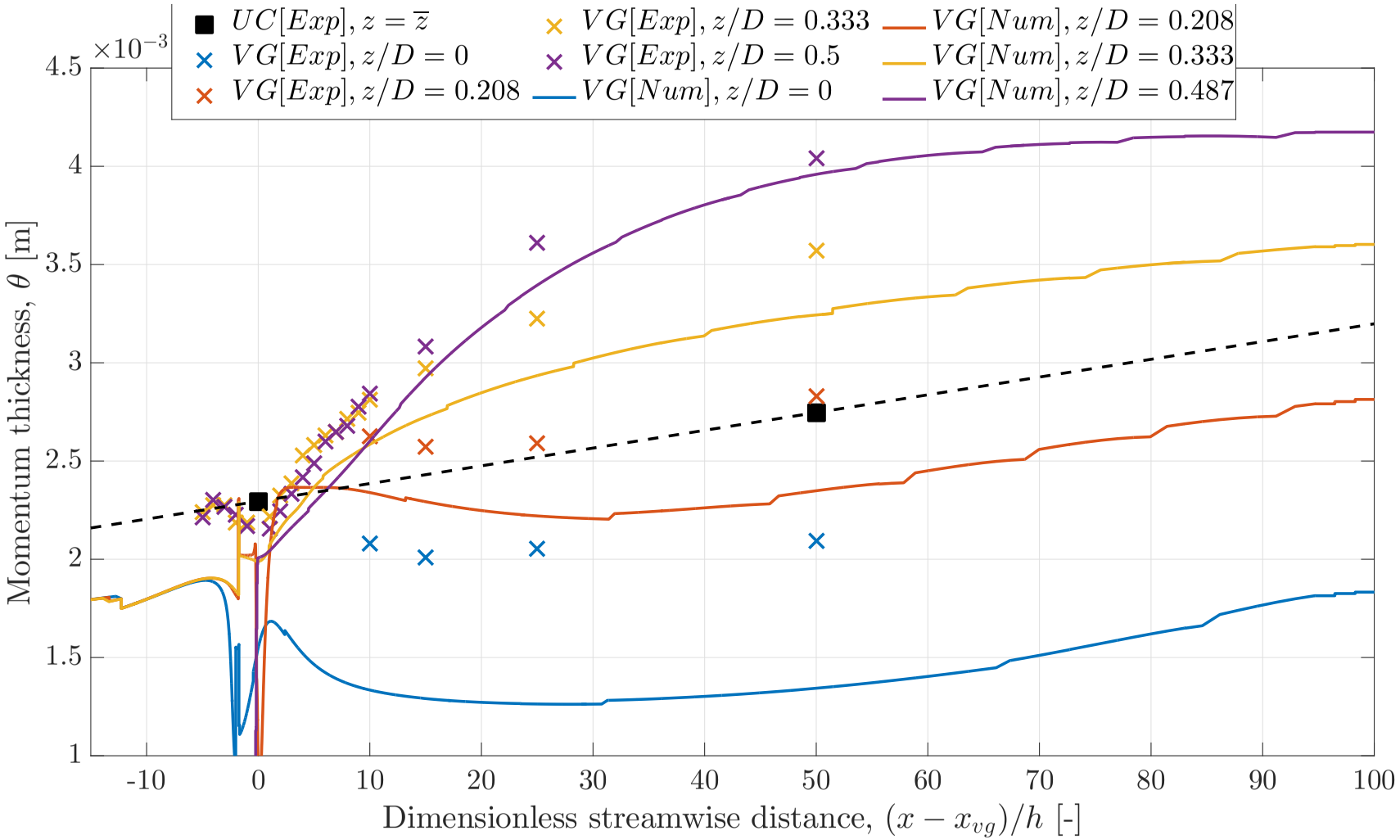

Figure 4.7: *Momentum thickness, θ [m] development in streamwise direction for uncontrolled (UC) case and vortex generator (VG) case from experimental (Exp) and numerical (Num) dataset. For UC case from Exp dataset : Spanwise averaged ($z/D = \overline{z}$), for VG case from Exp dataset : ($z/D = 0, 0.208, 0.333, 0.5$) and for VG case from Num dataset : ($z/D = 0, 0.208, 0.333, 0.487$). Streamwise distance, x is dimensionalised by VG trailing edge location, x_{vg} and VG height, h.*

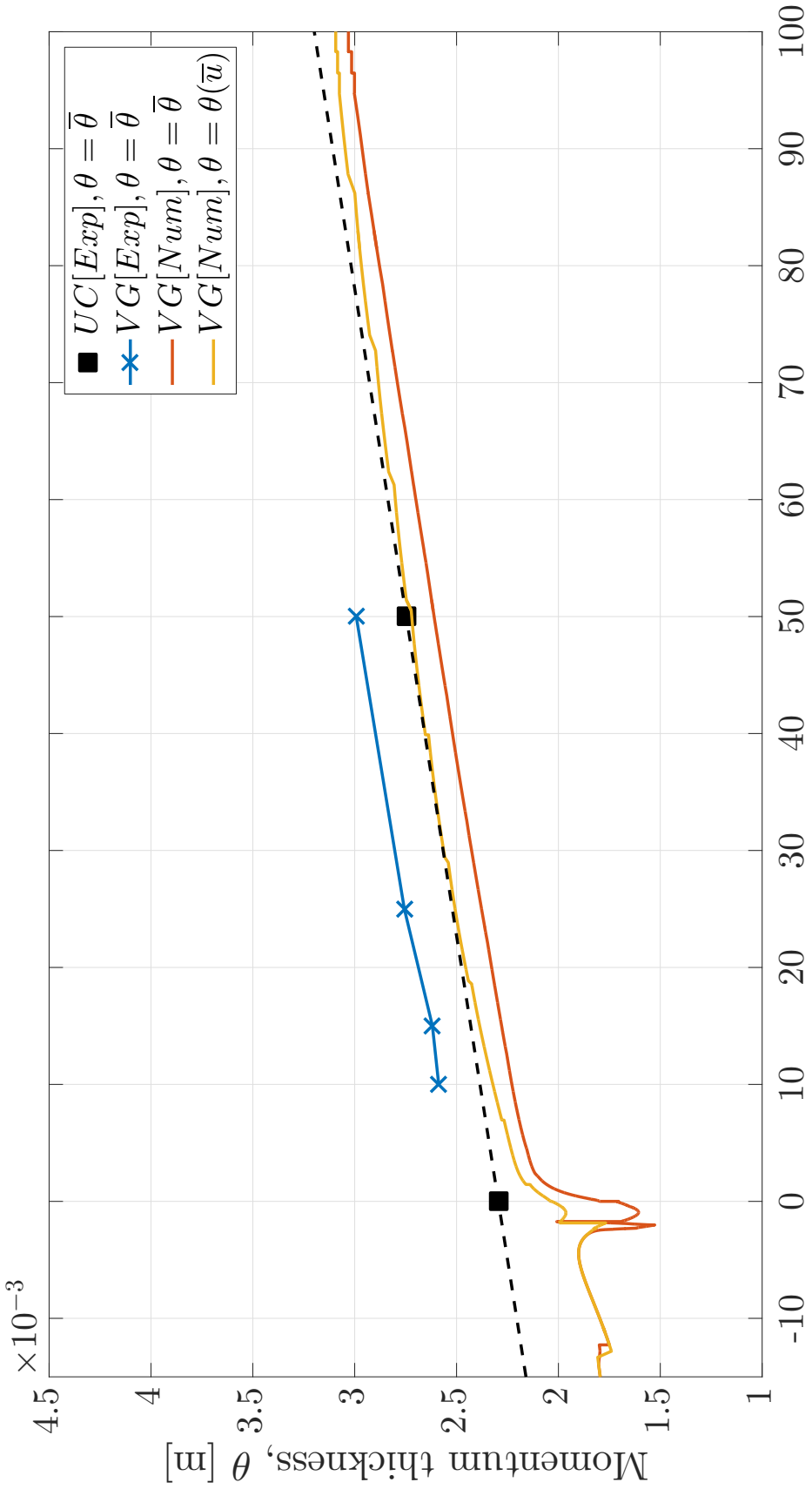

Figure 4.8: *Spanwise averaged momentum thickness, θ [m] development in streamwise direction for uncontrolled (UC) case and vortex generator (VG) case from experimental (Exp) and numerical (Num) dataset. For UC case from Exp dataset : Spanwise averaged $(z/D = \overline{z})$, for VG case from Exp dataset : $(z/D = 0, 0.208, 0.333, 0.5)$ and for VG case from Num dataset : $(z/D = 0, 0.208, 0.333, 0.487)$. Streamwise distance, x is dimensionalised by VG trailing edge location, x_{vg} and VG height, h.*

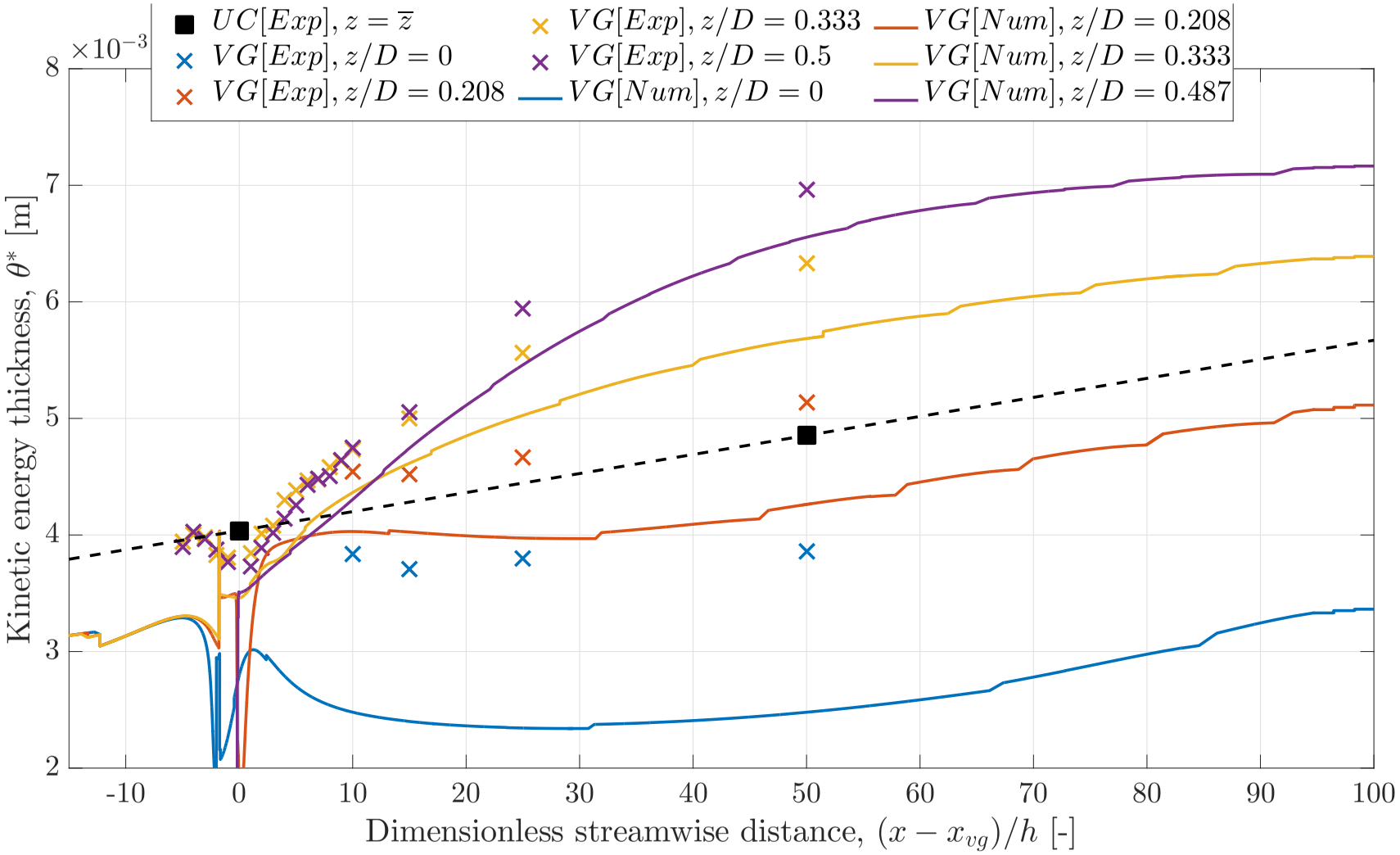

Figure 4.9: *Kinetic energy thickness, θ^* [m] development in streamwise direction for uncontrolled (UC) case and vortex generator (VG) case from experimental (Exp) and numerical (Num) dataset. For UC case from Exp dataset : Spanwise averaged ($z/D = \overline{z}$), for VG case from Exp dataset : ($z/D = 0, 0.208, 0.333, 0.5$) and for VG case from Num dataset : ($z/D = 0, 0.208, 0.333, 0.487$). Streamwise distance, x is dimensionalised by VG trailing edge location, x_{vg} and VG height, h.*

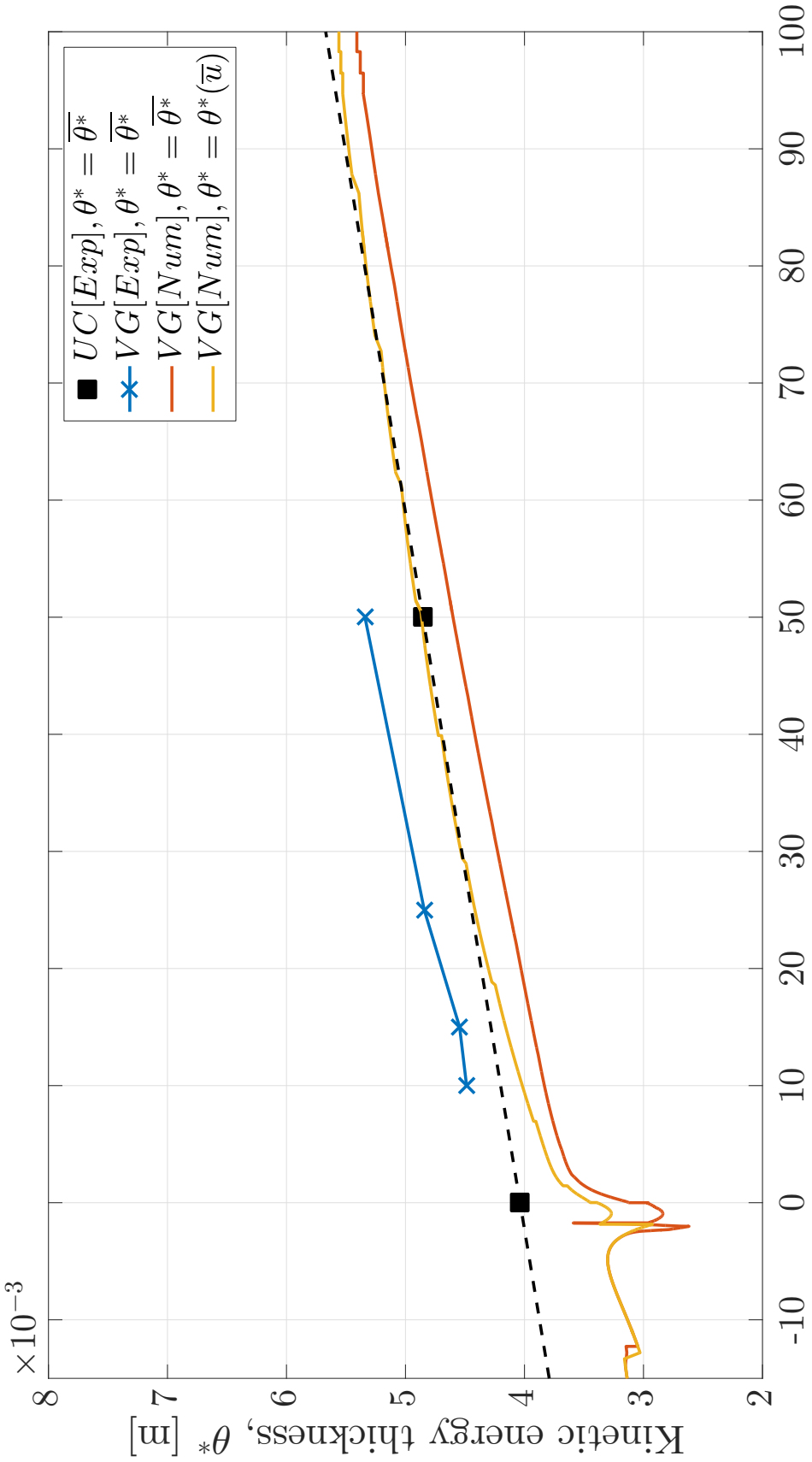

Figure 4.10: *Spanwise averaged kinetic energy thickness, θ^* [m] development in streamwise direction for uncontrolled (UC) case and vortex generator (VG) case from experimental (Exp) and numerical (Num) dataset. For UC case from Exp dataset : Spanwise averaged ($z/D = \overline{z}$), for VG case from Exp dataset : ($z/D = 0, 0.208, 0.333, 0.5$) and for VG case from Num dataset : ($z/D = 0, 0.208, 0.333, 0.487$). Streamwise distance, x is dimensionalised by VG trailing edge location, x_{vg} and VG height, h.*

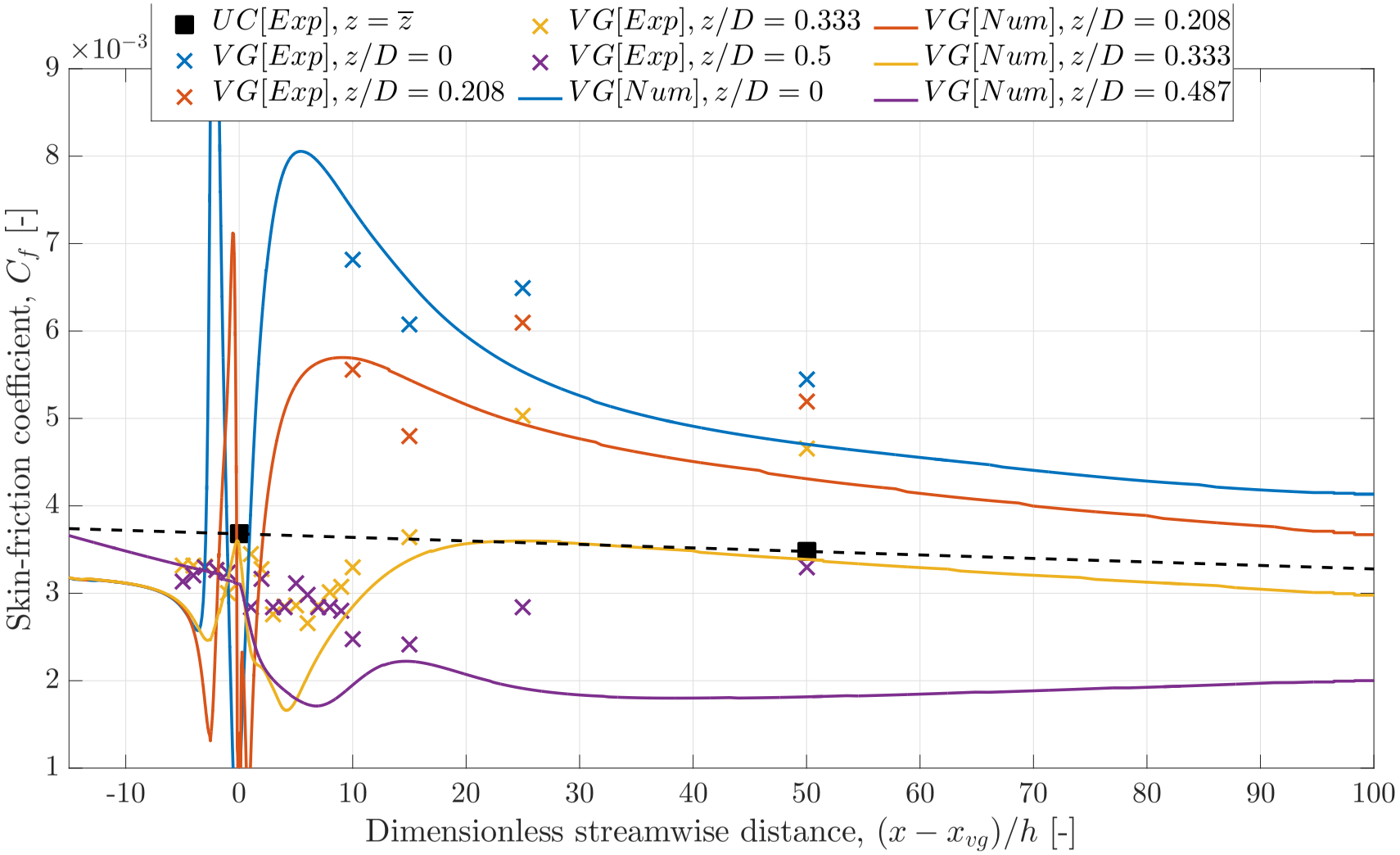

Figure 4.11: *Skin-friction coefficient, C_f [-] development in streamwise direction for uncontrolled (UC) case and vortex generator (VG) case from experimental (Exp) and numerical (Num) dataset. For UC case from Exp dataset : Spanwise averaged ($z/D = \overline{z}$), for VG case from Exp dataset : ($z/D = 0, 0.208, 0.333, 0.5$) and for VG case from Num dataset : ($z/D = 0, 0.208, 0.333, 0.487$). Streamwise distance, x is dimensionalised by VG trailing edge location, x_{vg} and VG height, h.*

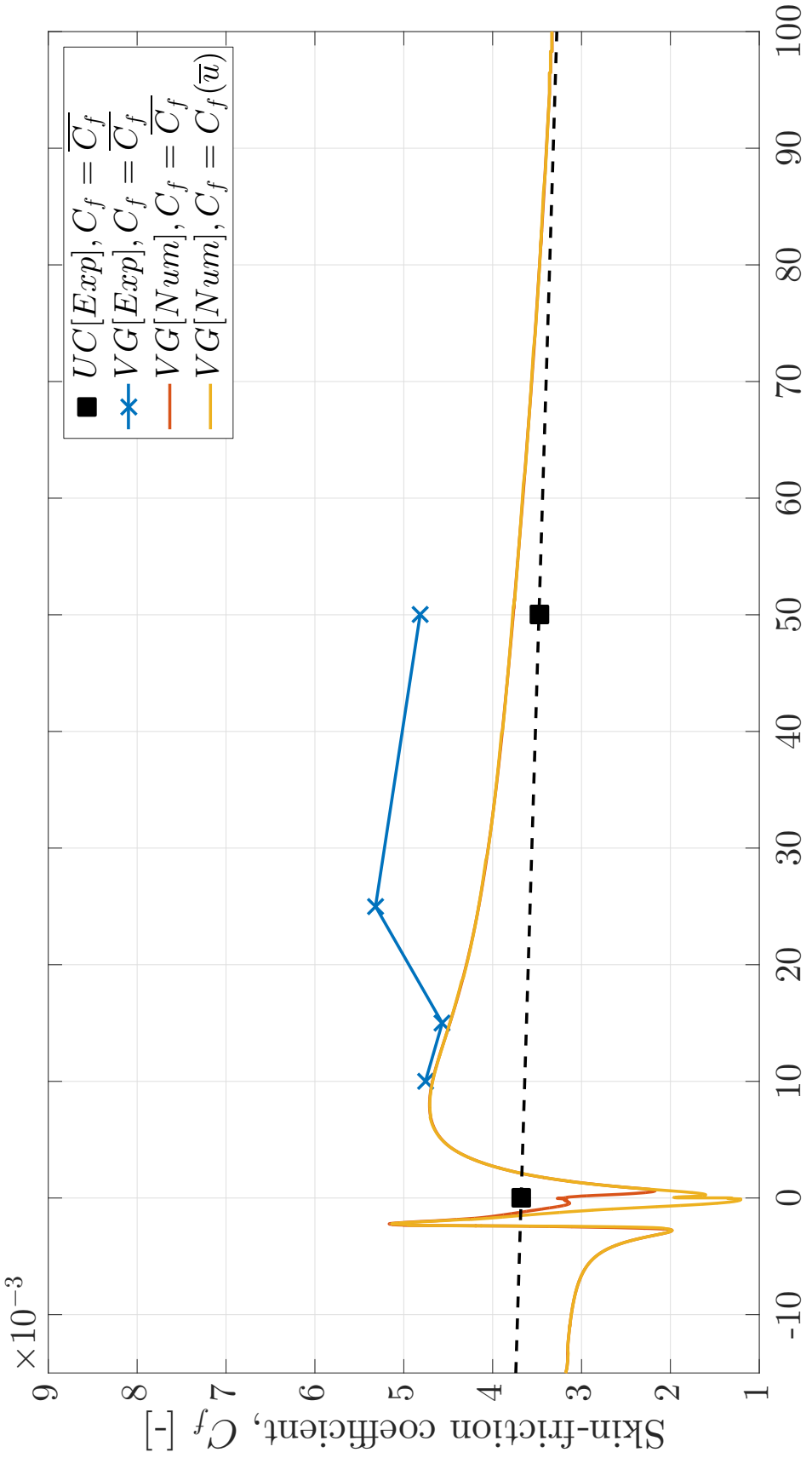

Figure 4.12: *Spanwise averaged skin-friction coefficient, C_f [-] development in streamwise direction for uncontrolled (UC) case and vortex generator (VG) case from experimental (Exp) and numerical (Num) dataset. For UC case from Exp dataset : Spanwise averaged ($z/D = \overline{z}$), for VG case from Exp dataset : ($z/D = 0, 0.208, 0.333, 0.5$) and for VG case from Num dataset : ($z/D = 0, 0.208, 0.333, 0.487$). Streamwise distance, x is dimensionalised by VG trailing edge location, x_{vg} and VG height, h.*

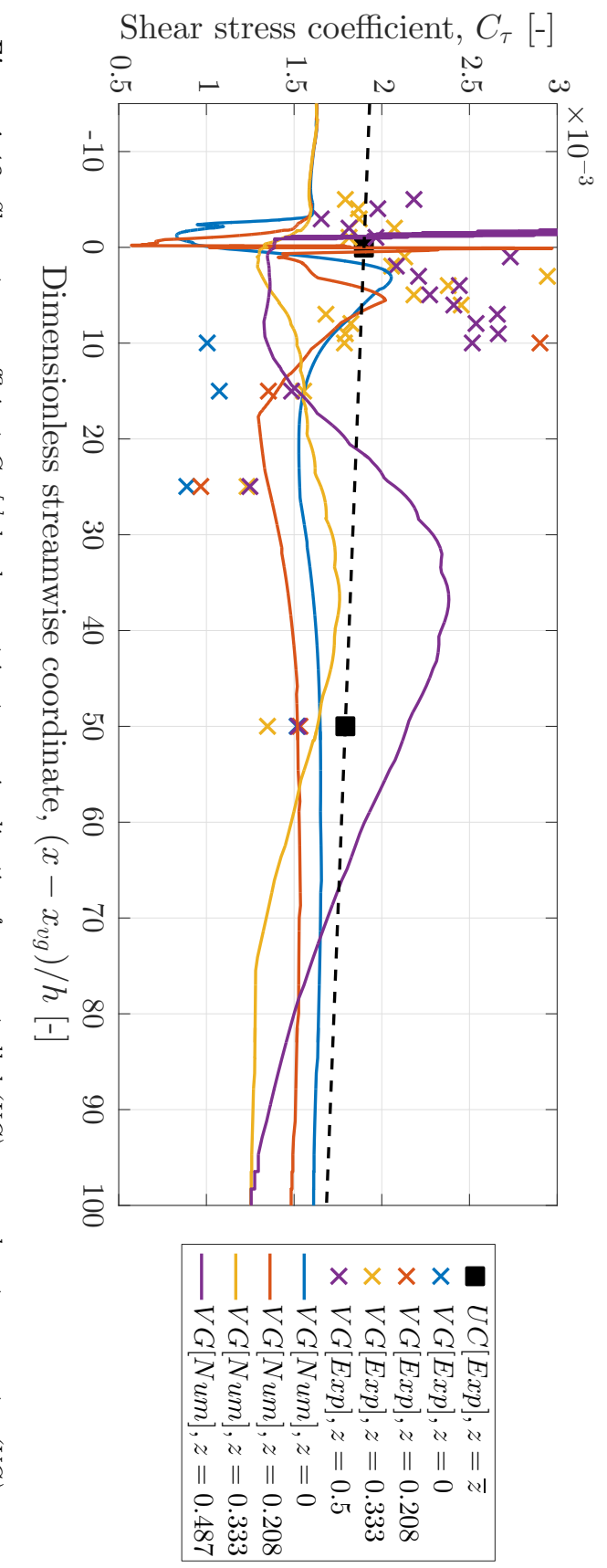

Figure 4.13: *Shear stress coefficient, C_τ [-] development in streamwise direction for uncontrolled (UC) case and vortex generator (VG) case from experimental (Exp) and numerical (Num) dataset. For UC case from Exp dataset : Spanwise averaged ($z/D = \overline{z}$), for VG case from Exp dataset : $(z/D = 0, 0.208, 0.333, 0.5)$ and for VG case from Num dataset : $(z/D = 0, 0.208, 0.333, 0.487)$. Streamwise distance, x is dimensionalised by VG trailing edge location, x_{vg} and VG height, h.*

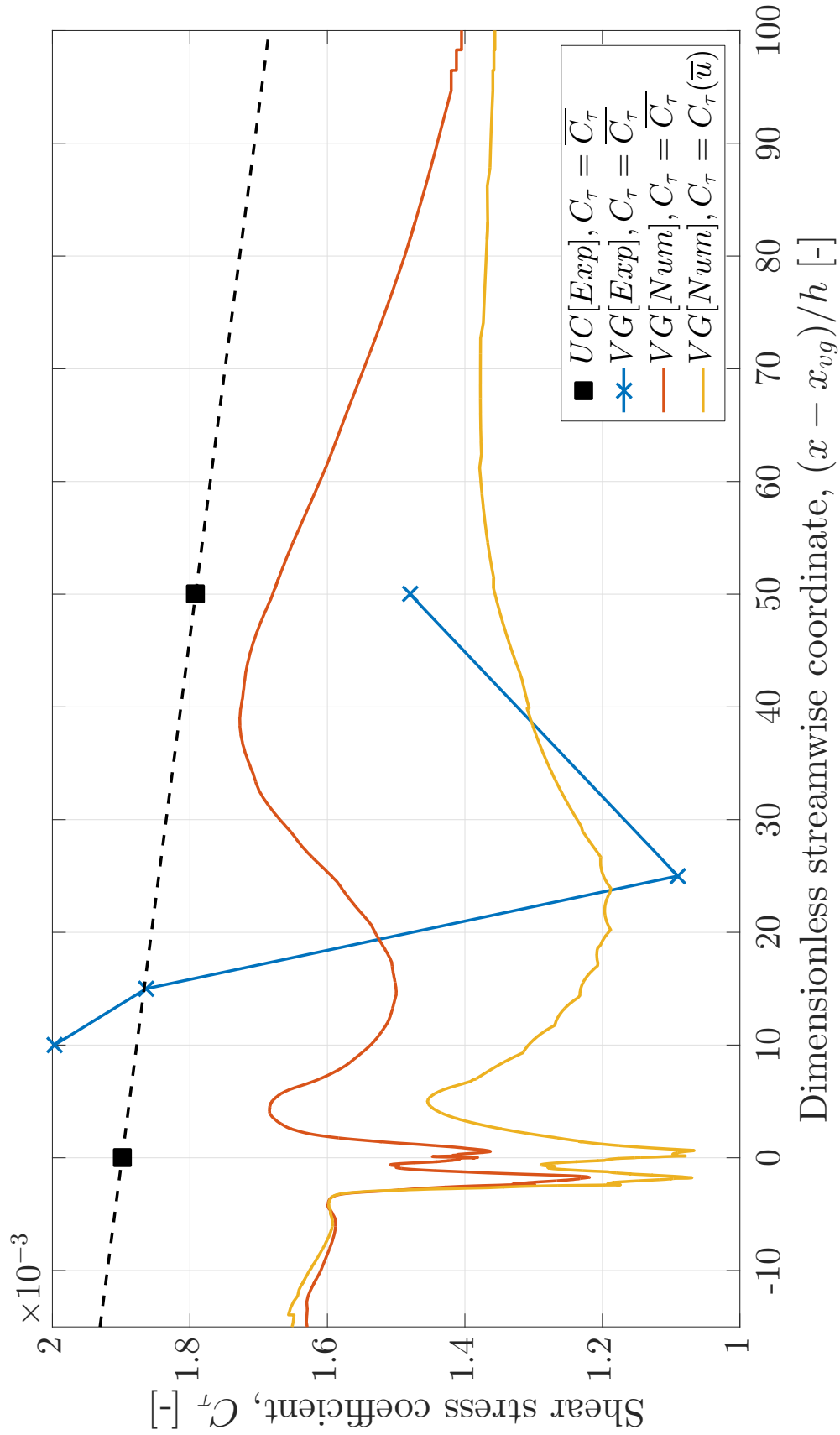

Figure 4.14: *Spanwise averaged shear stress coefficient, C_τ [-] development in streamwise direction for uncontrolled (UC) case and vortex generator (VG) case from experimental (Exp) and numerical (Num) dataset. For UC case from Exp dataset : Spanwise averaged $(z/D = \overline{z})$, for VG case from Exp dataset : $(z/D = 0, 0.208, 0.333, 0.5)$ and for VG case from Num dataset : $(z/D = 0, 0.208, 0.333, 0.487)$. Streamwise distance, x is dimensionalised by VG trailing edge location, x_{vg} and VG height, h.*

Figure 4.15: *Effective slip velocity, U_s [-] development in streamwise direction for uncontrolled (UC) case and vortex generator (VG) case from experimental (Exp) and numerical (Num) dataset. For UC case from Exp dataset : Spanwise averaged ($z/D = \overline{z}$), for VG case from Exp dataset : ($z/D = 0, 0.208, 0.333, 0.5$) and for VG case from Num dataset : ($z/D = 0, 0.208, 0.333, 0.487$). Streamwise distance, x is dimensionalised by VG trailing edge location, x_{vg} and VG height, h.*

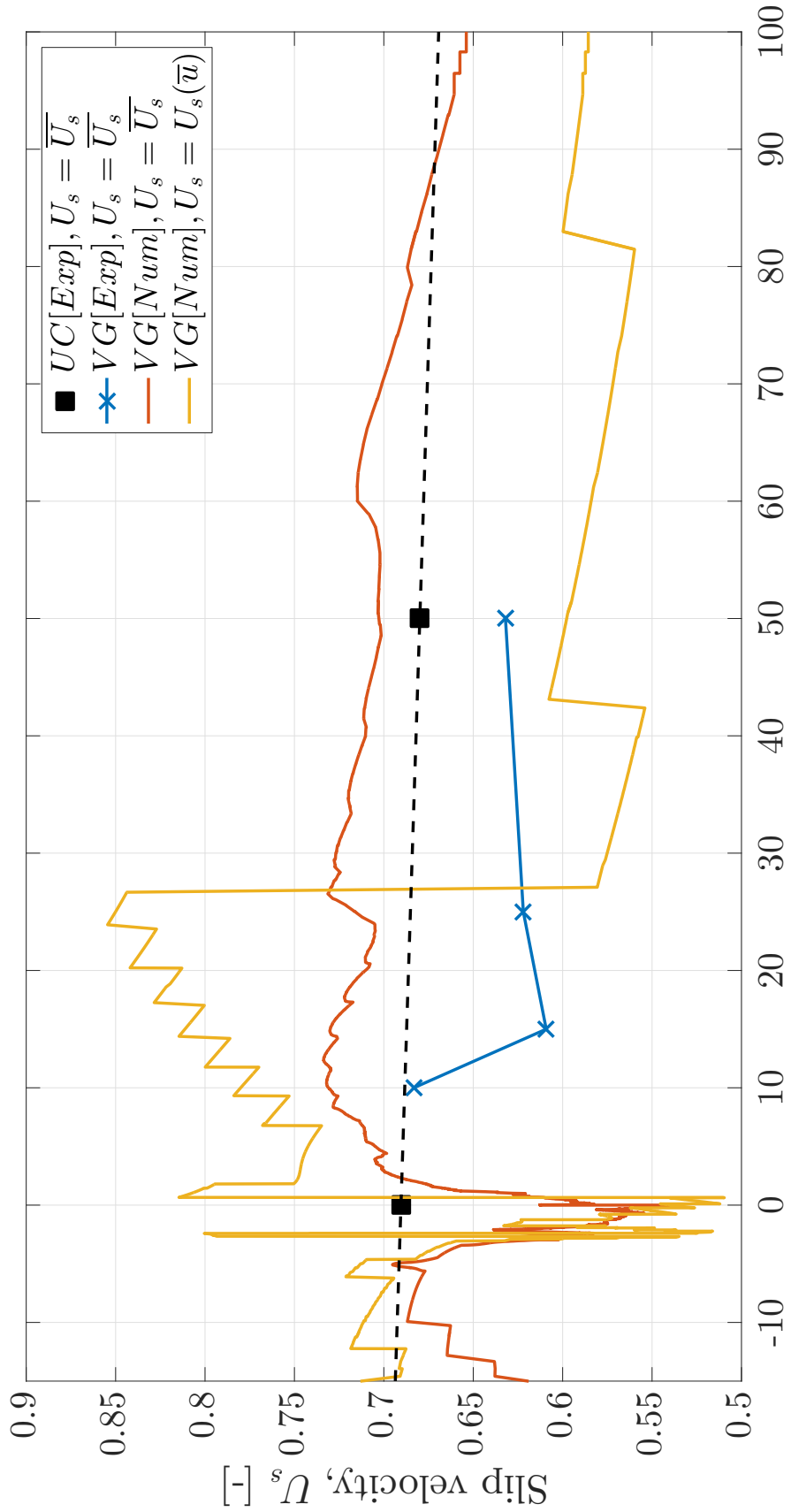

Figure 4.16: *Spanwise averaged effective slip velocity, U_s [-] development in streamwise direction for uncontrolled (UC) case and vortex generator (VG) case from experimental (Exp) and numerical (Num) dataset. For UC case from Exp dataset : Spanwise averaged ($z/D = \overline{z}$), for VG case from Exp dataset : ($z/D = 0, 0.208, 0.333, 0.5$) and for VG case from Num dataset : ($z/D = 0, 0.208, 0.333, 0.487$). Streamwise distance, x is dimensionalised by VG trailing edge location, x_{vg} and VG height, h.*

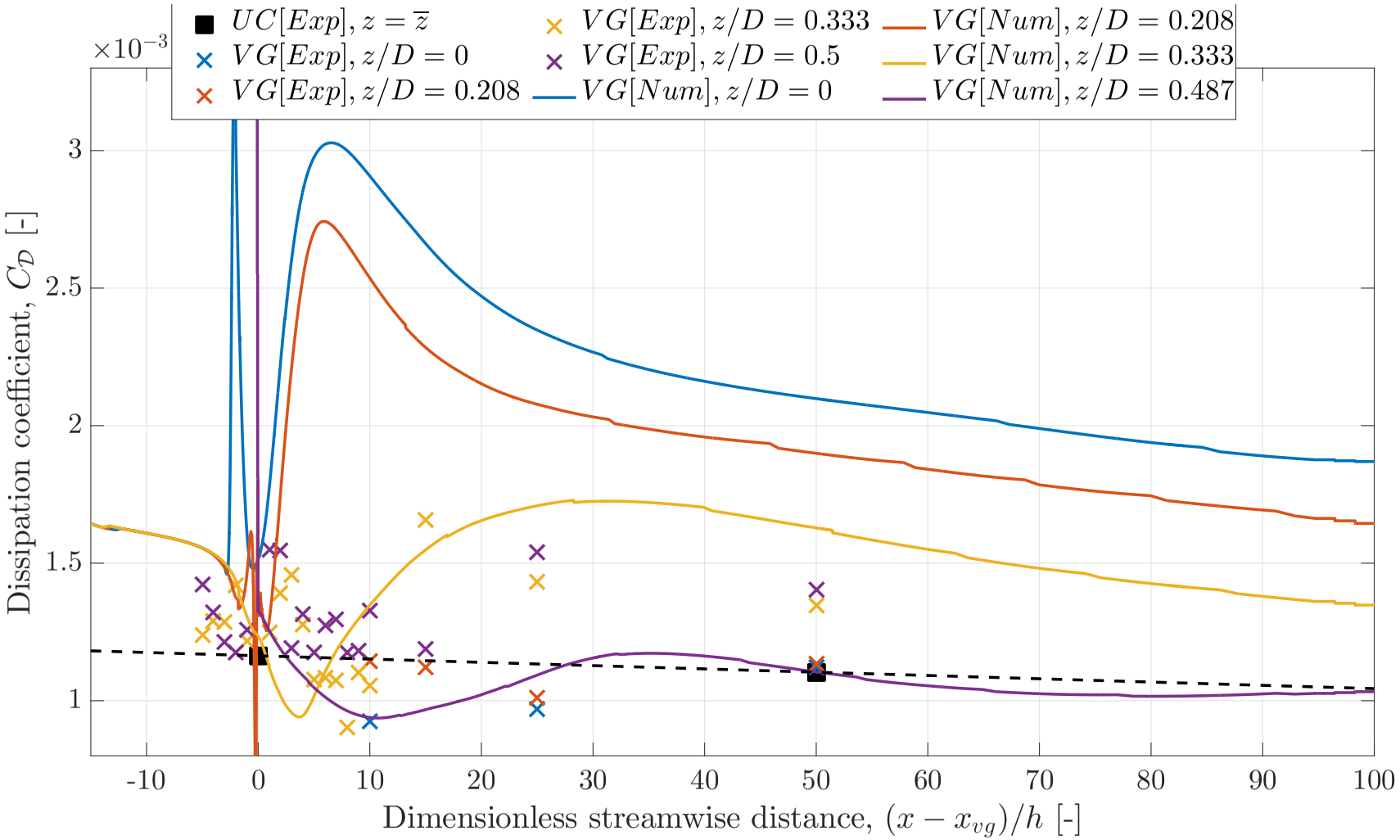

Figure 4.17: *Dissipation coefficient, $C_{\mathcal{D}}$ [-] development in streamwise direction for uncontrolled (UC) case and vortex generator (VG) case from experimental (Exp) and numerical (Num) dataset. For UC case from Exp dataset : Spanwise averaged ($z/D = \overline{z}$), for VG case from Exp dataset : ($z/D = 0, 0.208, 0.333, 0.5$) and for VG case from Num dataset : ($z/D = 0, 0.208, 0.333, 0.487$). Streamwise distance, x is dimensionalised by VG trailing edge location, x_{vg} and VG height, h.*

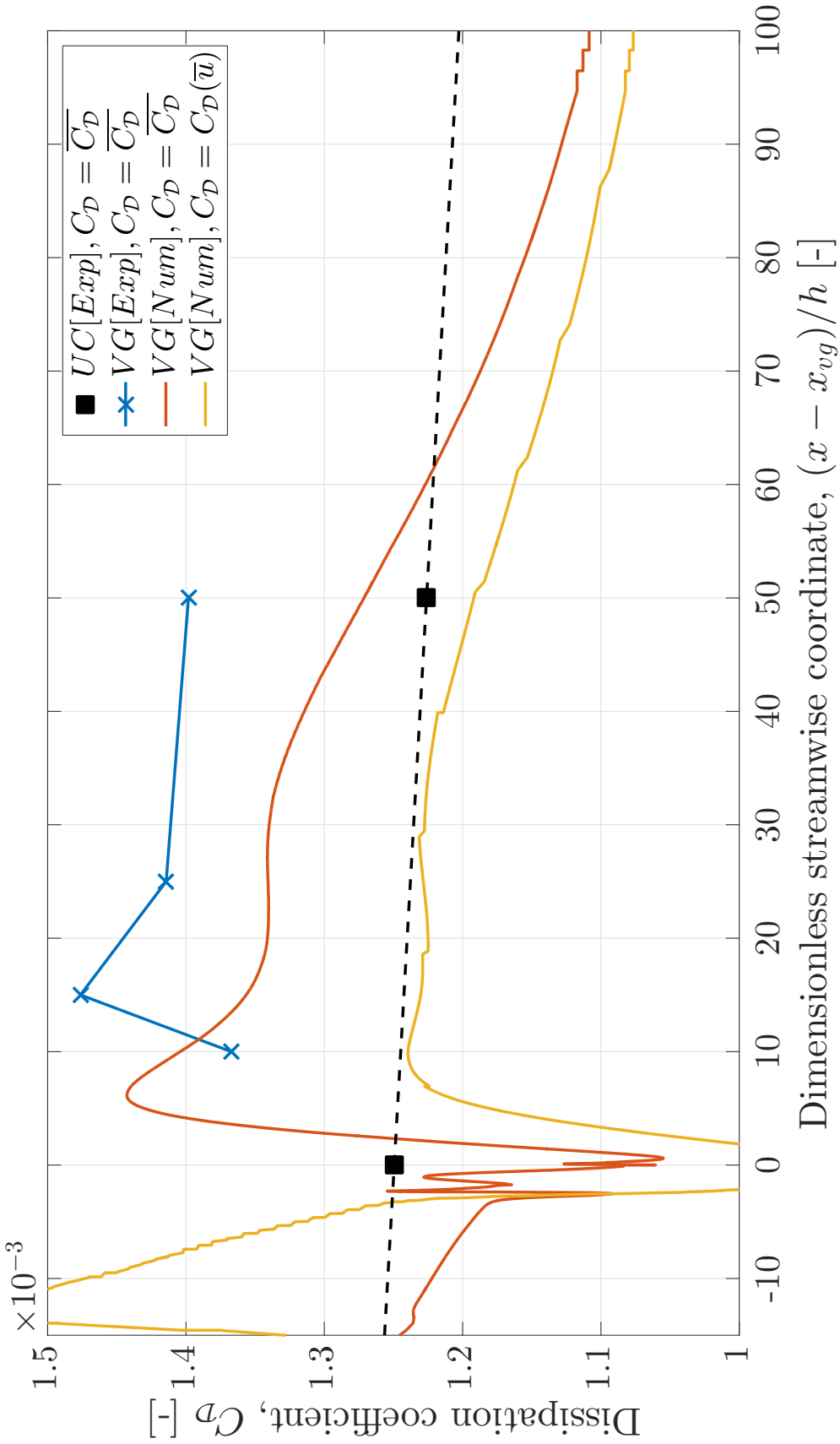

Figure 4.18: *Spanwise averaged dissipation coefficient, $C_{\mathcal{D}}$ [-] development in streamwise direction for uncontrolled (UC) case and vortex generator (VG) case from experimental (Exp) and numerical (Num) dataset. For UC case from Exp dataset : Spanwise averaged $(z/D = \overline{z})$, for VG case from Exp dataset : $(z/D = 0, 0.208, 0.333, 0.5)$ and for VG case from Num dataset : $(z/D = 0, 0.208, 0.333, 0.487)$. Streamwise distance, x is dimensionalised by VG trailing edge location, x_{vg} and VG height, h.*

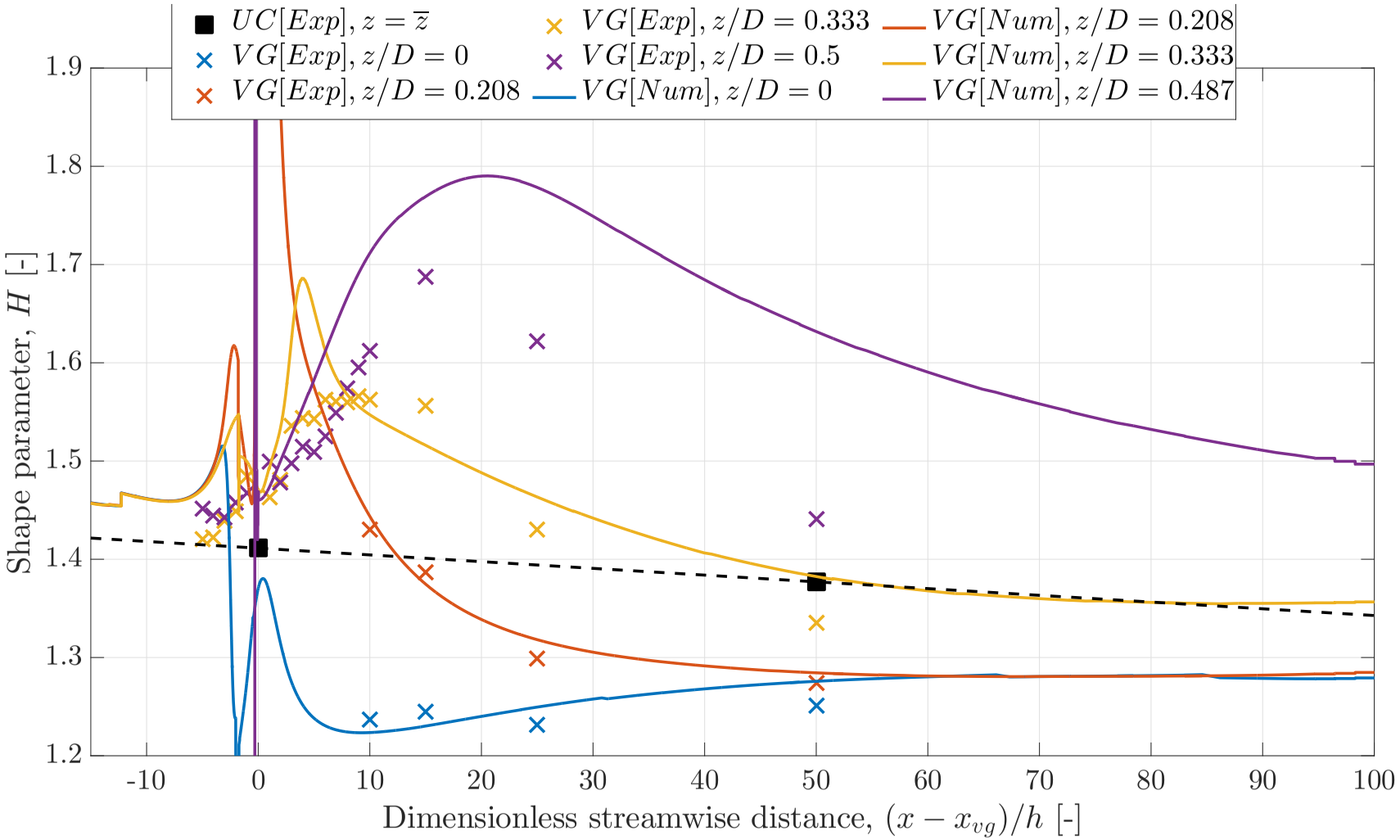

Figure 4.19: *Shape parameter, H [-] development in streamwise direction for uncontrolled (UC) case and vortex generator (VG) case from experimental (Exp) and numerical (Num) dataset. For UC case from Exp dataset : Spanwise averaged ($z/D = \overline{z}$), for VG case from Exp dataset : ($z/D = 0, 0.208, 0.333, 0.5$) and for VG case from Num dataset : ($z/D = 0, 0.208, 0.333, 0.487$). Streamwise distance, x is dimensionalised by VG trailing edge location, x_{vg} and VG height, h.*

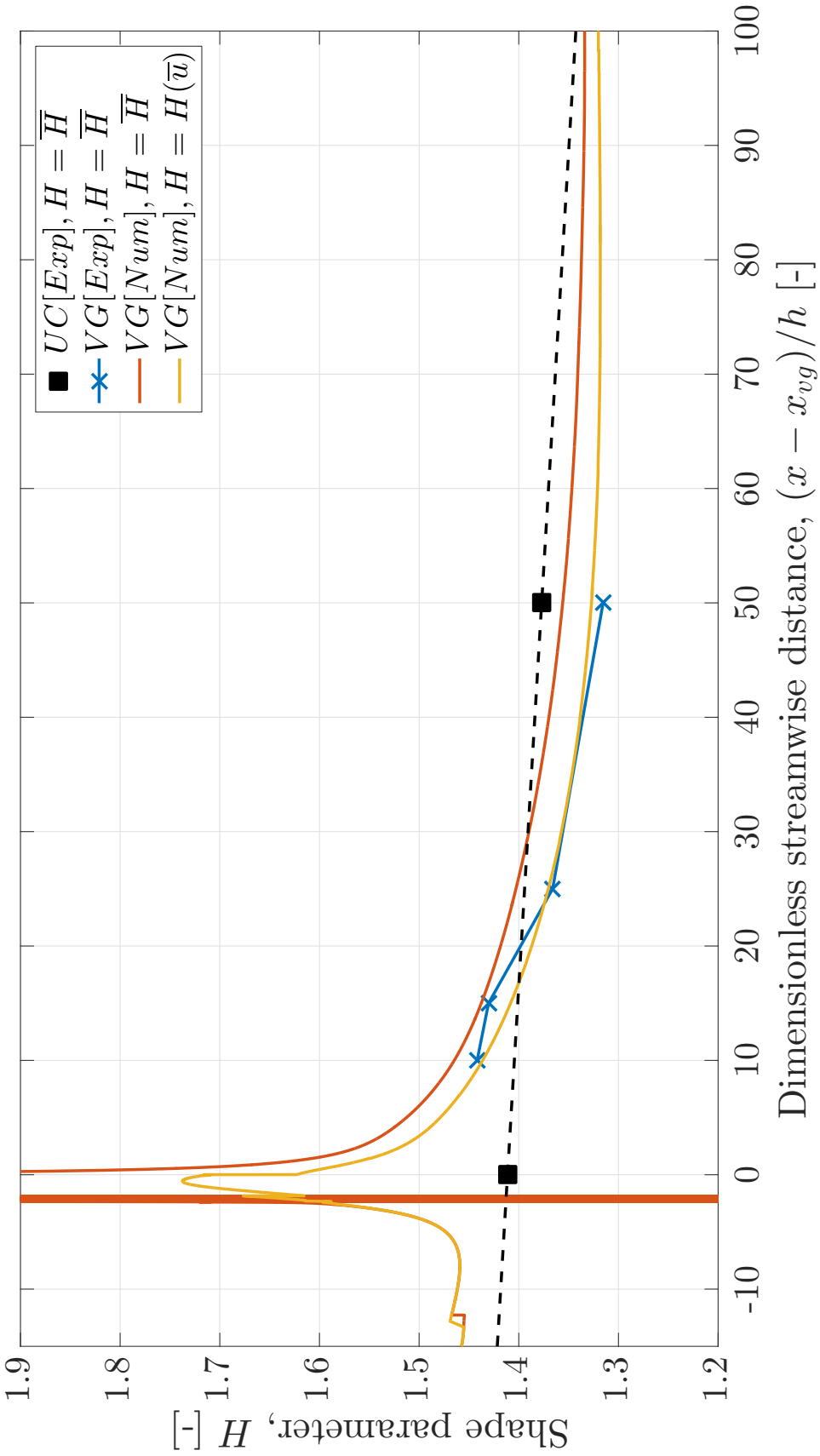

Figure 4.20: *Spanwise averaged shape parameter, H [-] development in streamwise direction for uncontrolled (UC) case and vortex generator (VG) case from experimental (Exp) and numerical (Num) dataset. For UC case from Exp dataset : Spanwise averaged $(z/D = \overline{z})$, for VG case from Exp dataset : $(z/D = 0, 0.208, 0.333, 0.5)$ and for VG case from Num dataset : $(z/D = 0, 0.208, 0.333, 0.487)$. Streamwise distance, x is dimensionalised by VG trailing edge location, x_{vg} and VG height, h.*

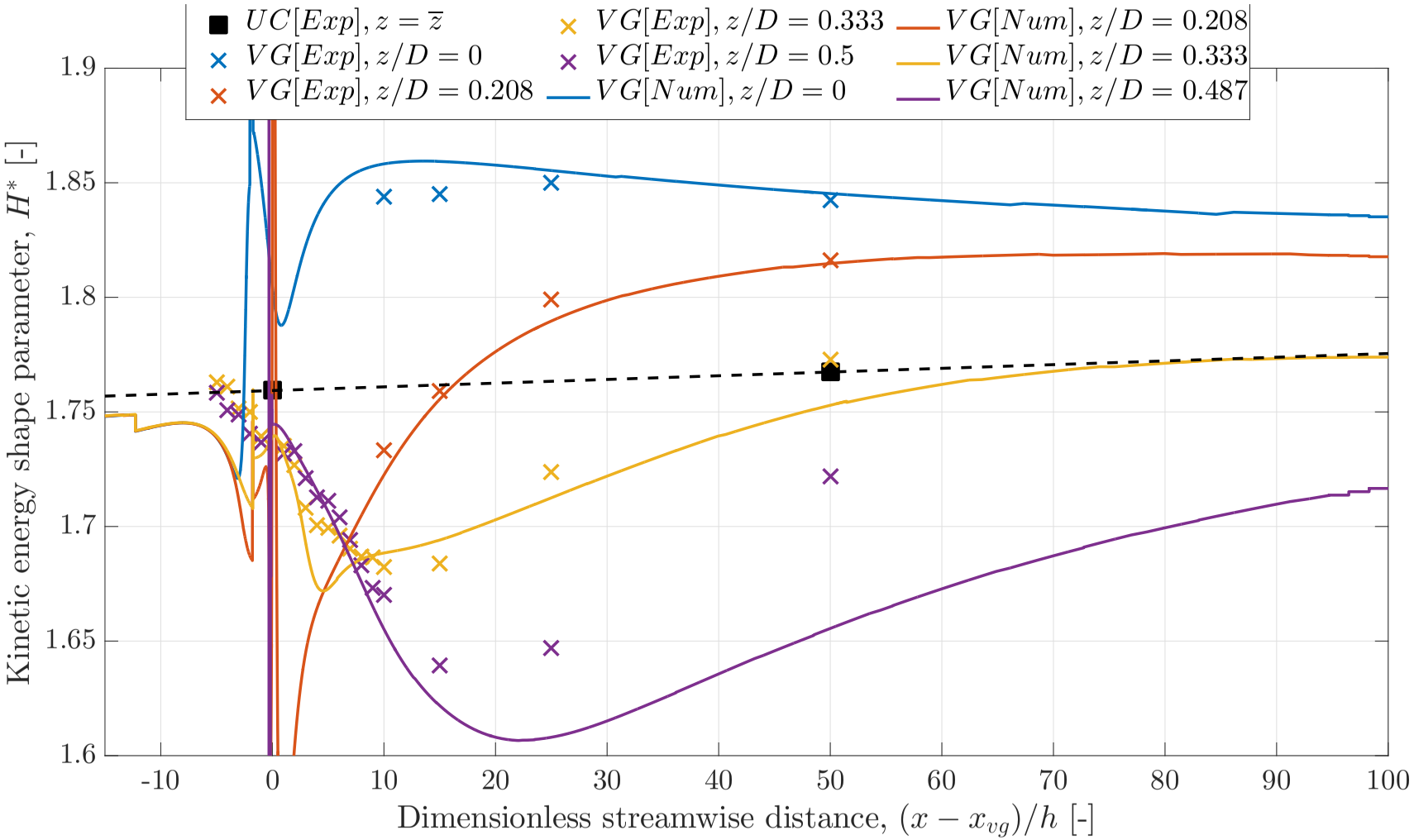

Figure 4.21: *Kinetic energy shape parameter, H^* [-] development in streamwise direction for uncontrolled (UC) case and vortex generator (VG) case from experimental (Exp) and numerical (Num) dataset. For UC case from Exp dataset : Spanwise averaged ($z/D = \overline{z}$), for VG case from Exp dataset : ($z/D = 0, 0.208, 0.333, 0.5$) and for VG case from Num dataset : ($z/D = 0, 0.208, 0.333, 0.487$). Streamwise distance, x is dimensionalised by VG trailing edge location, x_{vg} and VG height, h.*

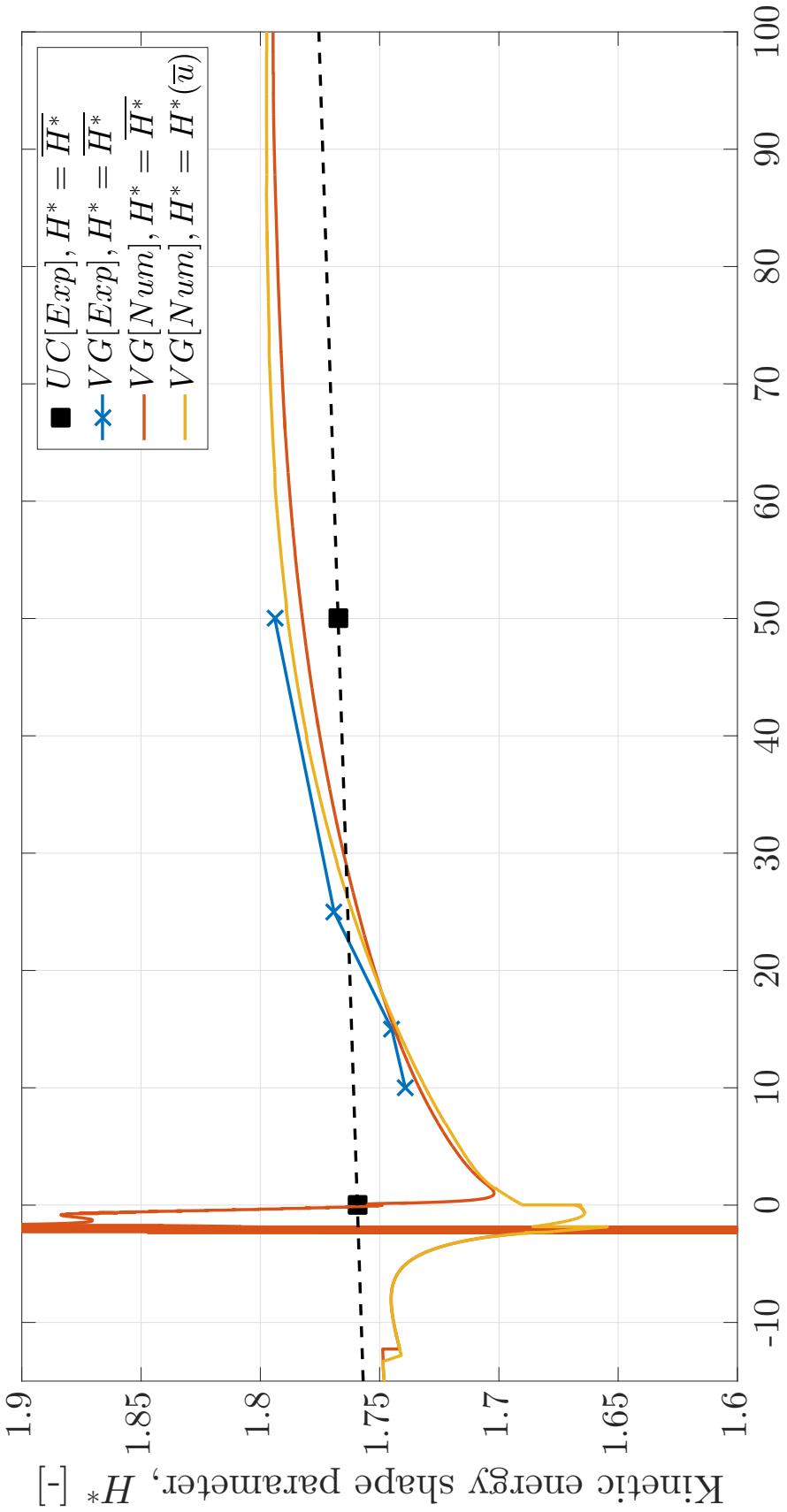

Figure 4.22: *Spanwise averaged kinetic energy shape parameter, H^* [-] development in streamwise direction for uncontrolled (UC) case and vortex generator (VG) case from experimental (Exp) and numerical (Num) dataset. For UC case from Exp dataset : Spanwise averaged $(z/D = \overline{z})$, for VG case from Exp dataset : $(z/D = 0, 0.208, 0.333, 0.5)$ and for VG case from Num dataset : $(z/D = 0, 0.208, 0.333, 0.487)$. Streamwise distance, x is dimensionalised by VG trailing edge location, x_{vg} and VG height, h.*

Chapter 5

Testing integral boundary layer relations for vortex generator induced flow using numerical dataset

Step 5 and **Step 6** of the approach (see 3.6) are discussed in this chapter. Integral boundary layer relations, namely van Kármán integral momentum relation (see equation 3.1) and kinetic energy shape parameter relation(see equation 3.11) are tested for vortex generator induced flow (VGIF) using numerical dataset. Terminology exclusive to this chapter is introduced in section 5.1. Uncertainty in testing the relations are discussed in section 5.2. Skin-friction coefficient, C_f and dissipation coefficient, $C_{\mathcal{D}}$ using different methods are compared and discussed in 5.3.

5.1 Chapter Terminology

Chapter exclusive terminology is introduced in this section. All the analysis are done using vortex generator case from the numerical dataset. This remove terminology of uncontrolled case, UC and experimental dataset, Exp. Integral parameters H^*, C_f, $C_{\mathcal{D}}$, U_s and C_τ can be determined directly from numerical dataset or through closure relations.

First new terms $C_f\left[\mathcal{R}\right]$ and $C_{\mathcal{D}}\left[\mathcal{R}\right]$ are introduced. These are C_f and $C_{\mathcal{D}}$ reminders van Kármán integral momentum relation (see equation 3.1) and kinetic energy shape parameter relation (see equation 3.11) respectively. For ease of understanding the equations are rearranged and reproduced as equations 5.1 and 5.2.

$$C_f\left[\mathcal{R}\right] = 2 \times \left[\frac{d\theta}{dx} + \left(H+2\right)\frac{\theta}{u_e}\frac{du_e}{dx}\right] \tag{5.1}$$

$$C_{\mathcal{D}}\left[\mathcal{R}\right] = 0.5 \times \left[\theta\frac{dH^*}{dx} + \left(H^*\left(1-H\right)\right)\frac{\theta}{u_e}\frac{du_e}{dx} + H^*\frac{C_f}{2}\right] \tag{5.2}$$

Notation	Method	Input parameter / Remark
Kinetic energy shape parameter [-]		
H^* [Num]	Numerical dataset	
H^* [DCR]	Drela's closure relation	H, Re_θ
Skin-friction coefficient [-]		
C_f [Num]	Numerical dataset	Gradient Method
C_f [SCR]	Swafford's closure relation	H, Re_θ
C_f [$\mathcal{R}$]	van karman	H, θ
Effective slip velocity [-]		
U_s [Num]	Numerical dataset	
U_s [DCR (H^* [])]	Drela's closure relation	H, H^* [Exp or DCR]
Shear stress coefficient [-]		
C_τ [Num]	Numerical dataset	
C_τ [DCR (H^* [], Us[])]	Drela's closure relation	H, H^* [Exp or DCR] U_s [Num] or U_s [DCR (H*[])]
Dissipation coefficient [-]		
$C_\mathcal{D}$ [Num]	Numerical dataset	
$C_\mathcal{D}$ [DCR (C_f [], Us [], C_τ [])]	Drela's closure relation	C_f [Num or SCR or R] U_s [Num] or U_s [DCR H^* []] C_τ [Num] or C_τ [DCR (H*[],Us[])]
$C_\mathcal{D}$ [$\mathcal{R}$ (H^* [], C_f [])]	Shape parameter equation	H, θ H^* [Exp or DCR] C_f [Num or SCR or R]

Table 5.1: *Terminology exclusive for chapter 5*

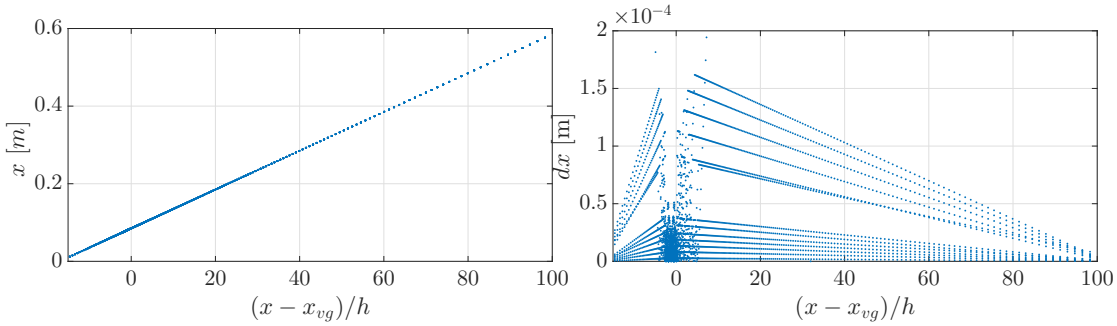

(a) Unique data points extracted from numerical data set is monotonously increasing.

(b) Central difference finite scheme implemented on streamwise distance.

Figure 5.1: *Error due to non-uniform grid spacing. $x, [m]$ is the streamwise distance in meters. $dx, [m]$ is the differential streamwise distance in meters. $(x - x_{vg})/h$ [-] is the dimensionless streamwise distance, where x_{vg} is location of trailing edge VG, and h is the VG height.*

5.2 Uncertainty in determining $C_f\,[\mathcal{R}]$ and $C_{\mathcal{D}}\,[\mathcal{R}]$

5.2.1 Error due to non-uniform grid spacing

Unique data points from numerical dataset are extracted using a MATLAB [33] code and has non-uniform grid spacing. The unique data points extracted are monotonously increasing in streamwise direction (see 5.1a). Fluctuations in differential streamwise distance, dx using a central difference finite scheme on unique data points is shown in figure 5.1b. Skin-friction coefficient and dissipation coefficient are in order of $1e-03$ hence, these fluctuations will have an impact in determining $C_f[\mathcal{R}]$ and $C_D[\mathcal{R}]$. For $C_f[\mathcal{R}]$ these fluctuations will be enlarged by factor of 2 (see 5.1) and $C_{\mathcal{R}}[\mathcal{R}]$ will be scaled down by factor of 2 (see 5.2). A linear interpolation is done to reduce the fluctuations due to non-uniform gird spacing. Interpolation is done considered with spacing between the non-uniform grid spacing. The unique points are concentrated on VGs and integral parameters are calculated correctly (see section) and hence, coarsely interpolated. The interpolated data points are plotted against the original unique data points in figures 5.2 and 5.3. Dissipation coefficient are smoother due to interpolation, however the skin-friction coefficient despite smoother, VG heights from 70 to 100 it does not follow a smooth trend, finely interpolating raises interpolation errors as it is also sparsely spaced further downstream. Nevertheless, the interpolated values are chosen.

5.2.2 Error due to boundary layer edge velocity detection method

As seen in 2.2.2 boundary layer edge velocity is discussed and the roughness is seen in section. Just to indicate if a smoother would have lead to improvement.C_f and $C_{\mathcal{D}}$ determined taking the maximum velocity (free stream velocity) are compared and plotted as figures 5.4 and 5.5. Nevertheless, boundary layer edge velocity is used for the rest of the thesis work.

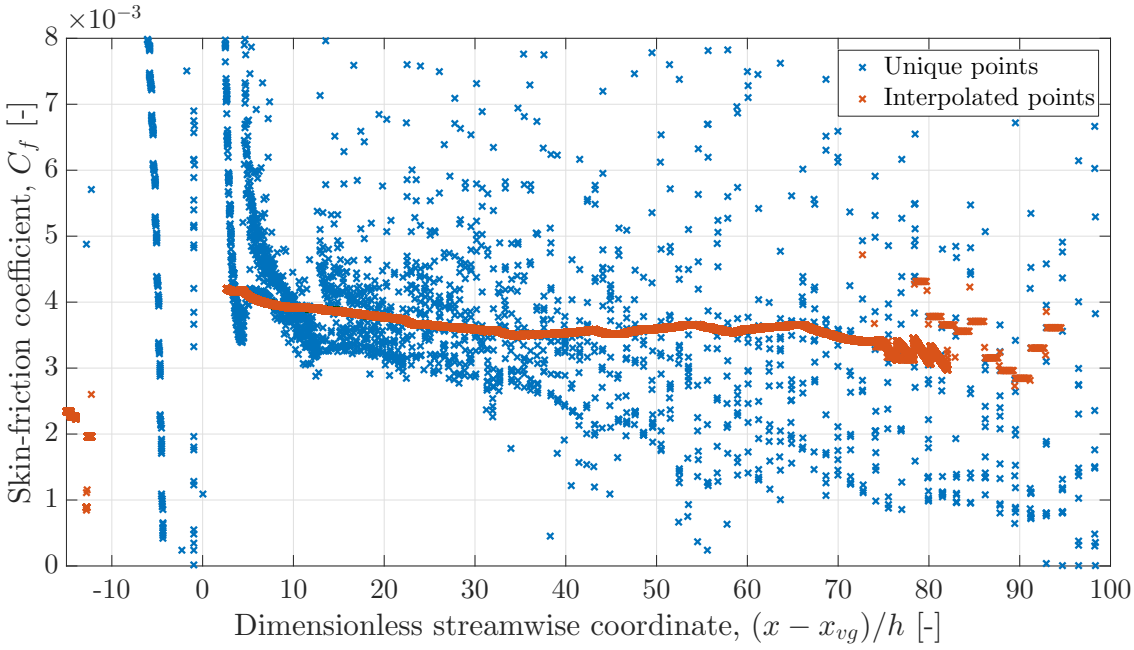

Figure 5.2: *Interpolated skin-friction coefficient downstream development against unique data points.*

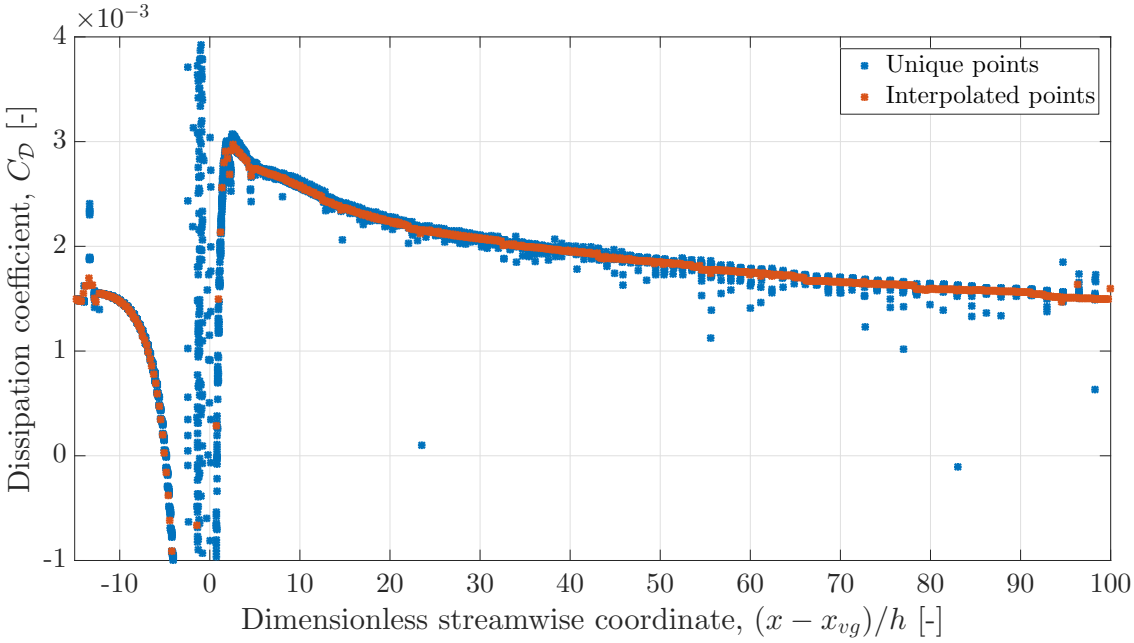

Figure 5.3: *Interpolated dissipation coefficient downstream development against unique data points.*

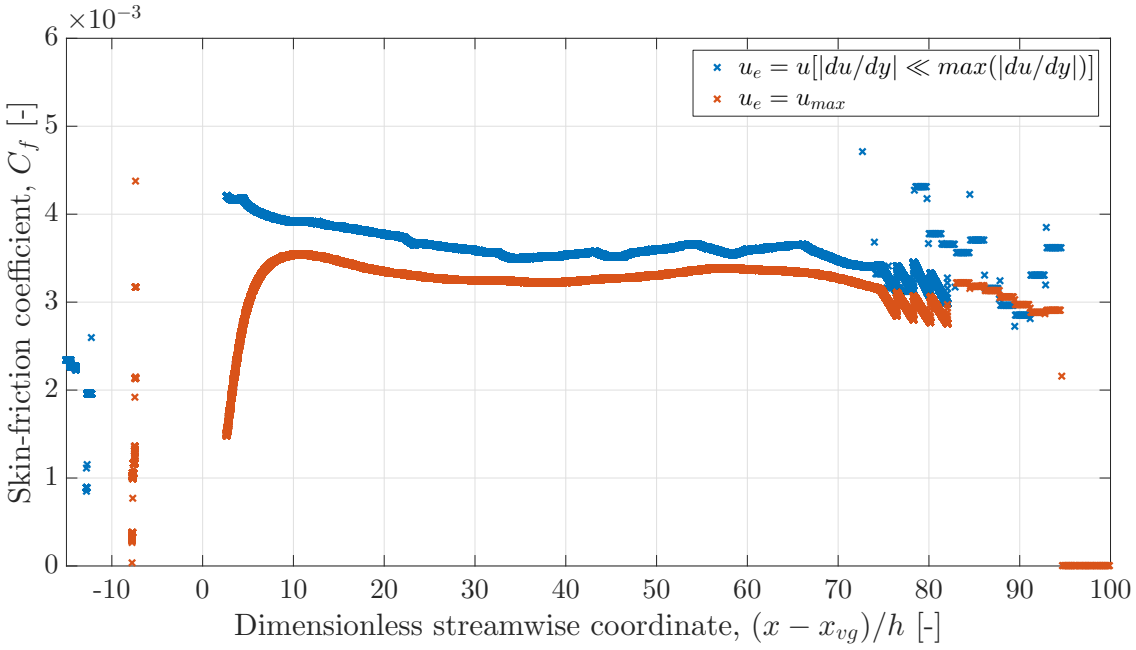

Figure 5.4: *Uncertainty in determining skin-friction coefficient due to boundary edge velocity detection method.*

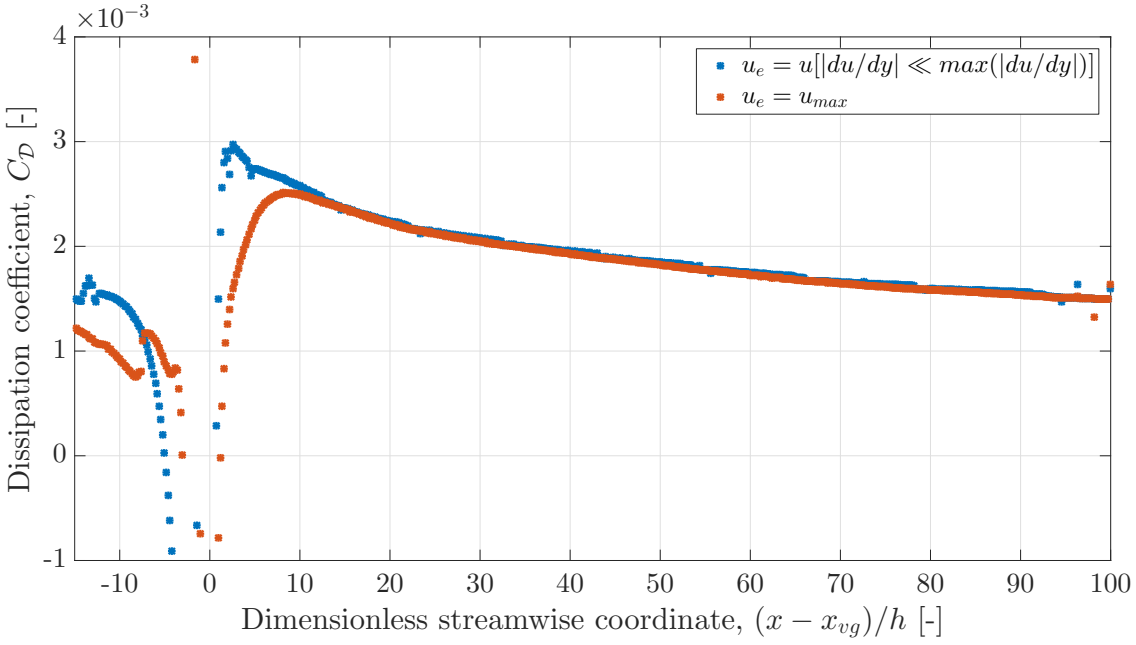

Figure 5.5: *Uncertainty in determining dissipation coefficient due to boundary edge velocity detection method.*

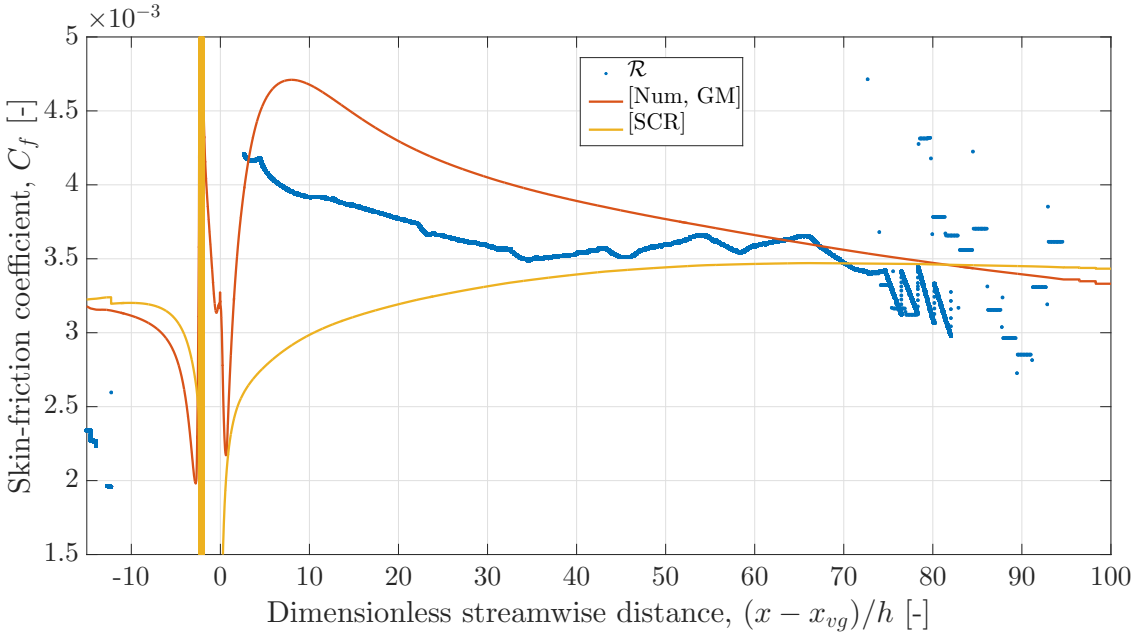

Figure 5.6: *Dissipation coefficient, $C_{\mathcal{D}}$ [-] development in streamwise direction. Streamwise distance, x is dimensionalised by VG trailing edge location, x_{vg} and VG height, h. For legend details, please refer to section 5.1 and table 5.1*

5.3 Results and discussion

Streamwise development of skin-friction coefficient, C_f determined by different methods as listed below are compared in figure 5.6

1. C_f [$\mathcal{R}$]
2. C_f [Num, GM]
3. C_f [SCR]

Streamwise development of dissipation coefficient, $C_{\mathcal{D}}$ determined by different methods as listed below are compared in figure 5.7.

1. $C_{\mathcal{D}}$ [$\mathcal{R}$ ($\mathbf{C_f}$ [Num], $\mathbf{H}^*$ [Num])]
2. $C_{\mathcal{D}}$ [Num $\leftarrow$ ($\mu(du/dy)$, -$\rho\overline{u'v'}$)]
3. $C_{\mathcal{D}}$ [Num $\leftarrow Re_\theta$]
4. $C_{\mathcal{D}}$ [DCR ($\mathbf{C_f}$ [Num], $\mathbf{U_s}$ [Num], $\mathbf{C}_\tau$ [Num])]
5. $C_{\mathcal{D}}$ [DCR ($\mathbf{C_f}$ [Num], $\mathbf{U_s}$ [DCR(H^*)], $\mathbf{C}_\tau$ [DCR (H^* [Num], U_s [DCR(H^*))])]

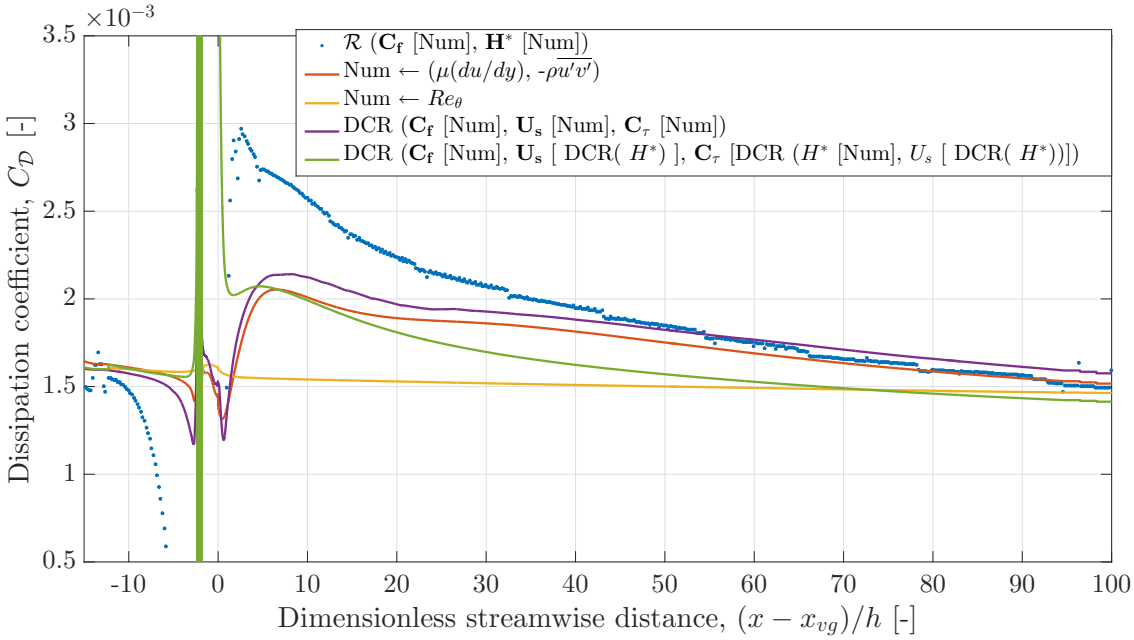

Figure 5.7: *Dissipation coefficient, $C_{\mathcal{D}}$ [-] development in streamwise direction. Streamwise distance, x is dimensionalised by VG trailing edge location, x_{vg} and VG height, h. For legend details, please refer to section 5.1 and table 5.1*

$$C_D\,[DCR] = \underbrace{\frac{C_f}{2}U_s}_{Wall(Inner)\ layer\ contribution} + \underbrace{C_\tau(1-U_s)}_{Wake(Outer)\ layer\ contribution} \tag{5.3}$$

In figure 5.8

1. $C_{\mathcal{D}}$ [$\mathcal{R}$ ($\mathbf{C_f}$ [Num], $\mathbf{H}^*$ [Num])]
2. $C_{\mathcal{D}}$ [Num ← ($\mu(du/dy)$, -$\rho\overline{u'v'}$)]
3. $C_{\mathcal{D}}$ [DCR ($\mathbf{C_f}$ [Num], $\mathbf{U_s}$ [Num], $\mathbf{C}_\tau$ [Num])]
   Inner layer contribution
   Outer layer contribution

In figure 5.9

1. $C_{\mathcal{D}}$ [$\mathcal{R}$ ($\mathbf{C_f}$ [Num], $\mathbf{H}^*$ [Num])]
2. $C_{\mathcal{D}}$ [Num ← ($\mu(du/dy)$, -$\rho\overline{u'v'}$)]
3. $C_{\mathcal{D}}$ [DCR ($\mathbf{C_f}$ [Num], $\mathbf{U_s}$ [DCR(H^*)], $\mathbf{C}_\tau$ [DCR (H^* [Num], U_s [DCR(H^*))])]
   Inner layer contribution
   Outer layer contribution

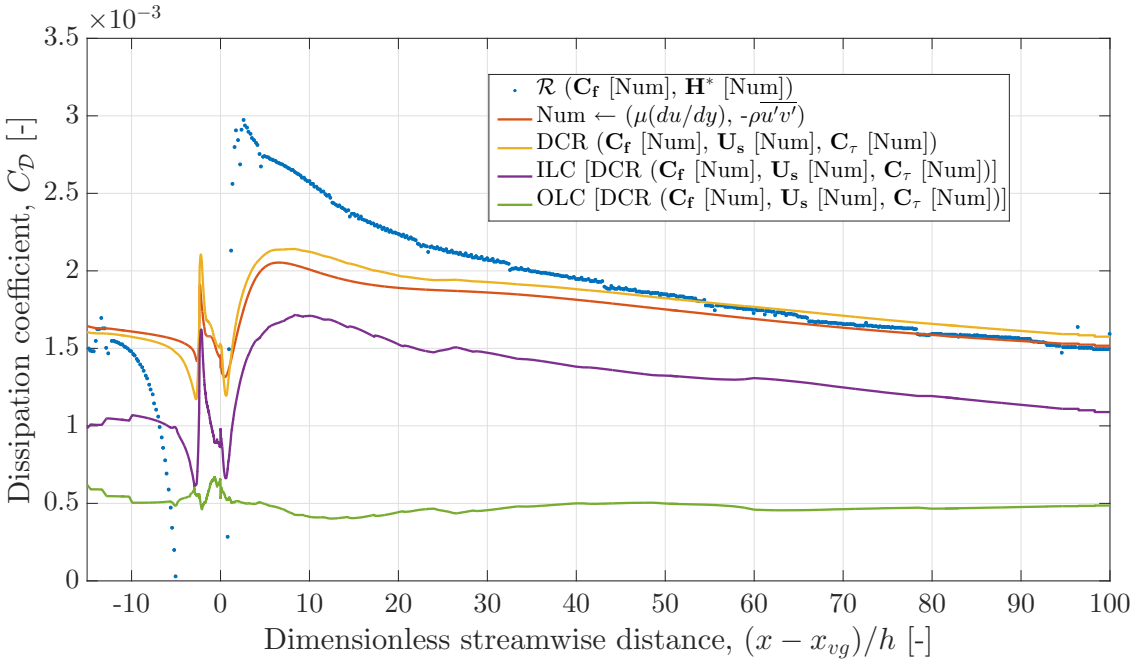

Figure 5.8

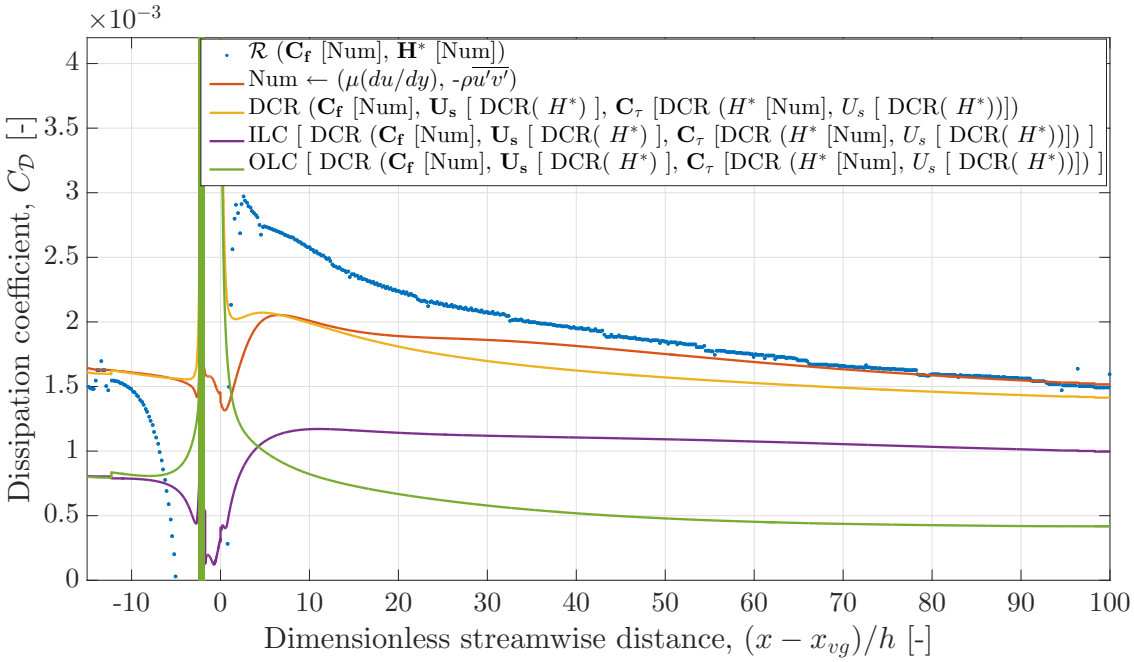

Figure 5.9

5.3.1 The conditioning effect: Is 2D or 3D mechanism predominant?

As seen in earlier sections, the 3D effects are strong till $x_{vg} = 30$ and then tend to show quasi-uniform effects. The *conditioning effect* occur at order layer of twelve boundary layer thickness downstream of VG. To recall, empirical closure $C_{\mathcal{D}}$ [Num $\leftarrow Re_\theta$] is obtained only considering $-\rho\overline{u'v'}(du/dy)$, neglecting $\mu(du/dy)^2$ contribution. majorly -$\rho\overline{u'v'}$, neglecting $\mu(du/dy)$ contribution. Given, that has it's own inaccuracies. This comparison gives an indication the $\mu(du/dy)$ is the predominant effect. $\mu(du/dy)$ can be interpreted as the wall contribution and -$\rho\overline{u'v'}$ as the wake contribution (see 5.3).

Bradshaw et al. [8] states that the shear stress $-\rho\overline{u'v'}$ is closely related to the kinetic energy $\frac{1}{2}\rho\left(\overline{u^2}+\overline{v^2}+\overline{w^2}\right)$. Also, formulates an empirical relation. Drela and Giles [16] this empirical relation for the shear lag equation. Kerho et al. [26] approach of adding a step function and decaying based on vortex decay strength. Clearly does not work current dataset investigated. Adding a step function, would indirectly indicate $-\rho\overline{u'v'}$ is the major part of the kinetic energy $\frac{1}{2}\rho\left(\overline{u^2}+\overline{v^2}+\overline{w^2}\right)$.

5.4 Key integral parameter

A quote extracted from Cebeci and Smith [10][1]

> *Shall I refuse my dinner because I do not full understand the process of digestion ?*
>
> Oliver Heaviside
> according to von Kármán and Biot

From section, it is quite evident that the VGIF exhibit strong 3 D mechanism till 30 device heights downstream of trailing edge of VGs. Then, tend to exhibit quasi-uniform properties further downstream locations. Also, there is uncertainty in obtaining the skin-friction and dissipation coefficient as seen in section. However, drawing motivation from Cebeci and Smith [10] take on Heaviside's admonition, step 7 as per detailed approach is discussed in this section. Of course, it not in the same magnitude as the previous comparison. Author is merely trying to convey to the reader with the uncertainties and limited analysis of linking the 3 D mechanism to the integral parameters of interest, that it is not outrageous to identify the key integral parameter for VGIF.

Neglect skin friction, focus on dissipation. As it is composite closure. At hundred device heights from the trailing edge of VGs, the dissipation seem to converge at value of 1.5. What happens is open to debate. To recall, C_f, H^* and C_τ are closure relations. Turbulent closure relation are listed in Drela are used and is plotted.

Dissipation coefficient, $C_{\mathcal{D}}\,[\mathcal{R}]$ determined by equation 5.2 the ILC and OLC are not clearly identifiable. New terms *Apparent Inner Layer Contribution* and *Apparent Outer*

[1] Original context : Like Heaviside's operational calculus in its early days, the theory of turbulent flows lacks solid formulations. If we waited to perform applied calculation until we had laid these solid formulations, the wait would surely be very long.

Layer Contribution are introduced through equations 5.4 and 5.5]. Term *apparent*[2] is used as effective slip velocity, U_s and shear stress coefficient, C_τ are not used explicitly in equation 5.2. U_s, C_τ determined from VGIF as some uncertainty is method used (see **??**) as well as numerical uncertainty in using the method. $AILC$ and $AOLC$ are important parameter to compare the $C_\mathcal{D}$ and C_f from integral relations and closure relations. Is discussed more in detail.

From previous chapters we have seen multiple method by which kinetic energy shape parameter, skin-friction coefficient, effective slip velocity, shear stress coefficient and dissipation coefficient can be obtained. Every method has fair share of uncertainties and is critique. This section can compare different coefficient determined by different methods. Table 5.1 give indicates the terminology used in comparison. From a quick glance, there are lot of possible comparison. Motivation for each comparison and inference is written down.

Drela and Giles [16] $C_\mathcal{D}$ as sum of wall layer contribution and wake layer contribution (for ease of reference it is repeated here 5.3). As discussed in section **??** for VGIF it can be considered has three layers. It is more appropriate re-term *Wall layer contribution* as *Inner layer Contribution, ILC* and *Wake Layer Contribution* as *Outer layer contribution, OLC*.

$$AILC\left[C_\mathcal{D}\left[\mathcal{R}\right]\right] = C_\mathcal{D}^\mathcal{R} - \underbrace{\left[C_\tau(1-U_s)\right]}_{OLC} \tag{5.4}$$

$$AOLC\left[C_\mathcal{D}\left[\mathcal{R}\right]\right] = C_\mathcal{D}^\mathcal{R} - \underbrace{\left[\frac{C_f}{2}U_s\right]}_{ILC} \tag{5.5}$$

Therefore,

$AILC/ILC$ and $AOLC/OLC$ would be parameter indicate the change.

1. $C_\mathcal{D}$ [$\mathcal{R}$ ($\mathbf{C_f}$ [SCR], $\mathbf{H^*}$ [DCR])]
2. $C_\mathcal{D}$ [DCR ($\mathbf{C_f}$ [SCR], $\mathbf{U_s}$ [DCR(H^*)], $\mathbf{C}_\tau$ [DCR (H^* [DCR], U_s [DCR(H^*))])]

In a sense, it is not able imitate the quasi-uniform effect. The dissipation coefficient is values off. By correction ratios it seems both need to be factor of 2 even further downstream locations. Karmer approach is to mimic the vortex decay, in ctau is icnreased then Cf is increased. Us also change accoriding to that. So one can't simply Ctau as it linked to other parameter. Hence, in a sense it other approaches to mimic it. So it Might give a result. It is not pursed. From the spanwise averaged values, it is evident the contribution from the wall layer is major contributing term in determining the dissipation for numerical data and Drela and Giles [16] closure relations. From numerical dataset, wall contribution is the only ,major factor after 50 VG heights downstream of VGs. Drela and Giles [16] closure relations is qualitatively similar , but a lower value. An interesting

[2]Author uses definition of **apparent** as [before noun] seeming to be true but possibly not true. Considering *Wall layer contribution* and *Wake layer contribution* as qualities (noun) of the flow.

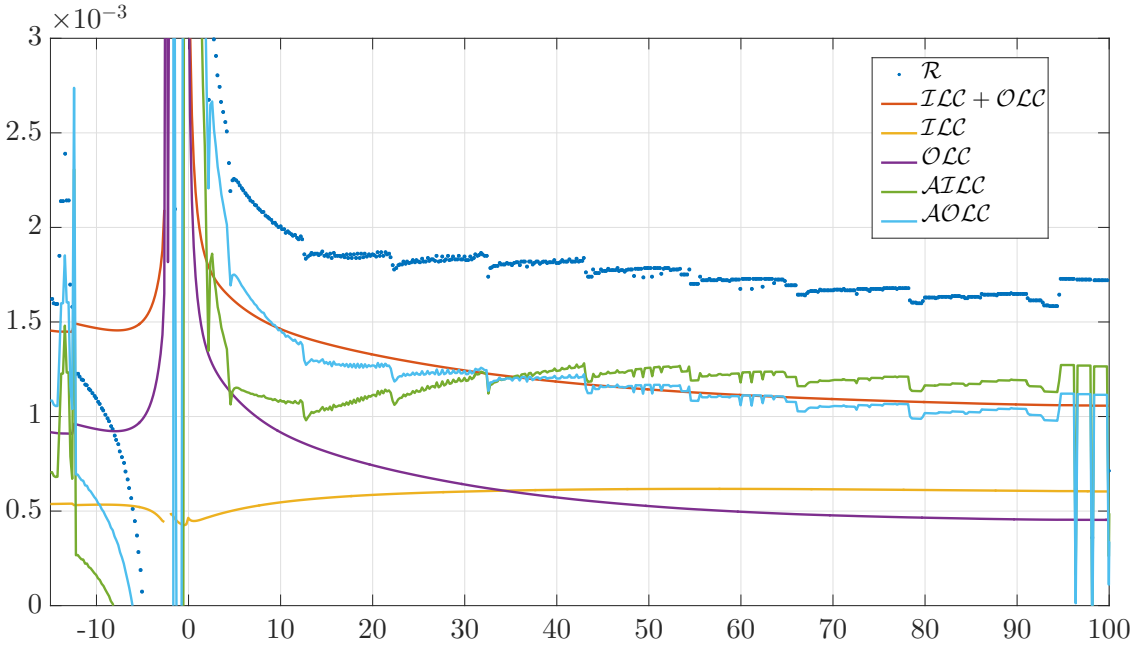

Figure 5.10: *Dissipation coefficient obtained using only turbulent closure relations*

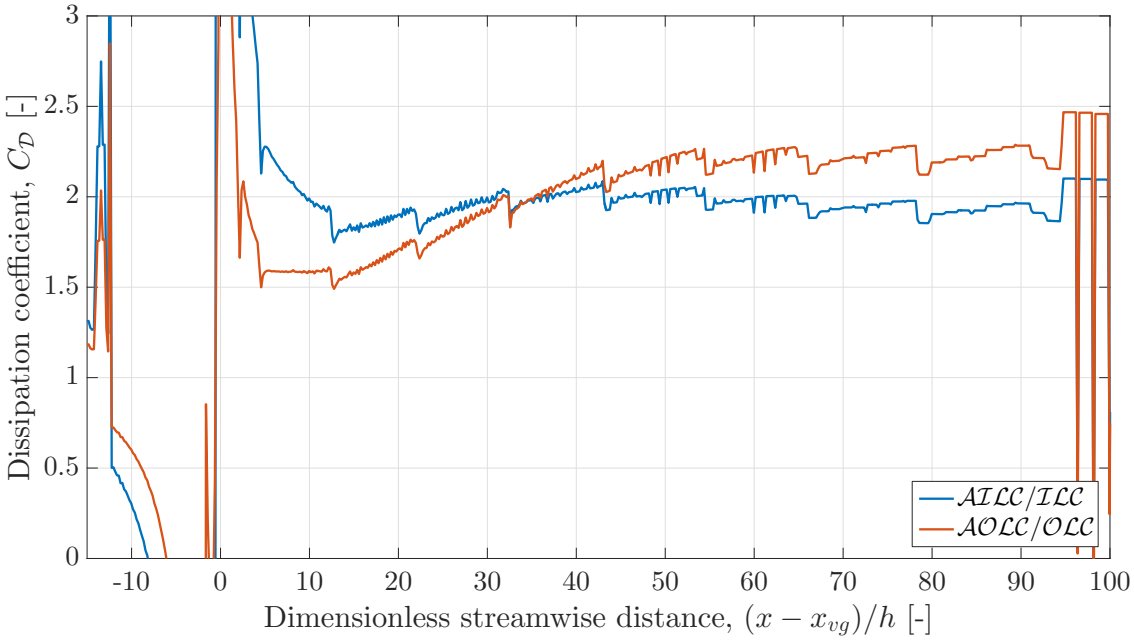

Figure 5.11: *Performance comparison. Using only turbulent closure relations*

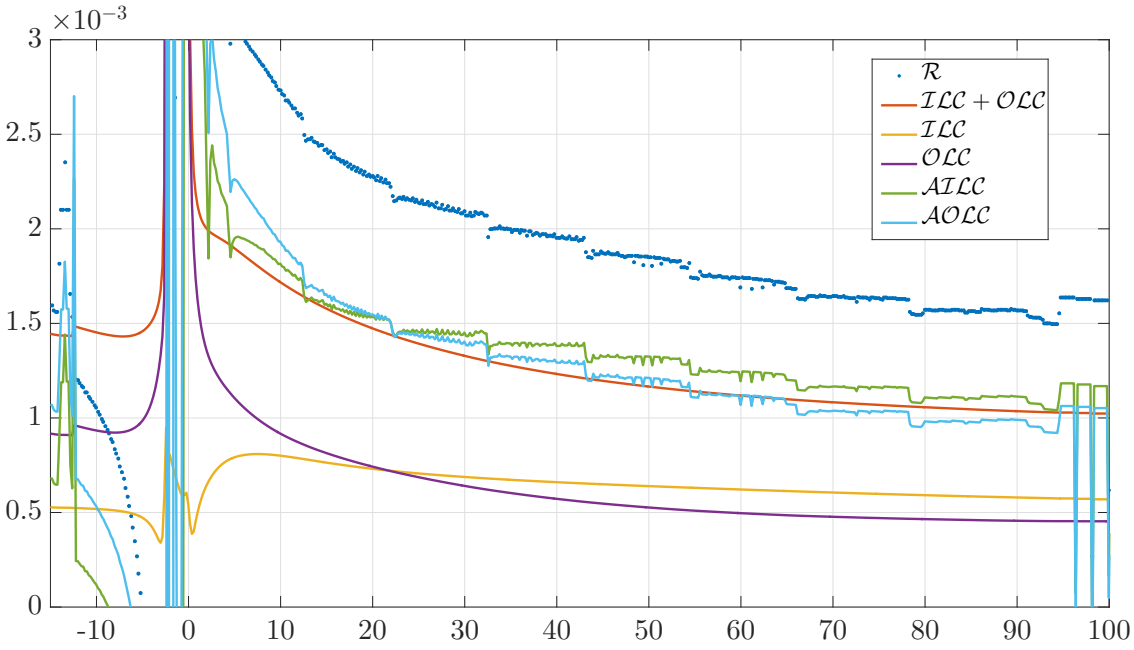

Figure 5.12: *Dissipation coefficient obtained using only turbulent closure relations with corrected skin-friction value*

trend is at $z/D = 0.487$ we see that contribution from the wake layer is higher for the closure relations. Inner contribution (Wall layer contributions) and Outer contributions (Wake layer contributions). On other hand, skin-friction is single formula. Godard and Stanislas [22] uses skin-friction as an optimal parameter. Also indicates drag would be less or different. This also enhances the claim against Godarad and Stansis opisitmation with just skin friction as optimal parameter.Inputting the correct skin-friction coefficient, could be interpreted as if Swafford emperical relation has been tweaked to be valid for VGIF. Still the R and ILC and OLC.

1. $C_{\mathcal{D}}$ [$\mathcal{R}$ ($\mathbf{C_f}$ [Num], $\mathbf{H}^*$ [DCR])]
2. $C_{\mathcal{D}}$ [DCR ($\mathbf{C_f}$ [Num], $\mathbf{U_s}$ [DCR(H^*)], $\mathbf{C}_\tau$ [DCR (H^* [DCR], U_s [DCR(H^*))])]

5.4.1 Inputting the correct effective slip velocity parameter

[5] suggest vortex trajectory is an important criterion. A hypothesis was made that the effective slip velocity parameter, somehow indicates the vortex trajectory. Changing effective slip velocity parameter would mean the inner and outer contribution is changed.

1. $C_{\mathcal{D}}$ [$\mathcal{R}$ ($\mathbf{C_f}$ [SCR], $\mathbf{H}^*$ [DCR])]
2. $C_{\mathcal{D}}$ [DCR ($\mathbf{C_f}$ [SCR], $\mathbf{U_s}$ [Num], $\mathbf{C}_\tau$ [DCR (H^* [DCR], U_s [DCR(H^*))])]

1. $C_{\mathcal{D}}$ [$\mathcal{R}$ ($\mathbf{C_f}$ [SCR], $\mathbf{H}^*$ [DCR])]

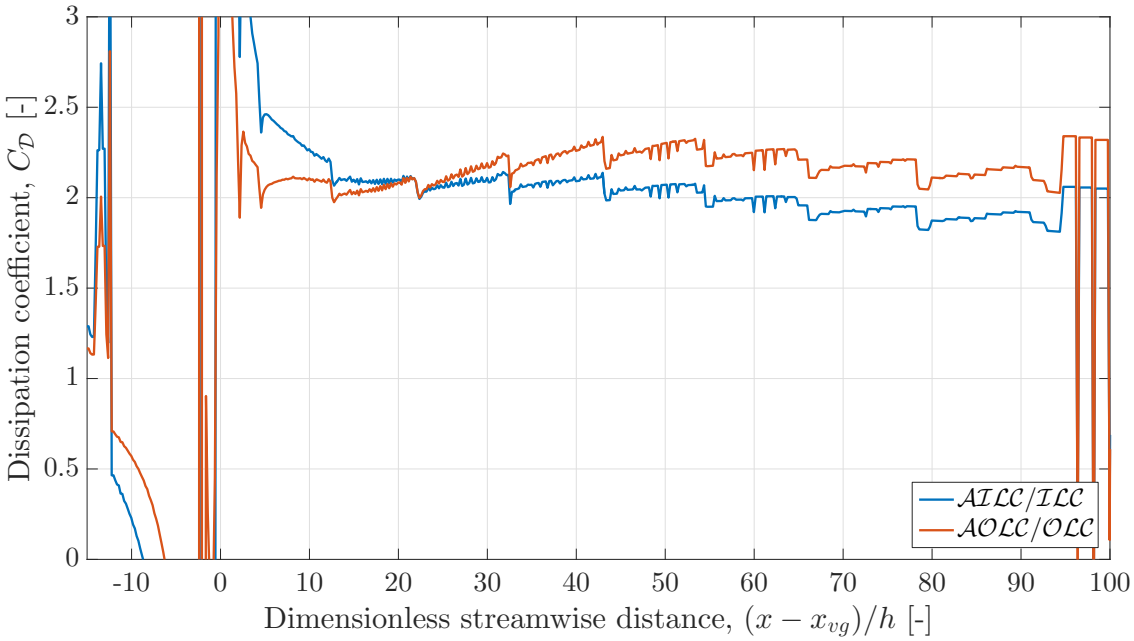

Figure 5.13: *Performance comparison.Using only turbulent closure relations with corrected skin-friction value*

2. $C_{\mathcal{D}}$ [DCR ($\mathbf{C_f}$ [SCR], $\mathbf{U_s}$ [LeBauler Thomas (CfSwafford)], $\mathbf{C}_\tau$ [DCR (H^* [DCR], U_s [DCR(H^*))])]

For [45] state downstream of VGs represent the as if the favourable pressure gradient further upstream. Clauser's concept of equilibrium boundary layers in adverse pressure, determines eddy viscosity which is effectively constant for 80-90 % . Ku$delta^*$. = 0.018 .

For investigated dataset, the wall shear stress plays a vital role. Possibly a bias due to [22] configuration.Drela [15] states "Vortex generators increase dissipation by introducing streamwise vortices into the boundary later at some distance from the wall ". Lin [29] which states that the effective "As a sign of their flow-control efficiency, the low-profile VGs use the approach of minimal near-wall protuberances to produce streamwise vortices just strong enough to overcome the baseline separation without unnecessarily persisting within the boundary layer once flow attachment is achieved."

Total profile drag is defined as the sum of skin friction drag (often referred as friction drag) and pressure drag (often referred as form drag). Total profile drag contribution can be interpreted in different ways. Since the two-dimensional dissipation integral method is considered, it will be discussed based on the power-balance view as mentioned in Drela [15].Drela [15] states that viscous dissipation is ultimately responsible for total profile drag, including the pressure drag component. The adverse pressure gradient capability of the boundary layer can be increased by increasing its dissipation away from the surface. Vortex generators, if designed accordingly, can increase dissipation away from the wall. Therefore to lower drag, dissipation has to be reduced. Vortex generator generates streamwise vortices and enhances the mixing process in turbulent flow regime. Hence, drag is always increasing with additions of VGs. *Lower drag*: the comparison is always

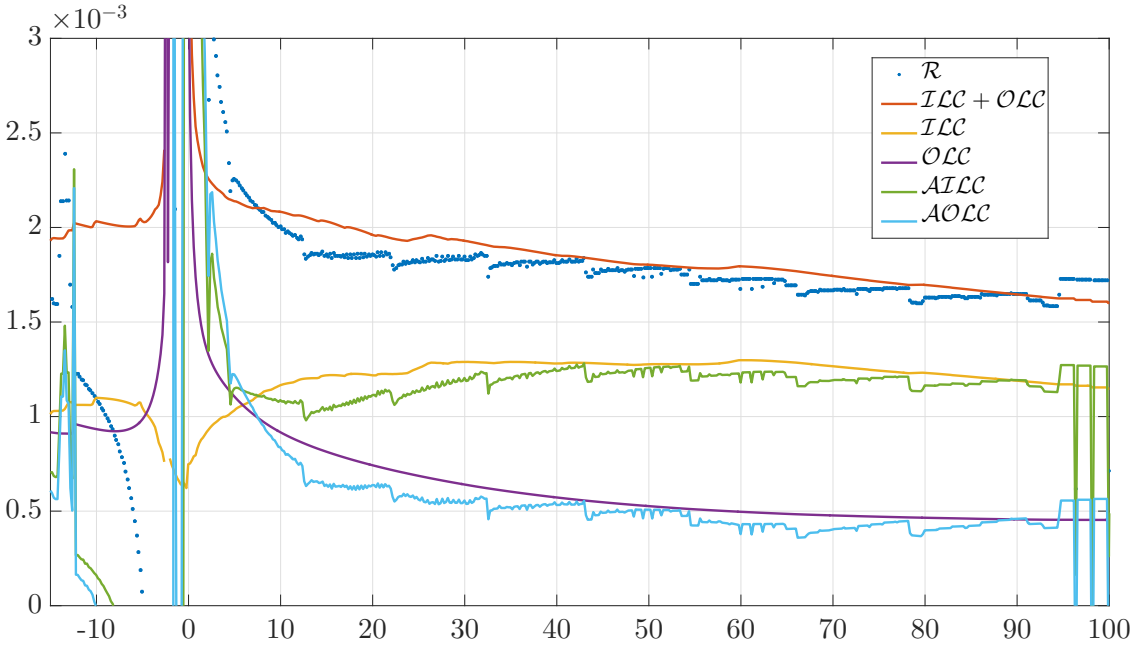

Figure 5.14: *Dissipation coefficient obtained using only turbulent closure relations with corrected effective slip velocity parameter value.*

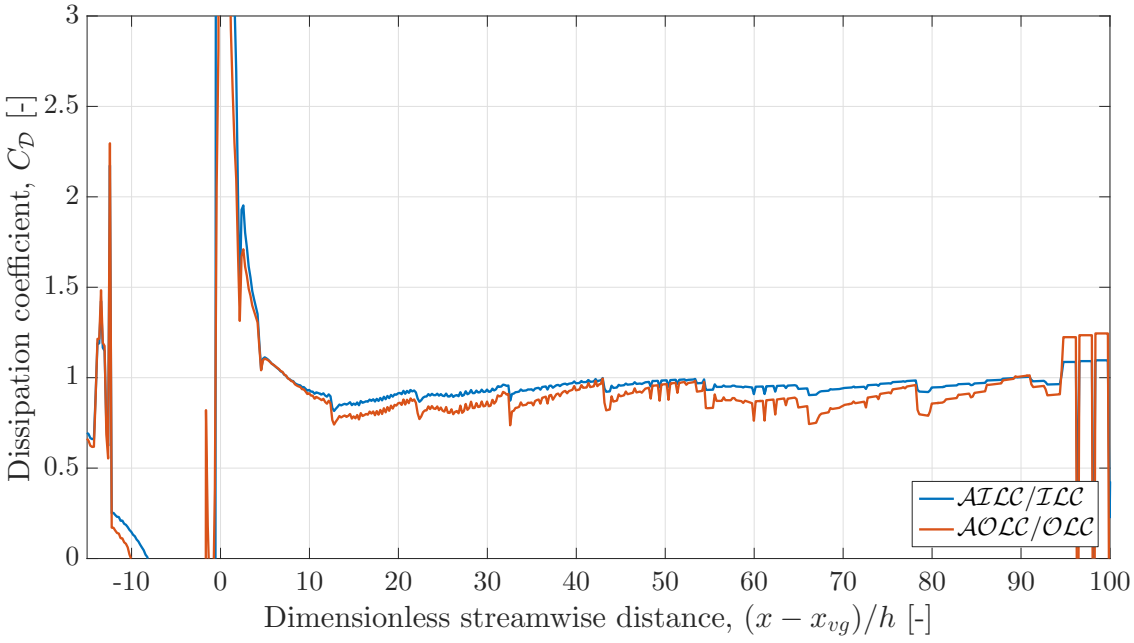

Figure 5.15: *Dissipation coefficient obtained using only turbulent closure relations with corrected effective slip velocity parameter value.*

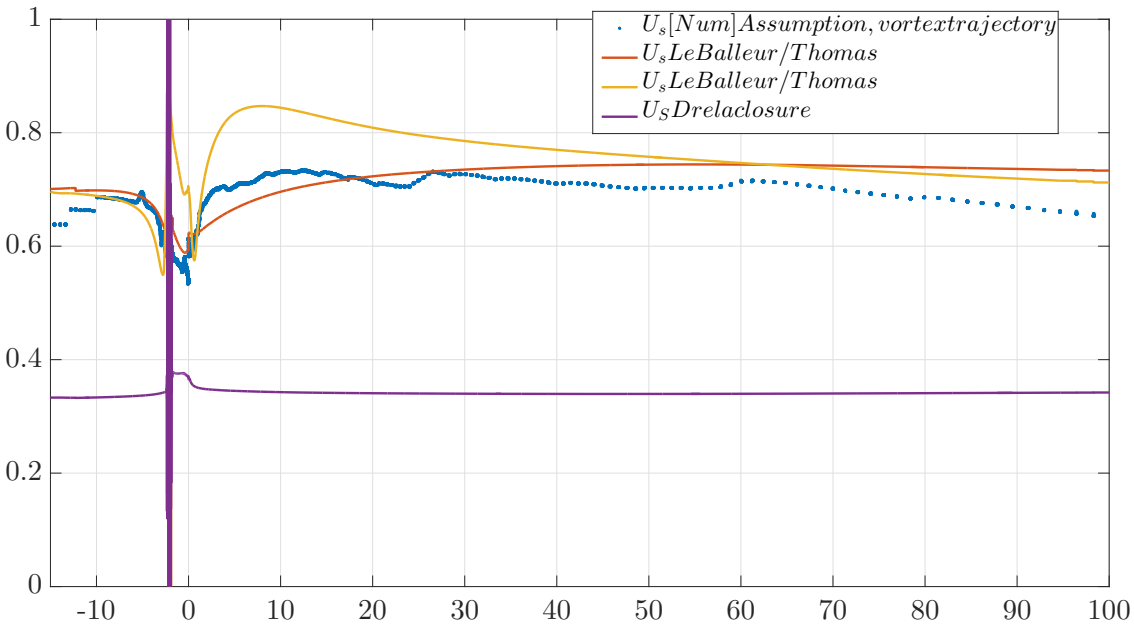

Figure 5.16

made to an alternative VG configuration.To increase adverse pressure gradient capability,

$$\Lambda_{\min} = \left(\frac{\theta}{u_e}\frac{du_e}{ds}\right)_{\min} = \frac{1}{H-1}\left(\frac{c_f}{2} - \frac{2c_D}{H^*}\right) \tag{5.6}$$

It is only valid for equilibrium flow condition. For shape parameter, H value of 1.4 and Reynolds number of 2500 was chosen. It is indicative of values for the uncontrolled case flow conditions.

$\Delta C_f\%$	$\Delta C_\tau\%$	$\Delta C_\mathcal{D}\%$	$\Delta\Lambda_{\min}\%$
0.7	0.3	0.54	-3.17
0.3	0.7	0.46	4.17

Table 5.2: *Maximum tolerable adverse pressure gradient*

From an ideal integral modelling perspective, it should be able to model both for domineering wall shear stress or Reynolds shear stress value or equal effect. Modifying the inner and outer layer contribution, through effective slip velocity parameter is a way forward.

Part IV

Conclusion

Chapter 6

Conclusion

The principal aim of the thesis is to determine the most relevant parameter(or s) for the validation of a two-dimensional integral boundary layer solution method(or s) for vortex generator induced flow. Dissipation integral method of Drela and Giles [16] is selected for the integral boundary layer analysis. The turbulent closure relations (mentioned in [16]) fail to predict VGIF. Indirect techniques (using velocity profile information) to estimate the skin-friction coefficient also fail. VGIF exhibit quasi-uniform effect twelve times the boundary layer thickness for the dataset analysed. It raises doubt about the wake measurements at the centre line downstream of flat plate/aerofoil for estimating drag. It is quite evident, the VGIF does not fall into the category of attached or separated smooth wall-bounded flow for which Drela and Giles [16] is formulated. Modifying the slip velocity concept for VGIF is suggested as a solution. Then, effective slip velocity parameter would be the key integral parameter for the validation of two-dimensional dissipation integral boundary layer solution (Drela and Giles [16]) for vortex generator induced flow.

To characterise the turbulent flow properties for VGIF direct wall shear stress measurements is required. Oil film interferometry is one such technique; it is implemented successfully for 3D non-equilibrium flows. Uncertainty in determining dissipation coefficient needs to be quantified; it requires drag measurements along with Reynolds stress measurement where VGIF exhibit strong non-quasi-uniform properties.

Part V

Appendix

Appendix A

Skin-friction coefficient estimation method comparison

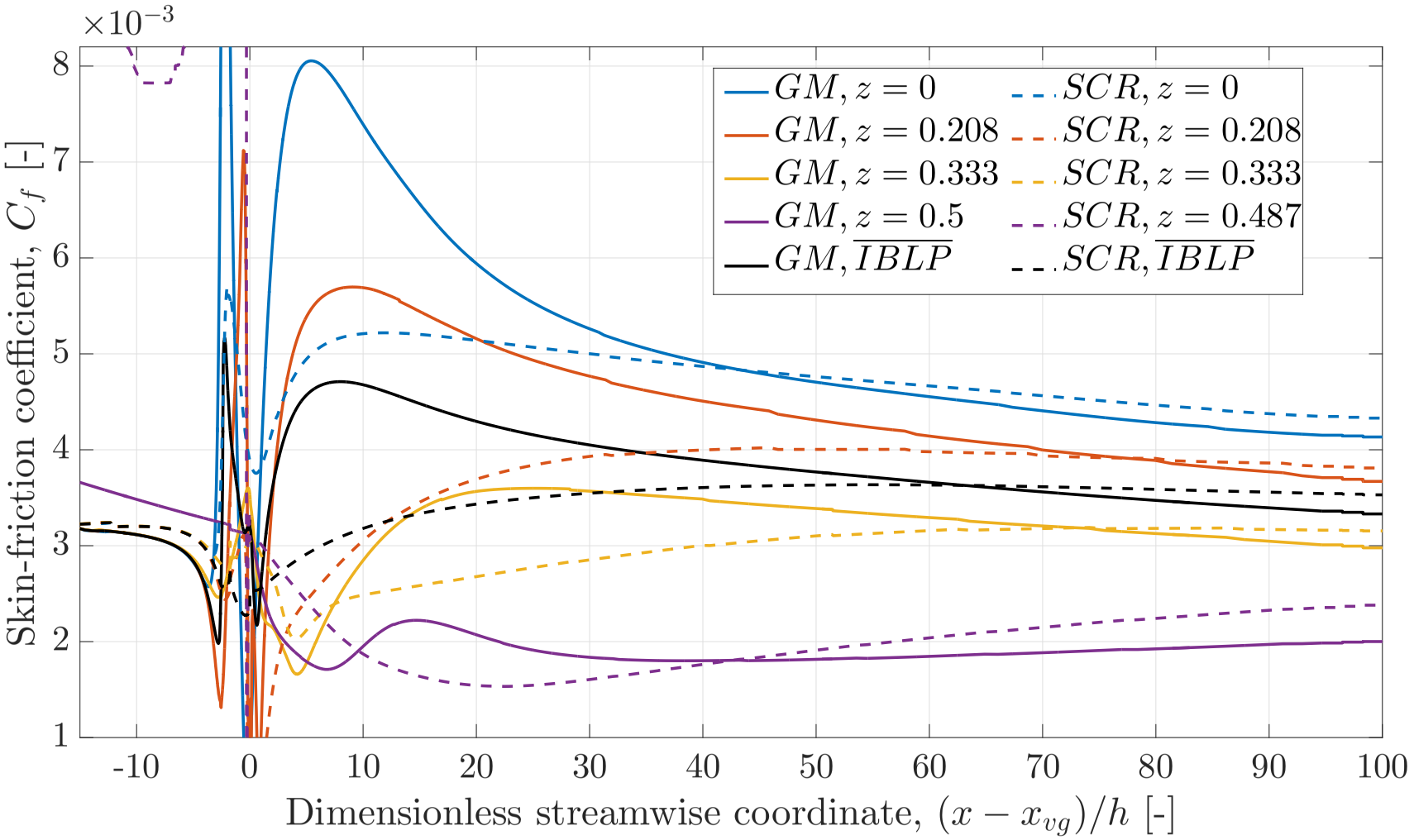

Figure A.1: *Skin-friction coefficient, C_f [-] development in streamwise direction for vortex generator, (VG) case from numerical dataset obtained using gradient method, [GM] (see 3.3.1) is compared with C_f obtained from Swafford's closure relation, [SCR] (see 3.2). Comparison is done at different spanwise locations, $(z/D = 0, 0.208, 0.333, 0.487)$ and spanwise averaged value. Streamwise distance, x is dimensionalised by VG trailing edge location, x_{vg} and VG height, h.*

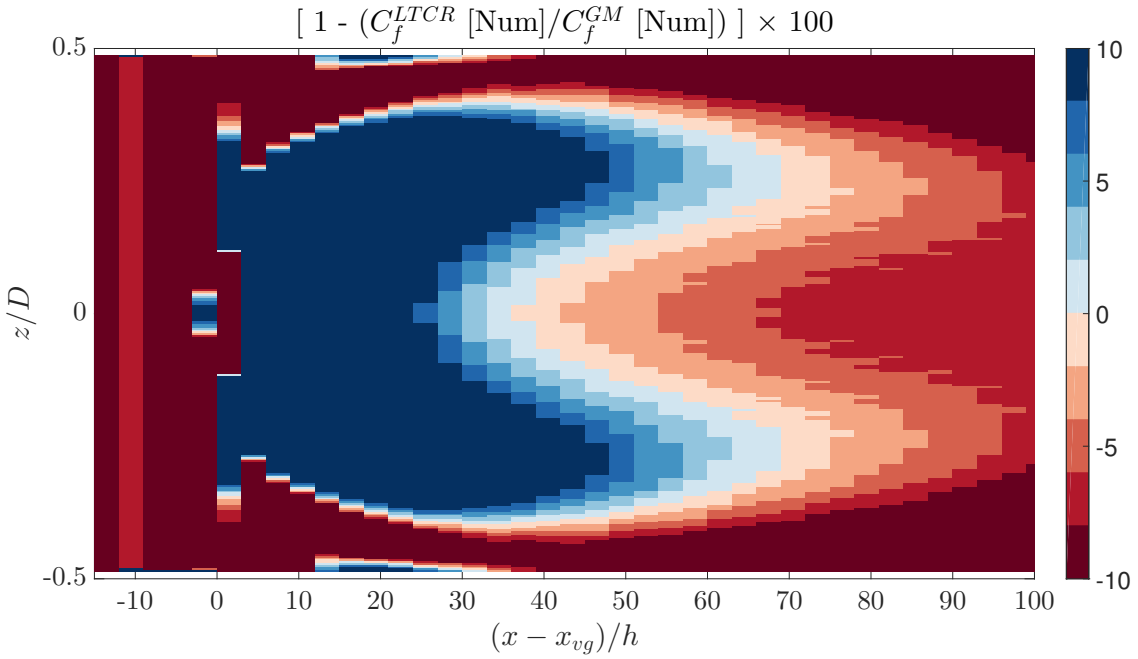

Figure A.2

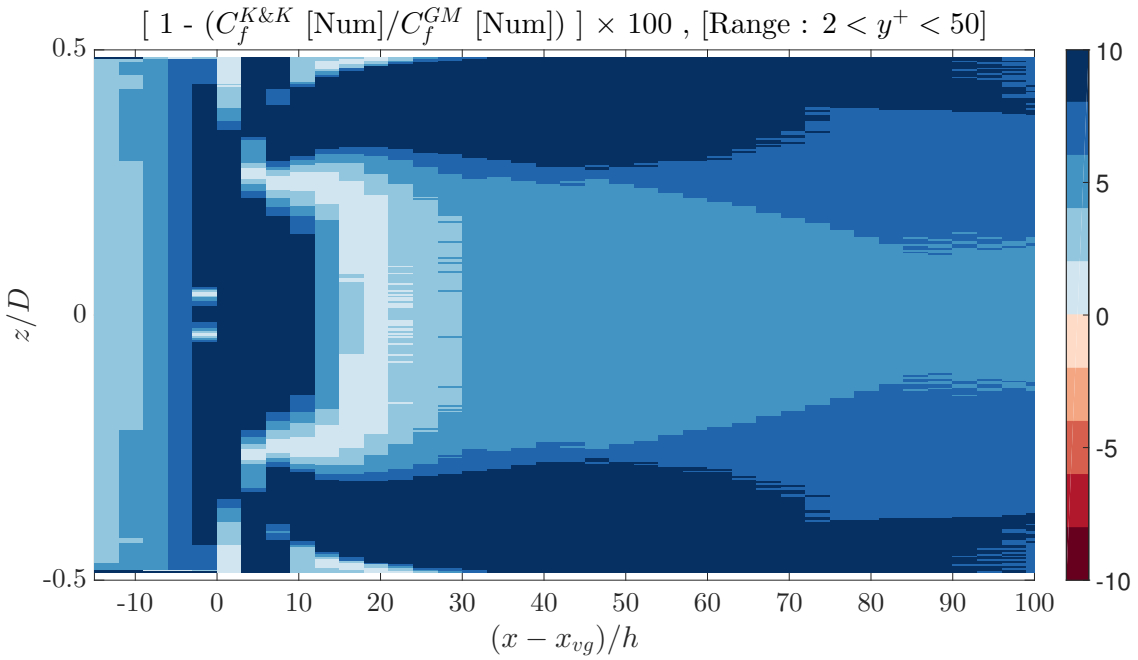

Figure A.3

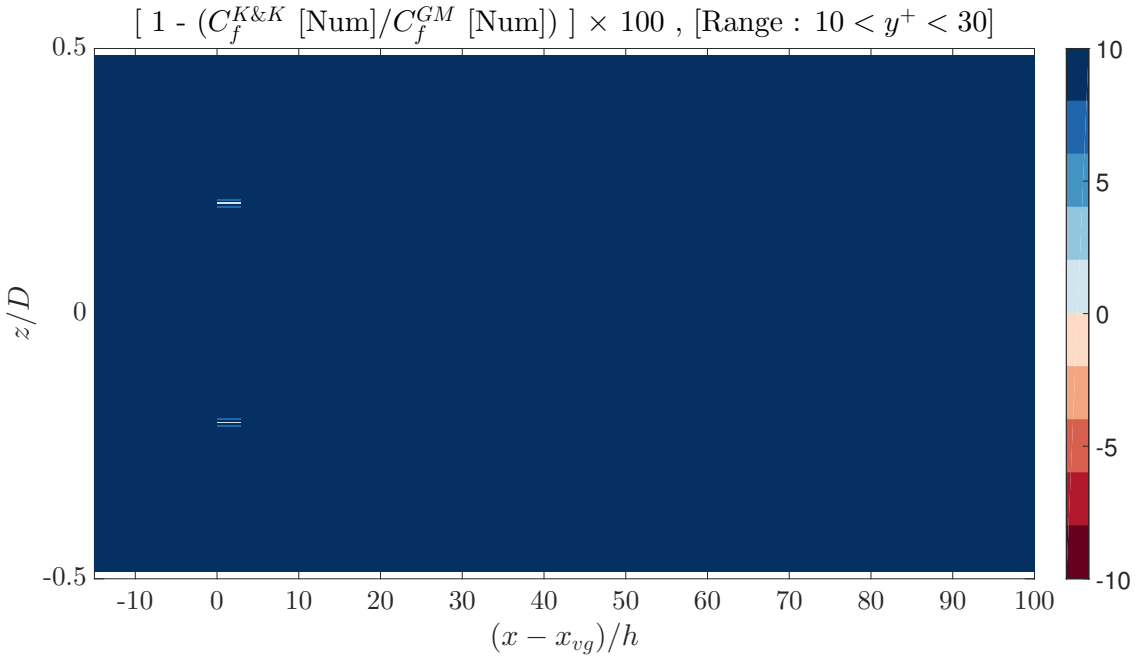

Figure A.4

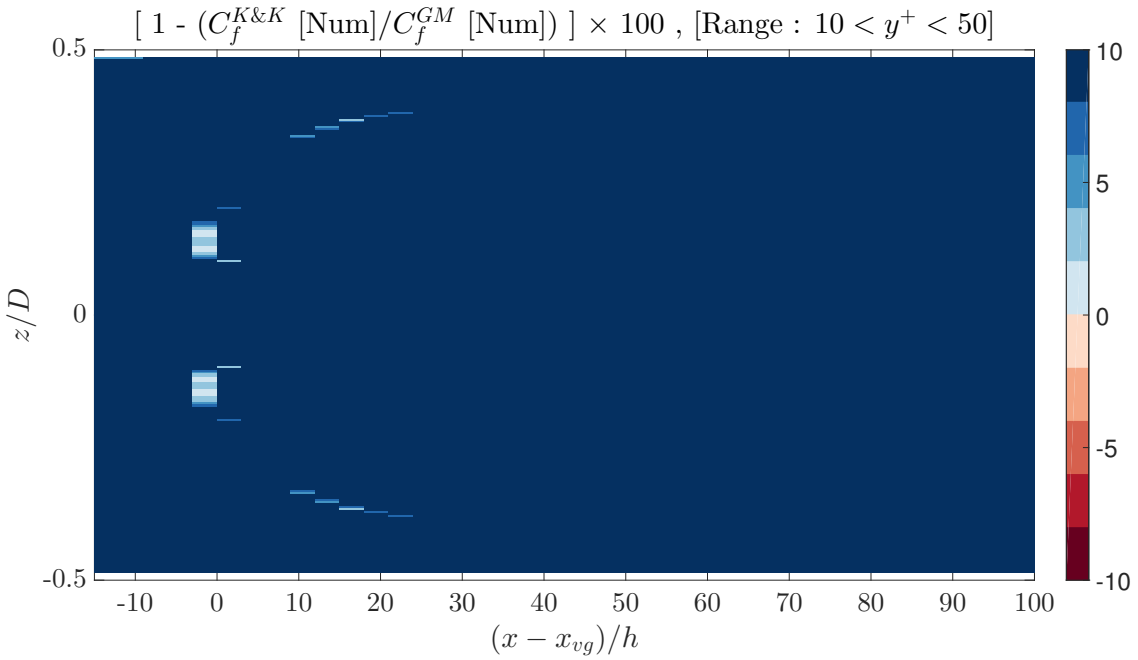

Figure A.5

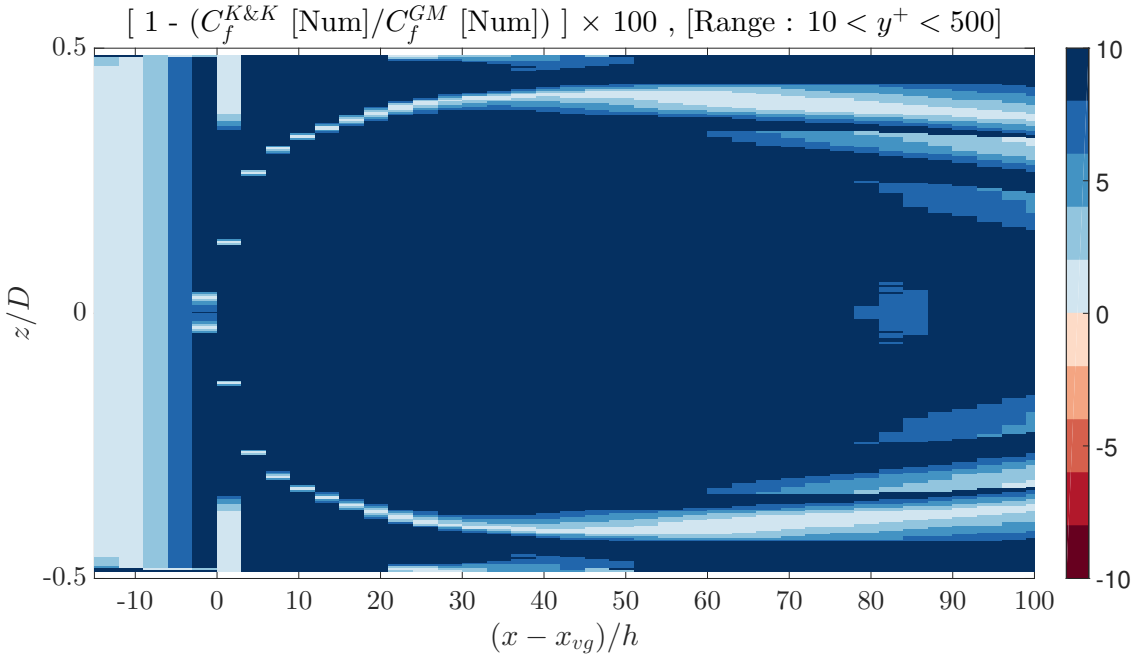
[1 - ($C_f^{K\&K}$ [Num]/C_f^{GM} [Num])] × 100 , [Range : $10 < y^+ < 500$]
0.5
0
-0.5
z/D
-10
0
10
20
30
40
50
60
70
80
90
100
$(x - x_{vg})/h$
10
5
0
-5
-10

Figure A.6

Appendix B

Dimensionless Profile

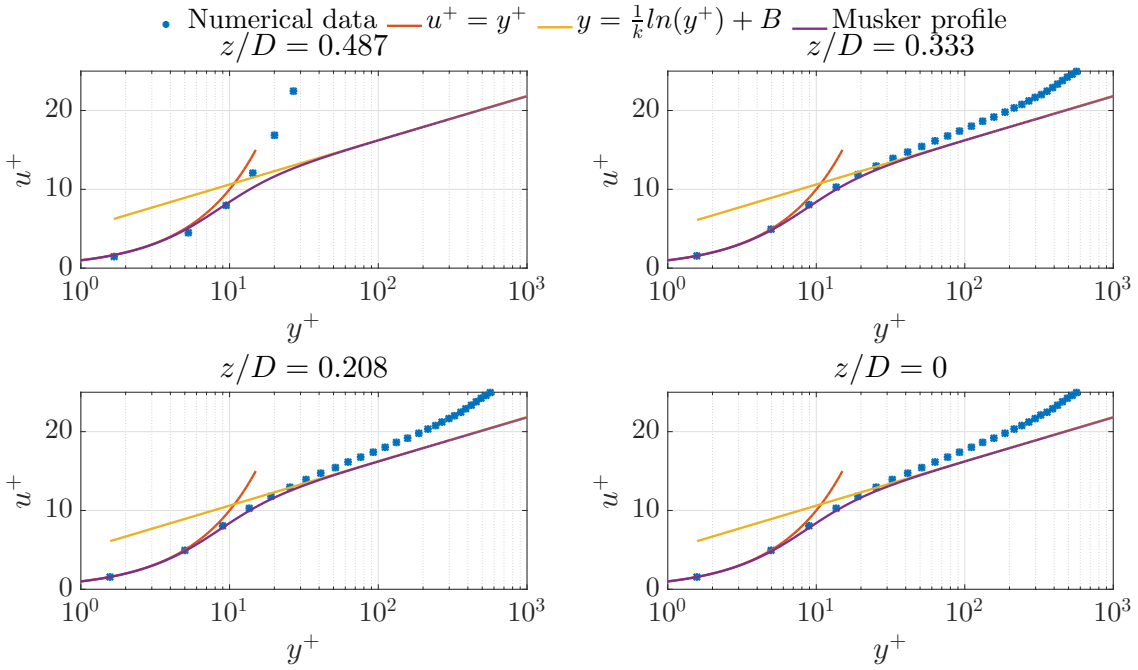

Figure B.1: *Comparison of velocity profile for VG test case [numerical dataset] at* $(x - x_{VG})/h = -10$ *with Musker profile at different spanwise locations.*

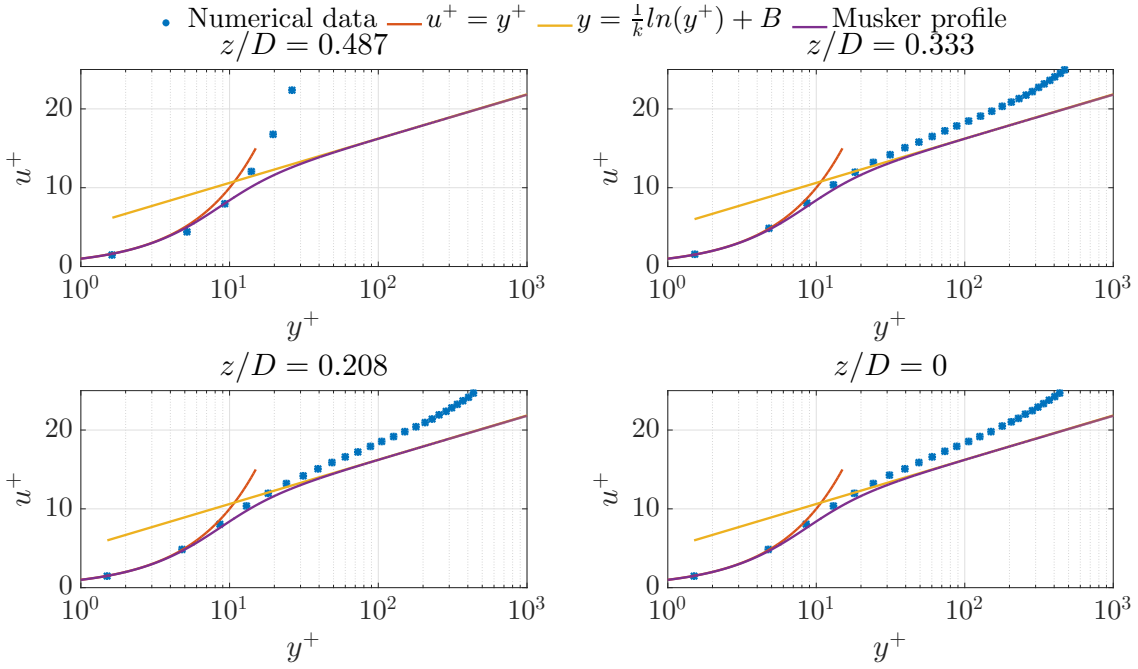

Figure B.2: *Comparison of velocity profile for VG test case [numerical dataset] at* $(x - x_{VG})/h = -5$ *with Musker profile at different spanwise locations.*

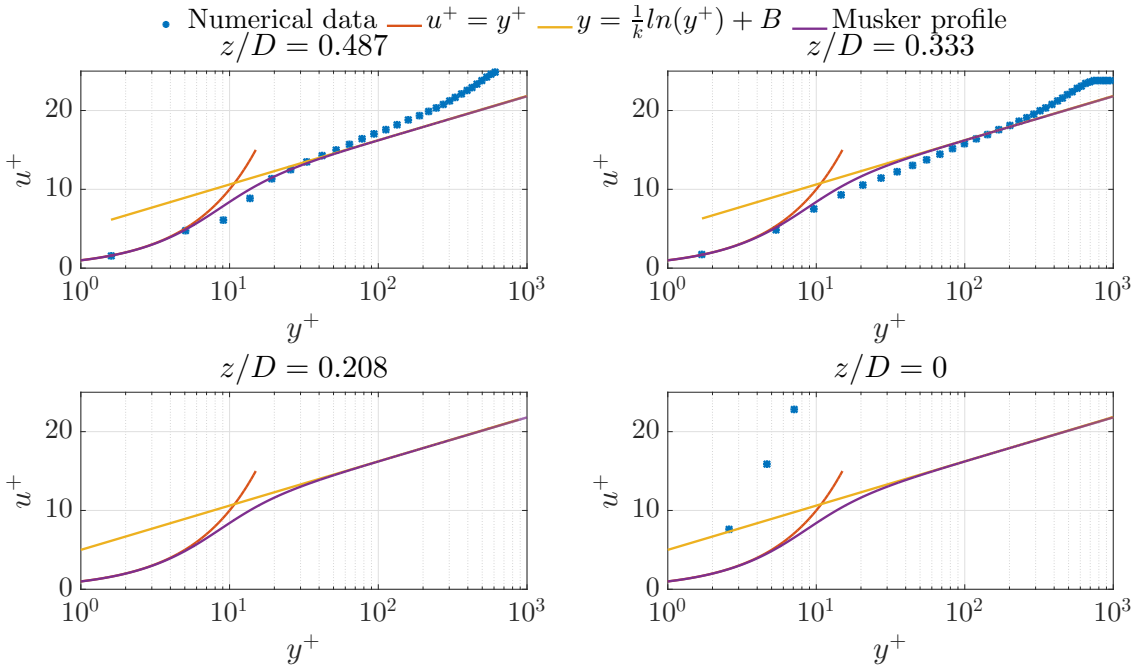

Figure B.3: *Comparison of velocity profile for VG test case [numerical dataset] at* $(x - x_{VG})/h = 0$ *with Musker profile at different spanwise locations.*

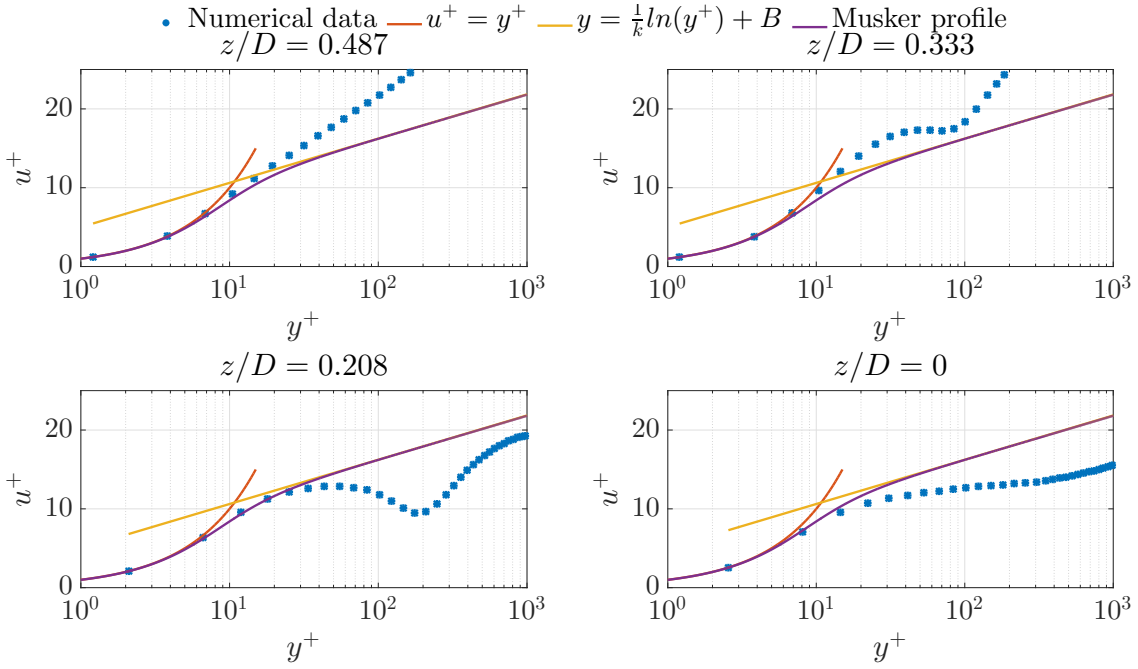

Figure B.4: *Comparison of velocity profile for VG test case [numerical dataset] at* $(x - x_{VG})/h = 5$ *with Musker profile at different spanwise locations.*

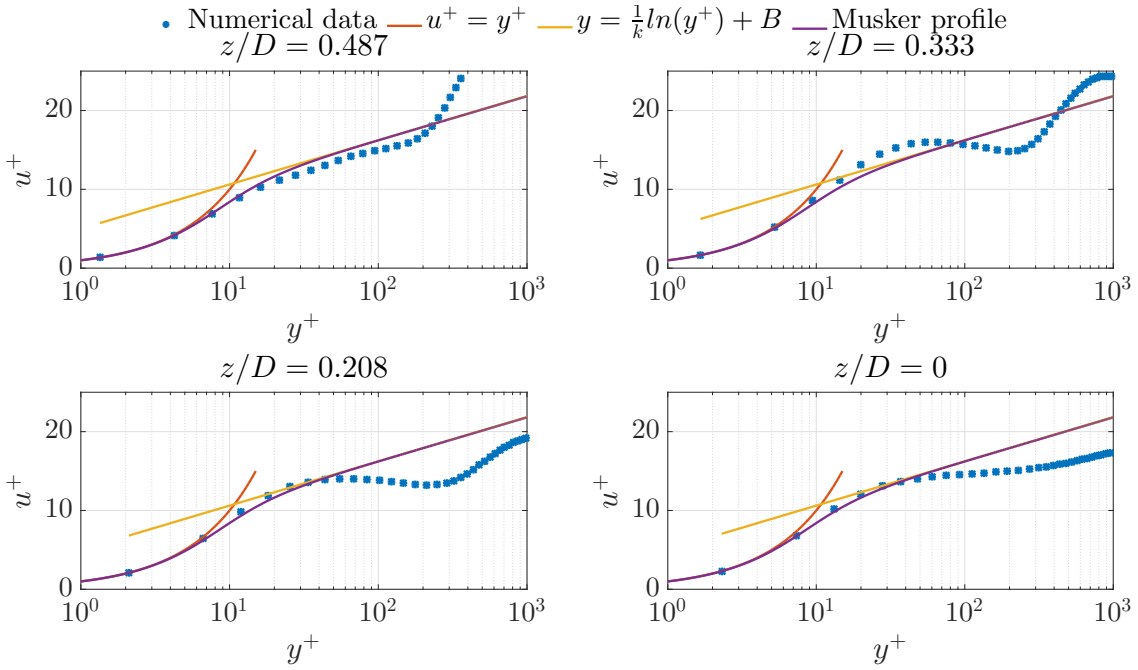

Figure B.5: *Comparison of velocity profile for VG test case [numerical dataset] at* $(x - x_{VG})/h = 15$ *with Musker profile at different spanwise locations.*

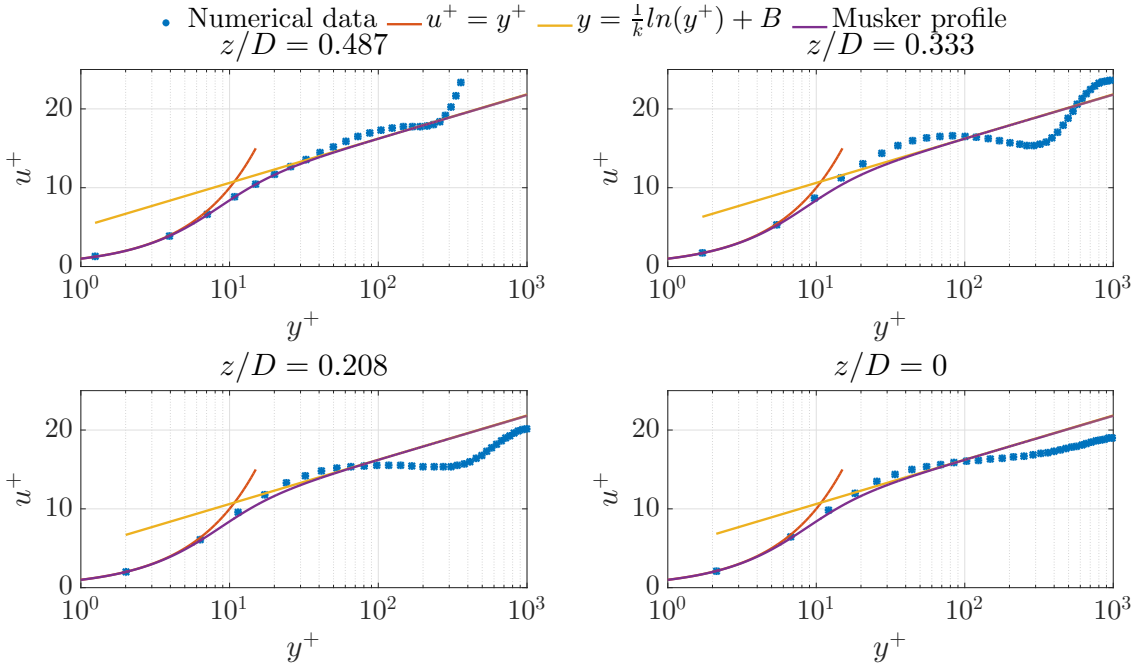

Figure B.6: *Comparison of velocity profile for VG test case [numerical dataset] at* $(x - x_{VG})/h = 25$ *with Musker profile at different spanwise locations.*

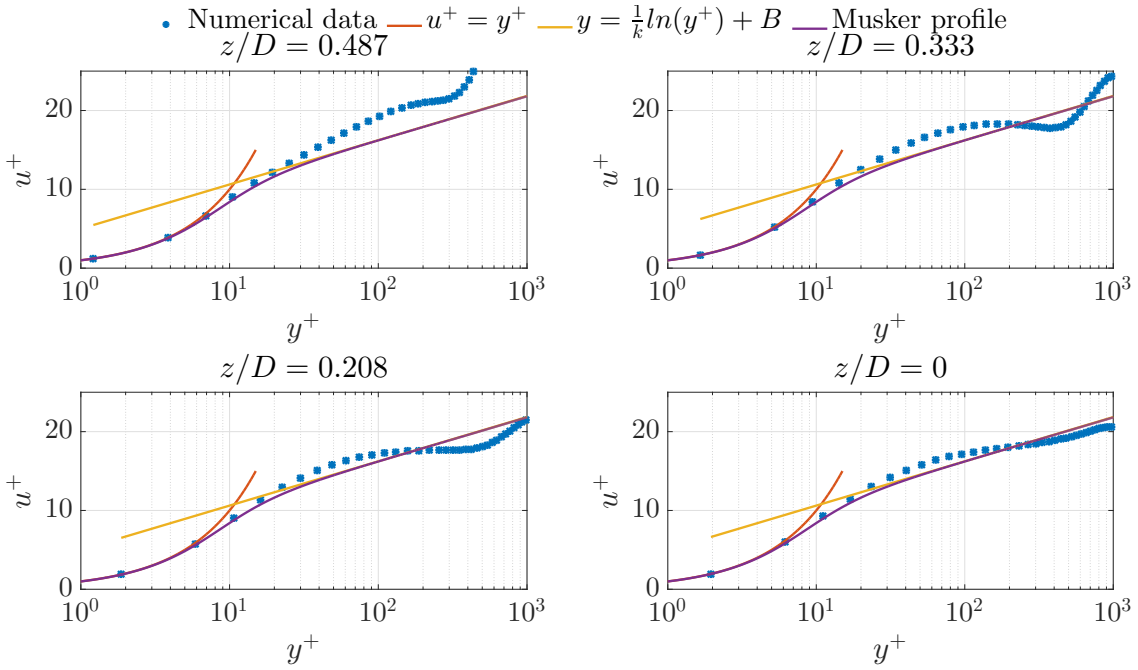

Figure B.7: *Comparison of velocity profile for VG test case [numerical dataset] at* $(x - x_{VG})/h = 50$ *with Musker profile at different spanwise locations.*

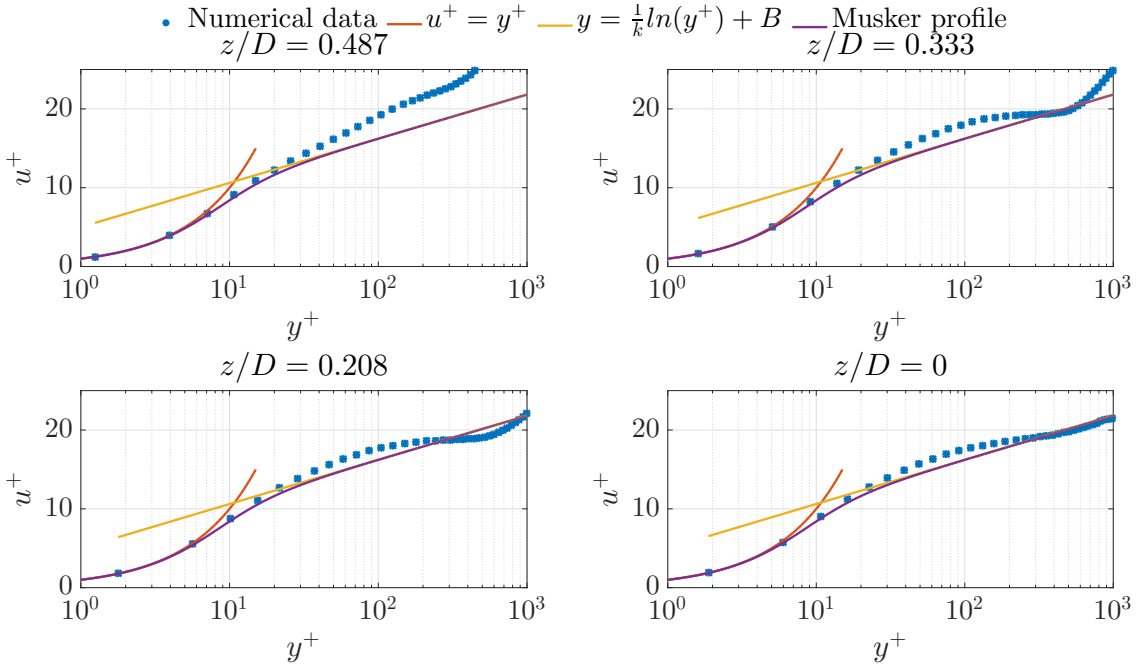

Figure B.8: *Comparison of velocity profile for VG test case [numerical dataset] at* $(x - x_{VG})/h = 75$ *with Musker profile at different spanwise locations.*

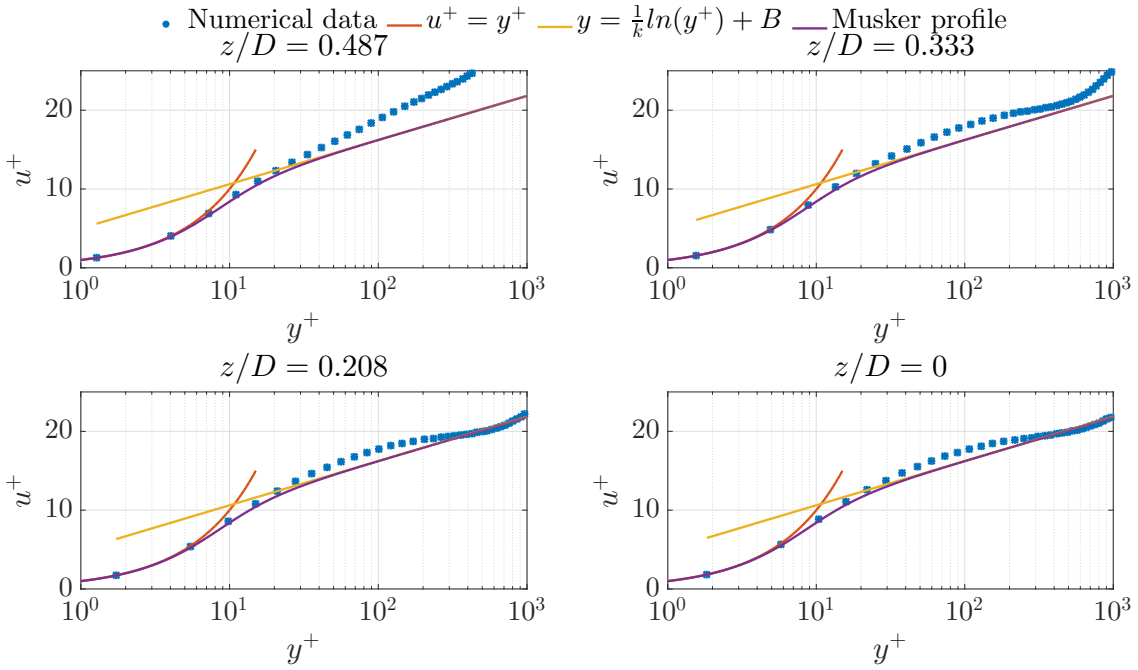

Figure B.9: *Comparison of velocity profile for VG test case [numerical dataset] at* $(x - x_{VG})/h = 100$ *with Musker profile at different spanwise locations.*

Appendix C

Swafford profile comparison

Appendix D

Coles Law of Wake

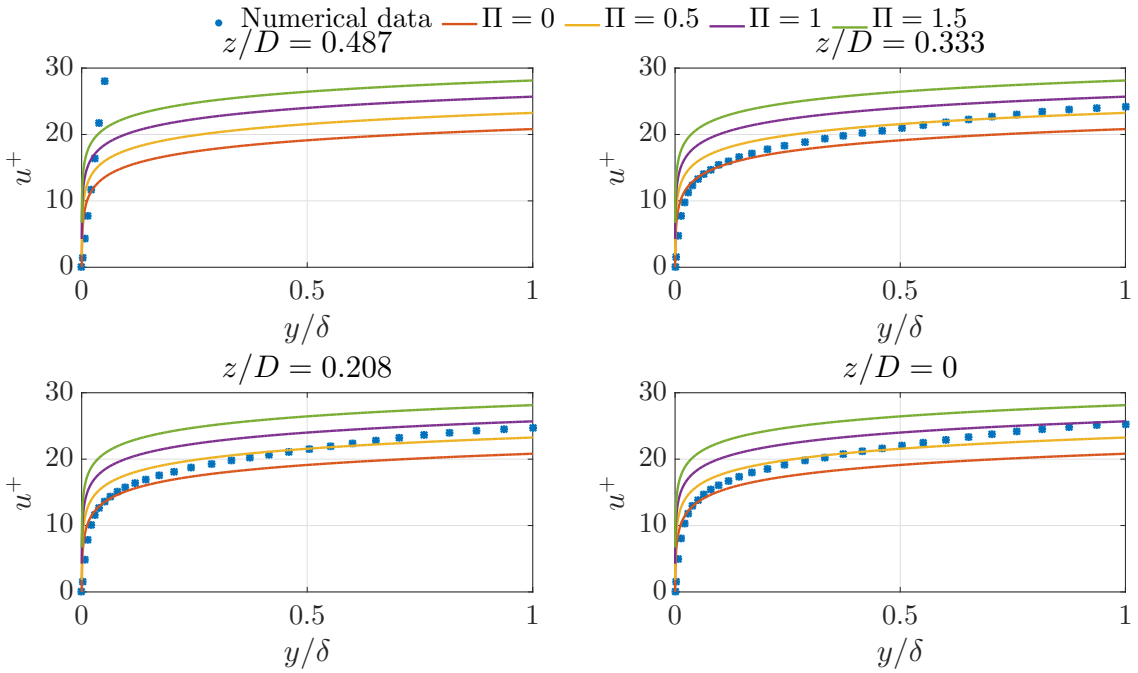

Figure D.1: *Comparison of velocity profile for VG test case [numerical dataset] at* $(x - x_{VG})/h = -10$ *with Coles' wall-wake formula at different spanwise locations.*

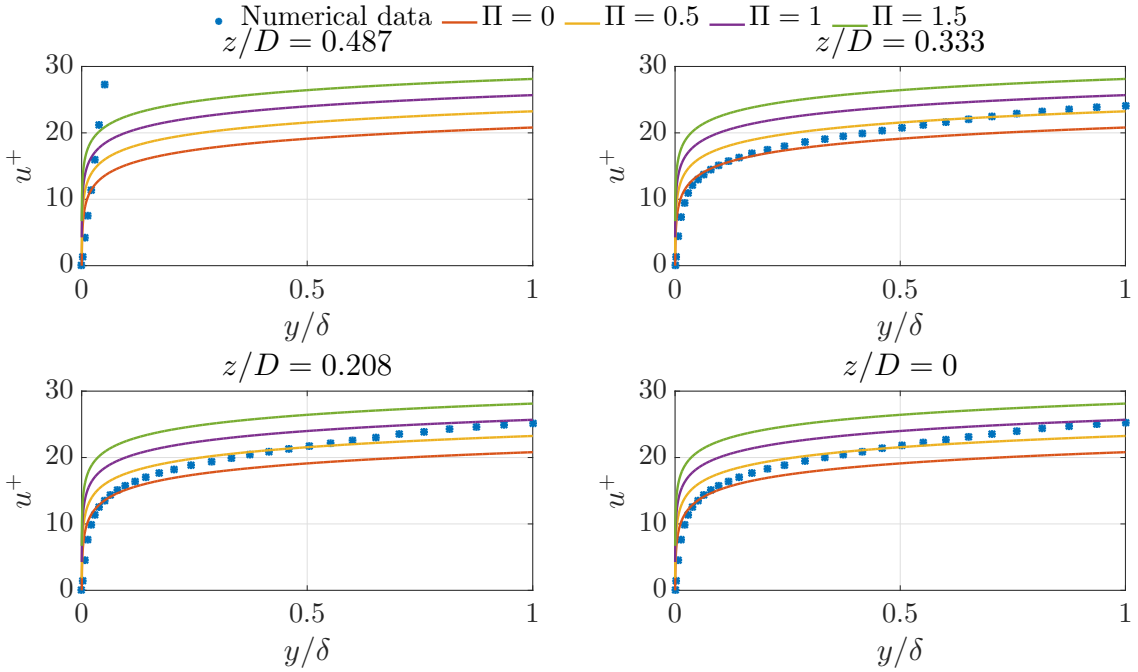

Figure D.2: *Comparison of velocity profile for VG test case [numerical dataset] at* $(x - x_{VG})/h = -5$ *with Coles' wall-wake formula at different spanwise locations.*

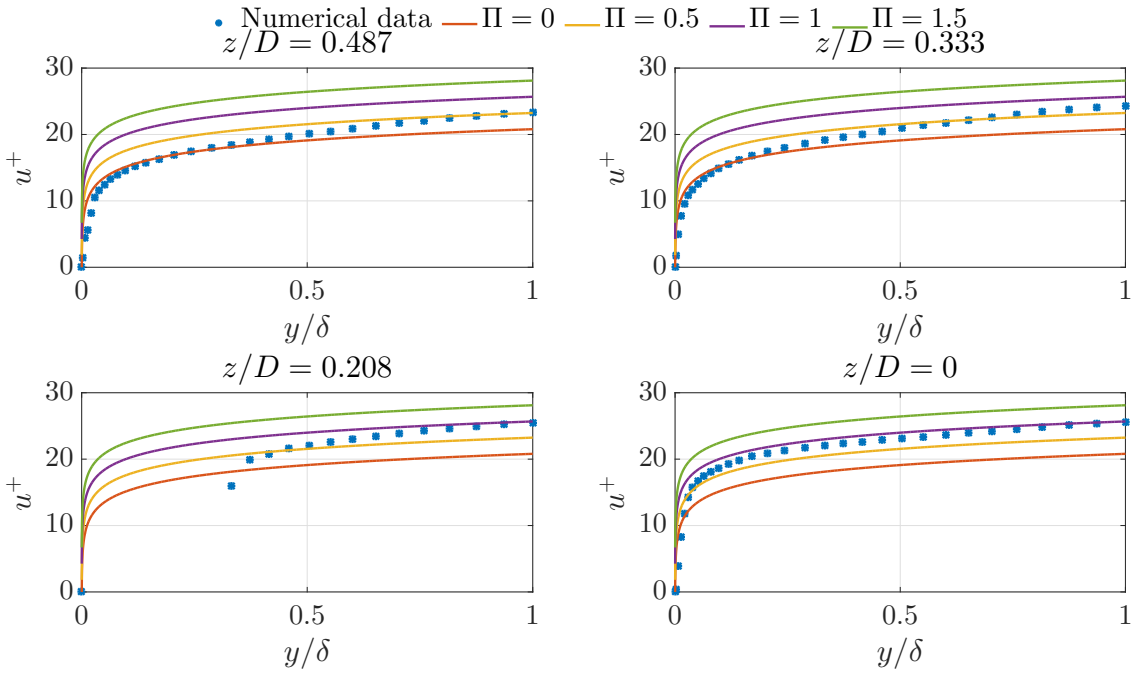

Figure D.3: *Comparison of velocity profile for VG test case [numerical dataset] at* $(x - x_{VG})/h = 0$ *with Coles' wall-wake formula at different spanwise locations.*

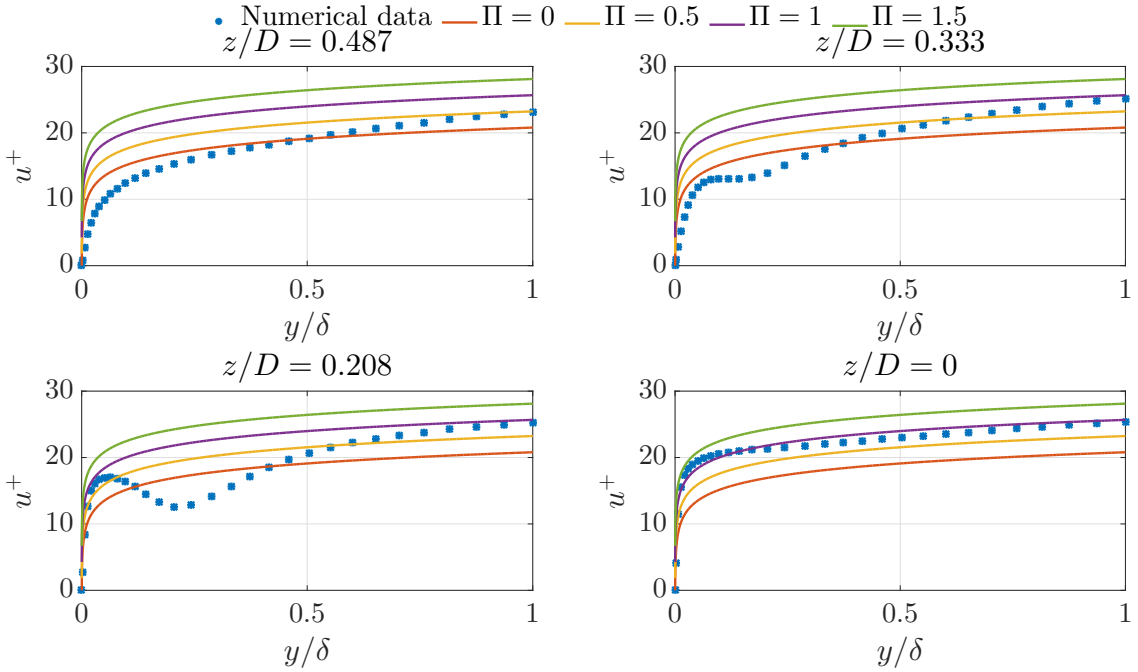

Figure D.4: *Comparison of velocity profile for VG test case [numerical dataset] at* $(x - x_{VG})/h = 5$ *with Coles' wall-wake formula at different spanwise locations.*

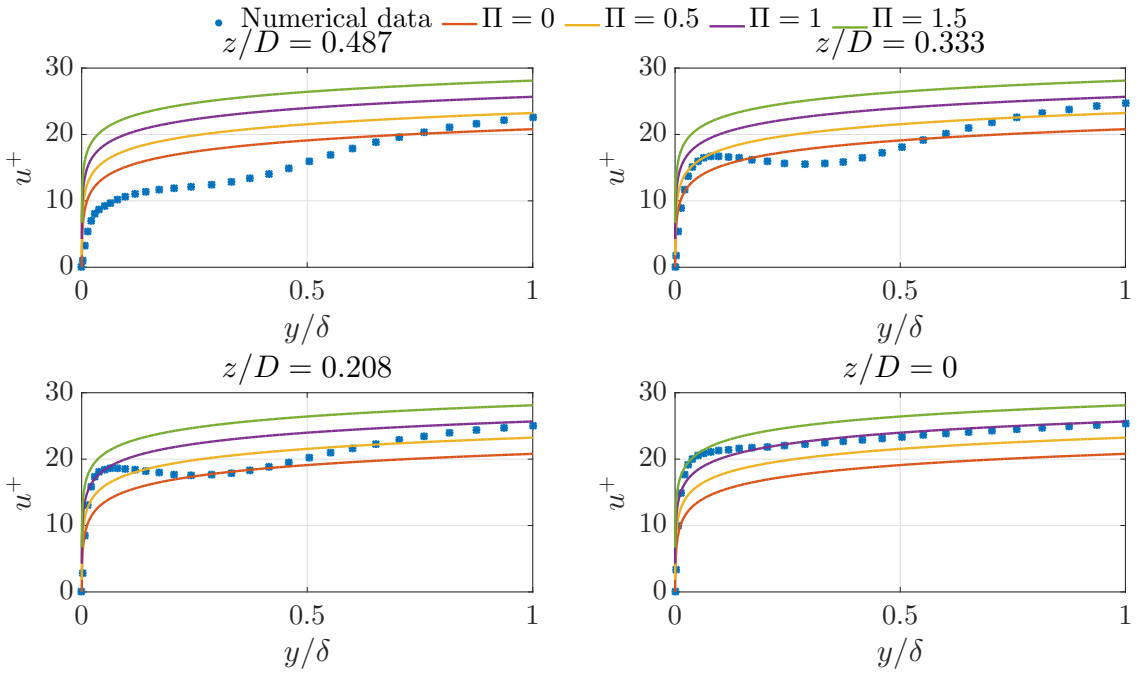

Figure D.5: *Comparison of velocity profile for VG test case [numerical dataset] at* $(x - x_{VG})/h = 15$ *with Coles' wall-wake formula at different spanwise locations.*

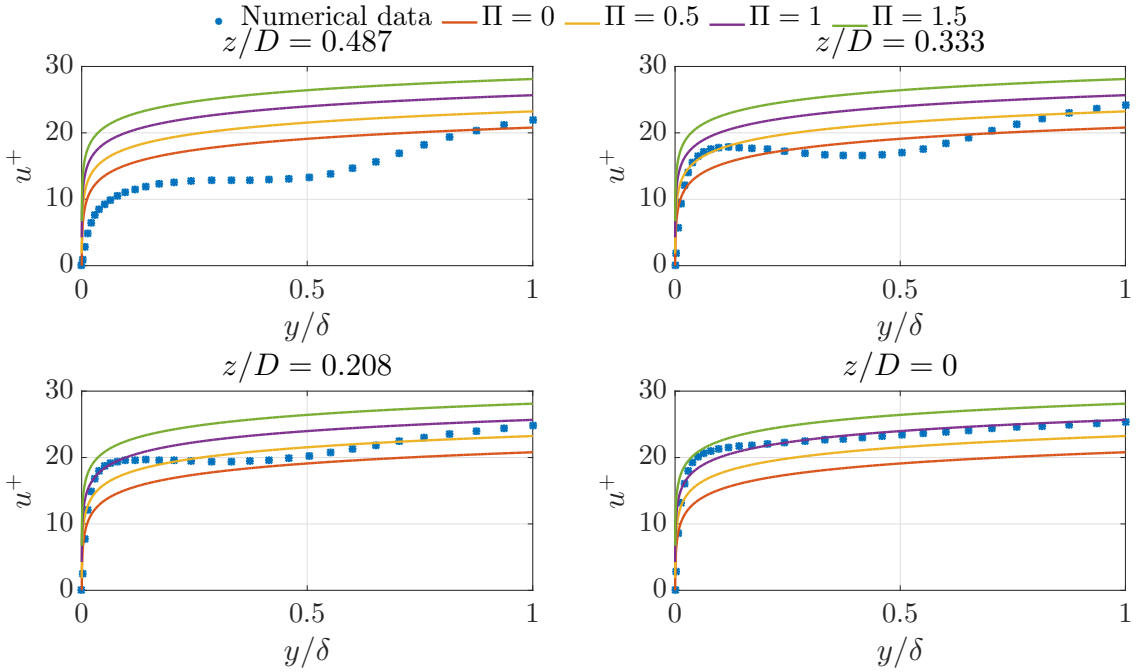

Figure D.6: *Comparison of velocity profile for VG test case [numerical dataset] at* $(x - x_{VG})/h = 25$ *with Coles' wall-wake formula at different spanwise locations.*

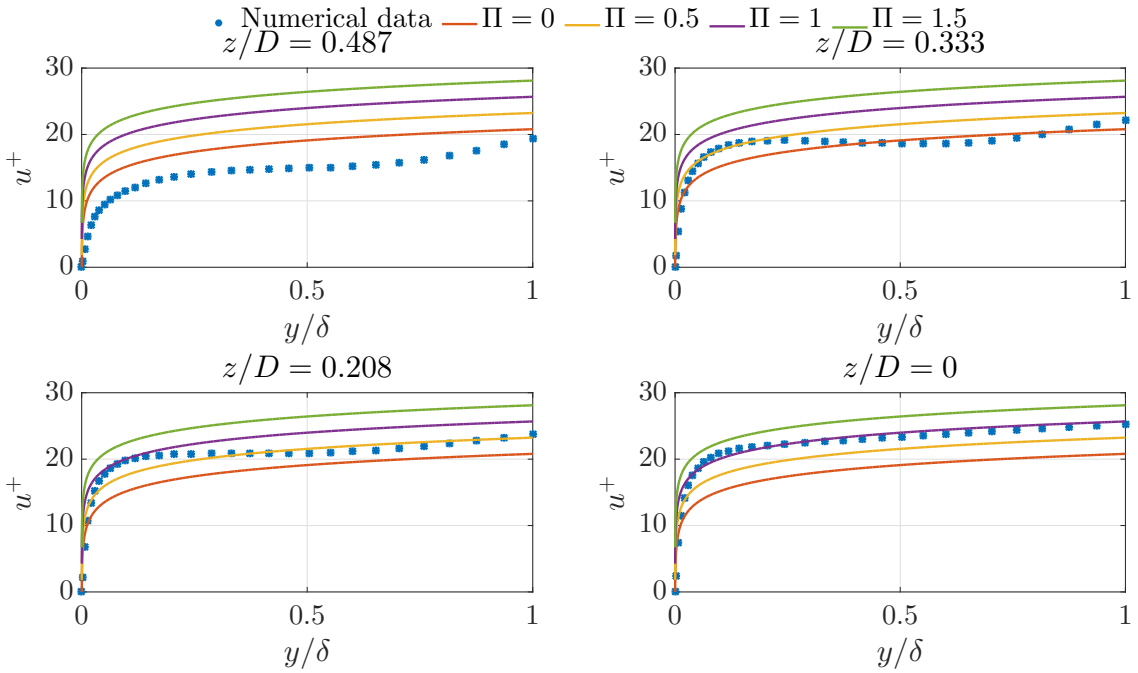

Figure D.7: *Comparison of velocity profile for VG test case [numerical dataset] at* $(x - x_{VG})/h = 50$ *with Coles' wall-wake formula at different spanwise locations.*

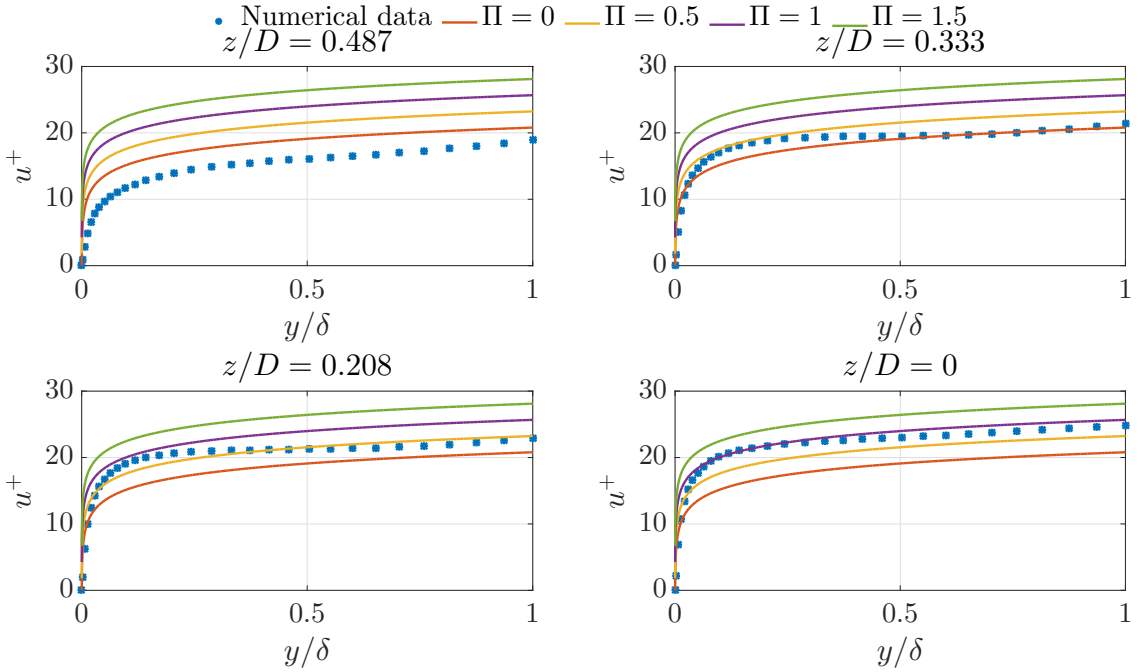

Figure D.8: *Comparison of velocity profile for VG test case [numerical dataset] at* $(x - x_{VG})/h = 75$ *with Coles' wall-wake formula at different spanwise locations.*

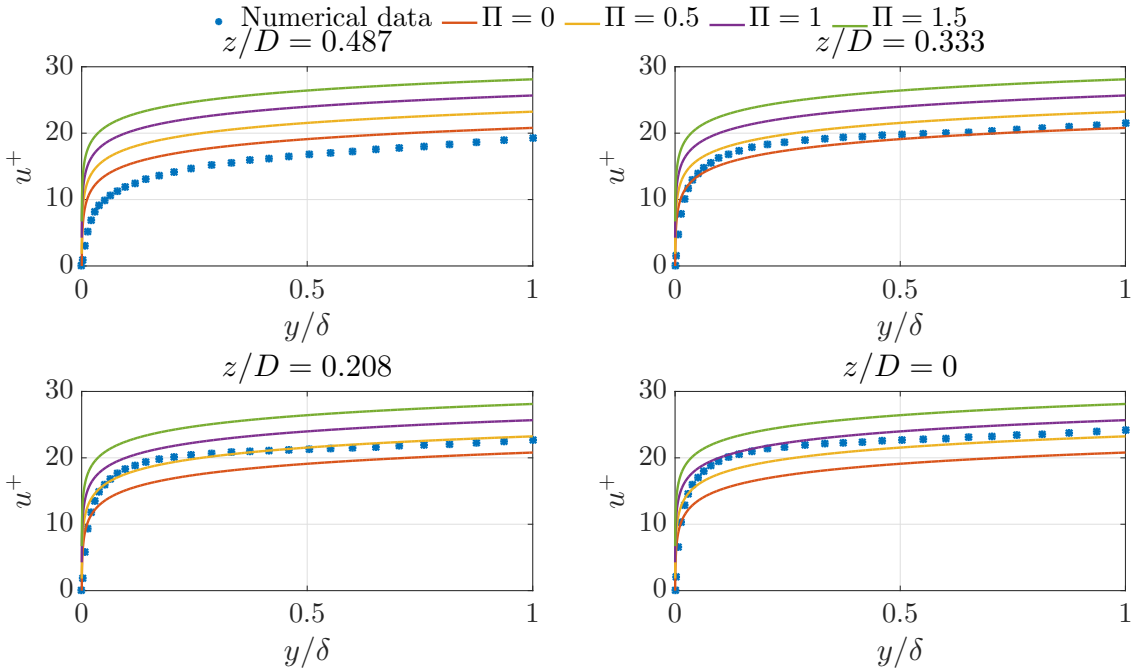

Figure D.9: *Comparison of velocity profile for VG test case [numerical dataset] at* $(x - x_{VG})/h = 100$ *with Coles' wall-wake formula at different spanwise locations.*

Appendix E

Boundary Layer Edge Velocity

U edge,

U maximum

U = 15 different plots

How it affects, somehow dissipiation from the boundary layer works out.

Also show the error with interpolation scheme.

Appendix F

Velocity, Total shear and Reynolds shear stress profile

This appendix shows the dimensionless profile of flow field around with vortex generators from the numerical dataset.

Effective slip velocity, Shear profiles,

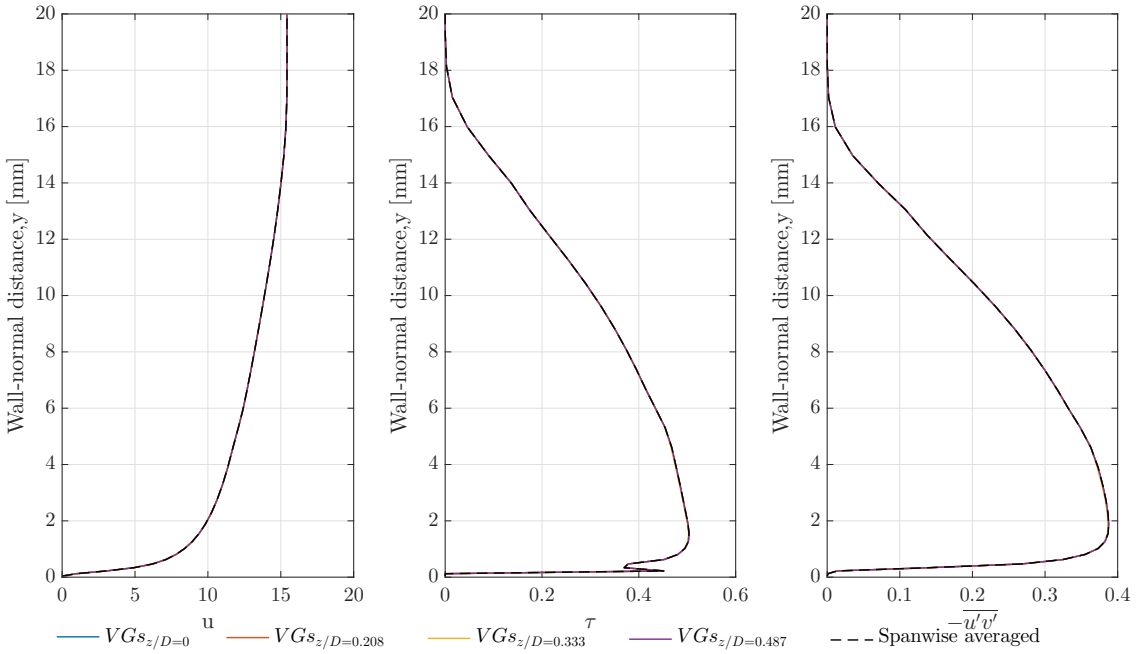

Figure F.1: *Velocity, total shear and Reynolds shear stress profile for VG test case [numerical dataset] at* $(x - x_{VG})/h = -15$ *for different spanwise locations compared with spanwise averaged profile.*

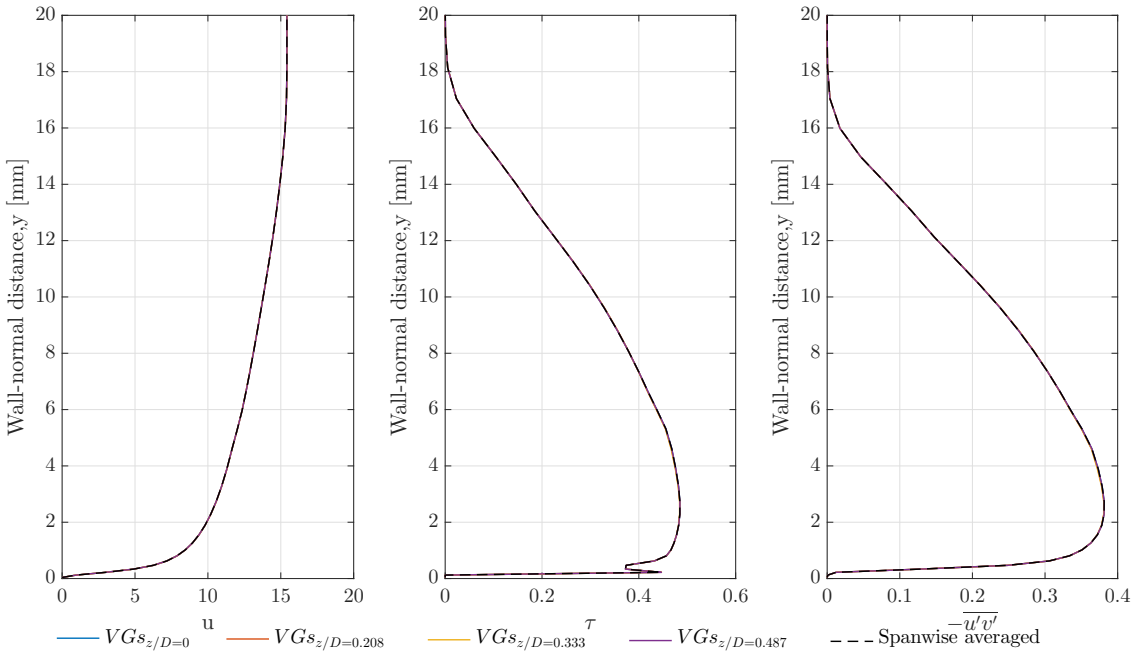

Figure F.2: *Velocity, total shear and Reynolds shear stress profile for VG test case [numerical dataset] at* $(x - x_{VG})/h = -10$ *for different spanwise locations compared with spanwise averaged profile.*

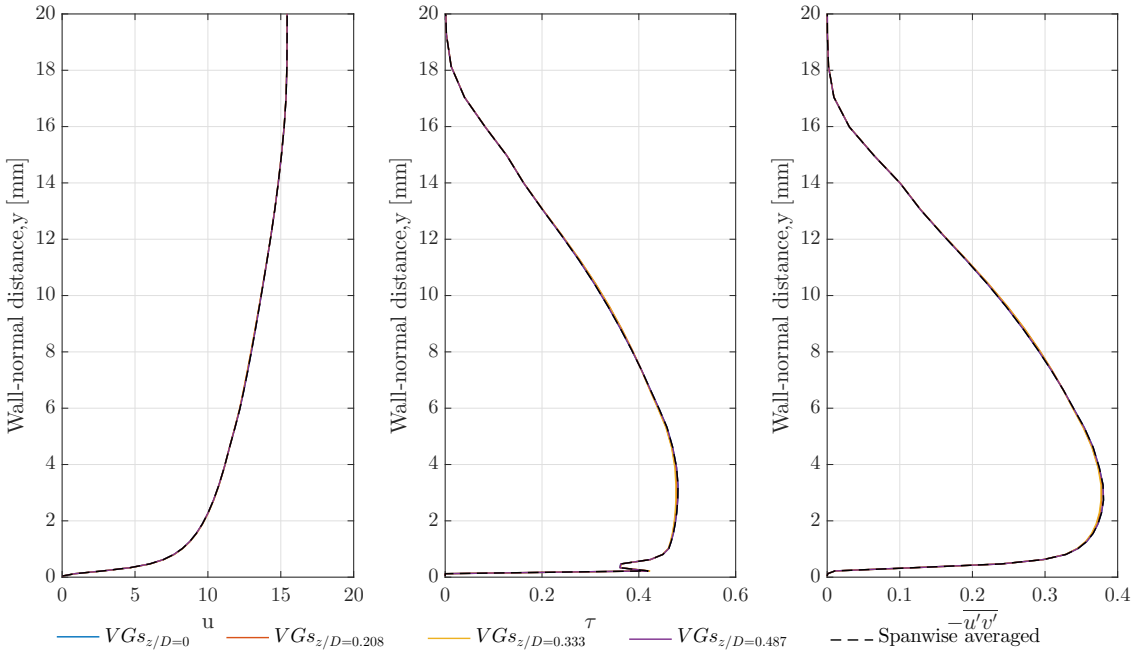

Figure F.3: *Velocity, total shear and Reynolds shear stress profile for VG test case [numerical dataset] at $(x - x_{VG})/h = -5$ for different spanwise locations compared with spanwise averaged profile.*

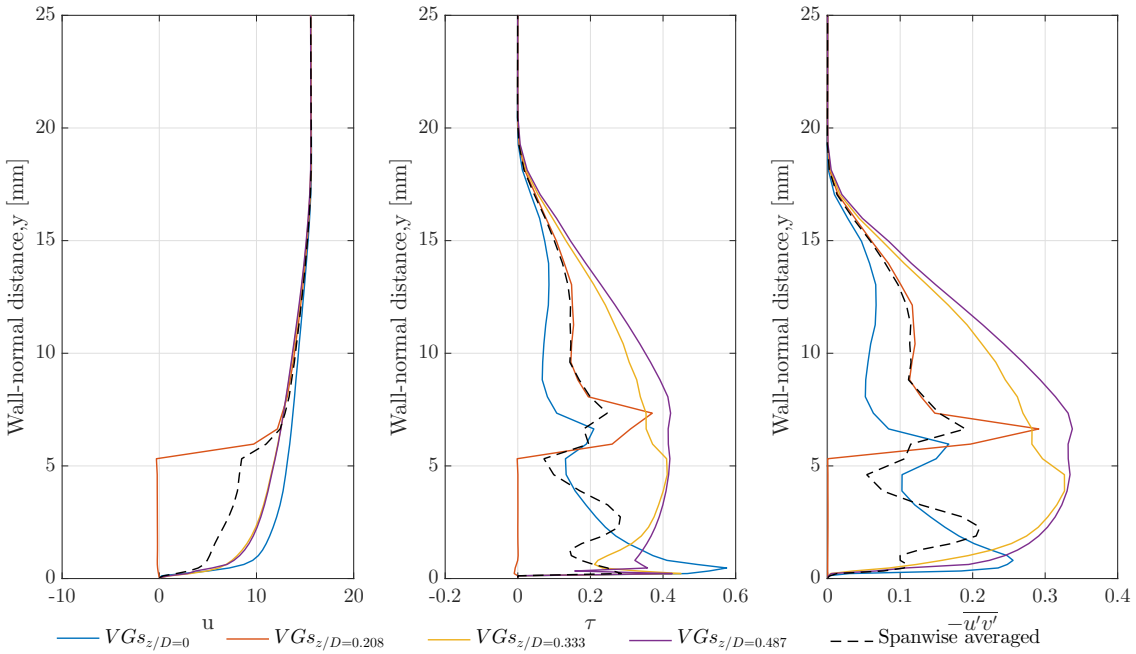

Figure F.4: *Velocity, total shear and Reynolds shear stress profile for VG test case [numerical dataset] at $(x - x_{VG})/h = 0$ for different spanwise locations compared with spanwise averaged profile.*

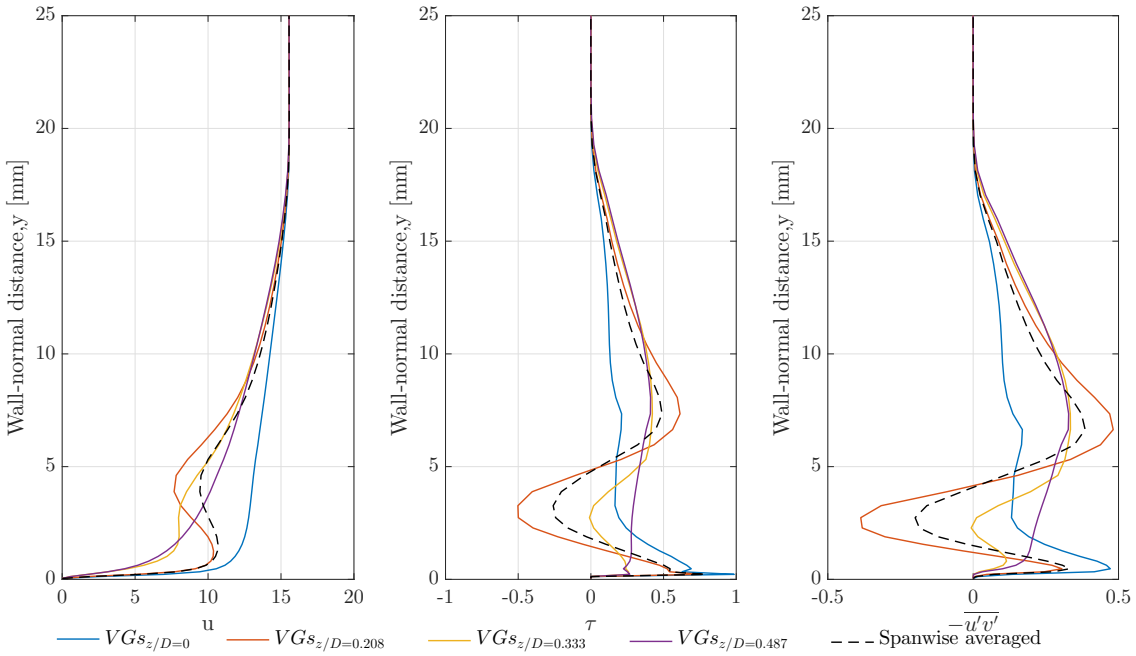

Figure F.5: *Velocity, total shear and Reynolds shear stress profile for VG test case [numerical dataset] at* $(x - x_{VG})/h = 5$ *for different spanwise locations compared with spanwise averaged profile.*

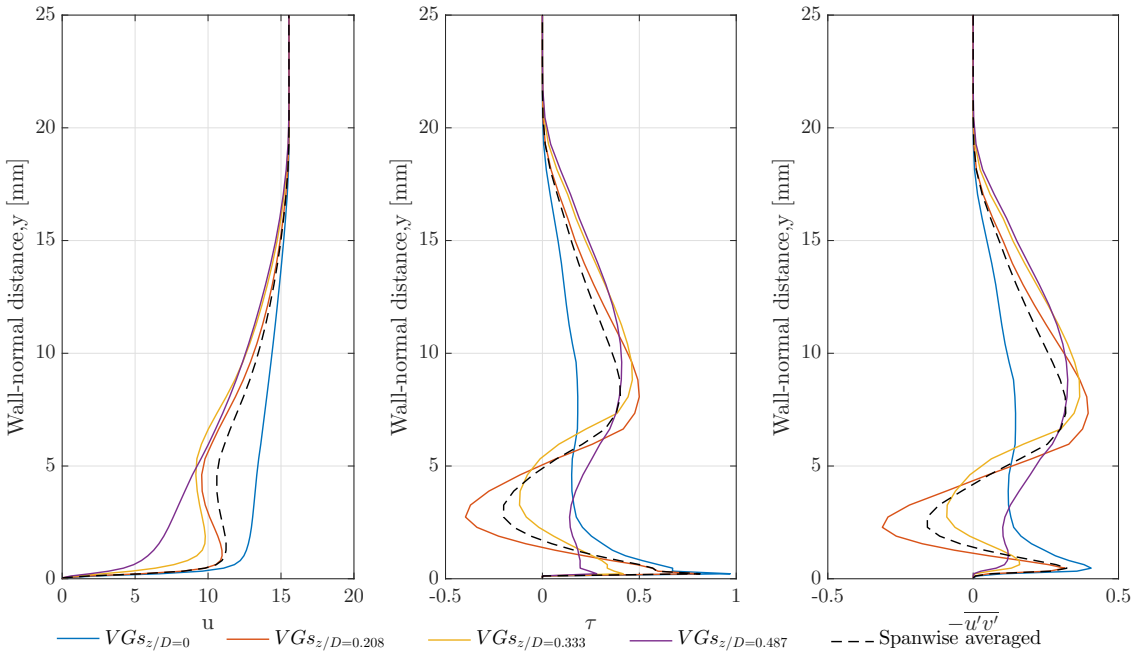

Figure F.6: *Velocity, total shear and Reynolds shear stress profile for VG test case [numerical dataset] at* $(x - x_{VG})/h = 10$ *for different spanwise locations compared with spanwise averaged profile.*

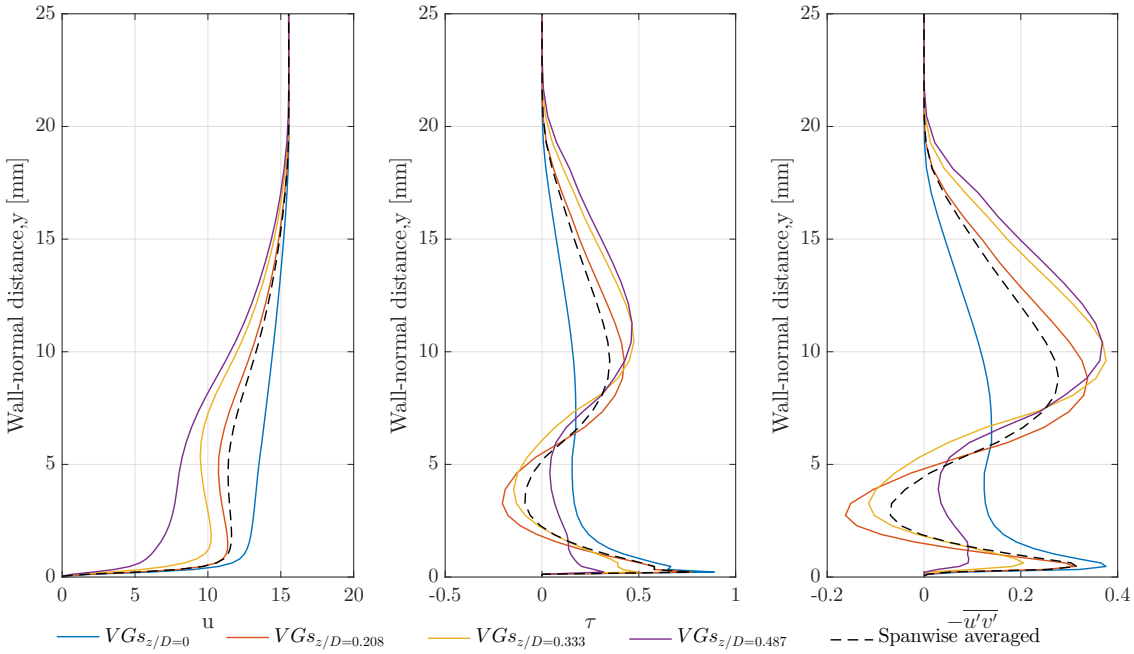

Figure F.7: *Velocity, total shear and Reynolds shear stress profile for VG test case [numerical dataset] at $(x - x_{VG})/h = 15$ for different spanwise locations compared with spanwise averaged profile.*

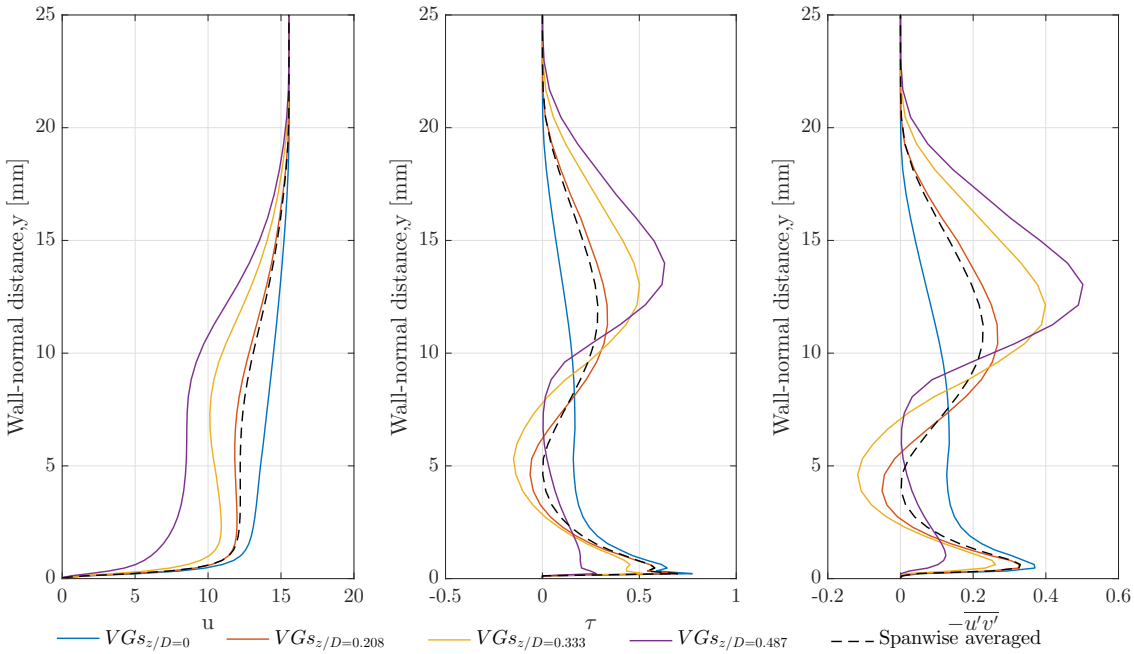

Figure F.8: *Velocity, total shear and Reynolds shear stress profile for VG test case [numerical dataset] at $(x - x_{VG})/h = 25$ for different spanwise locations compared with spanwise averaged profile.*

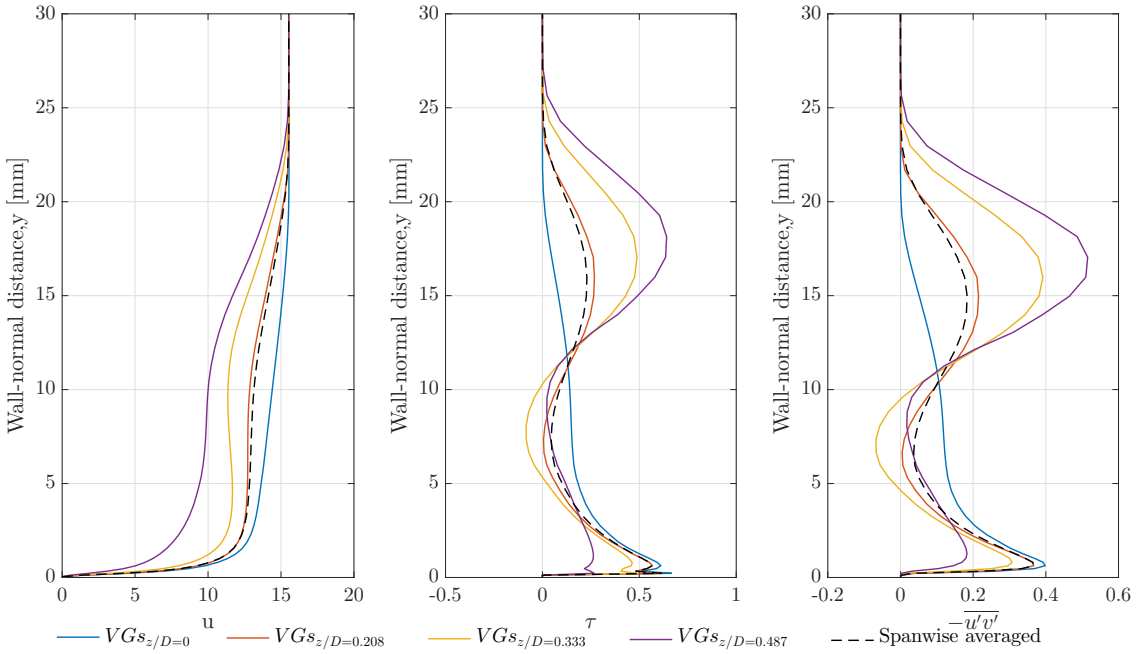

Figure F.9: *Velocity, total shear and Reynolds shear stress profile for VG test case [numerical dataset] at $(x - x_{VG})/h = 50$ for different spanwise locations compared with spanwise averaged profile.*

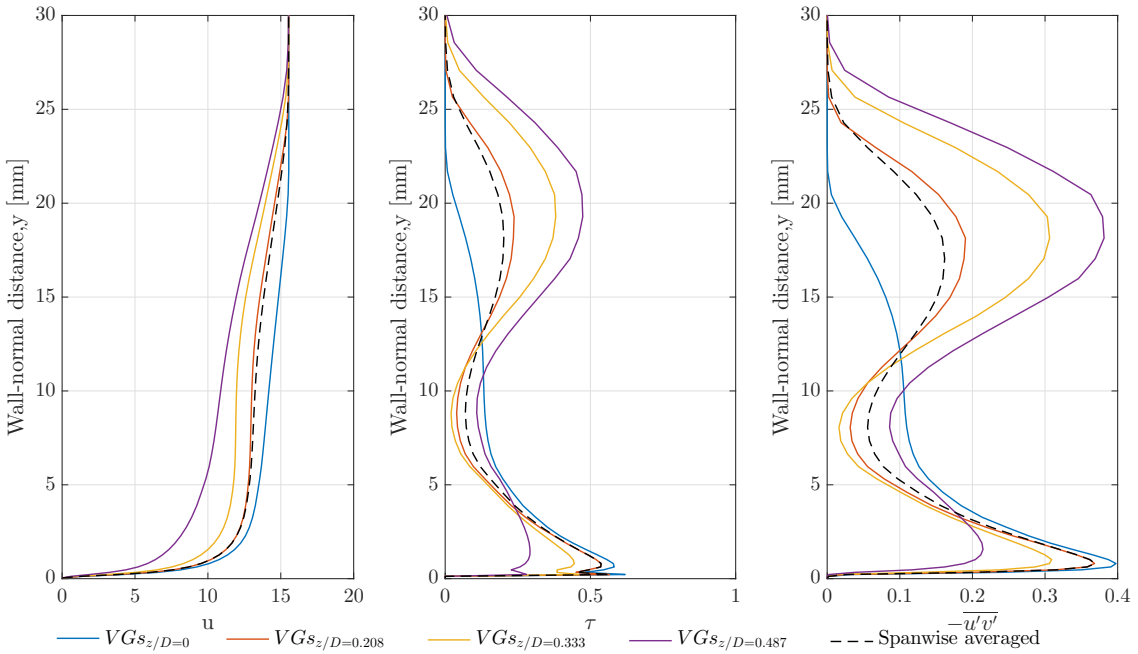

Figure F.10: *Velocity, total shear and Reynolds shear stress profile for VG test case [numerical dataset] at $(x - x_{VG})/h = 75$ for different spanwise locations compared with spanwise averaged profile.*

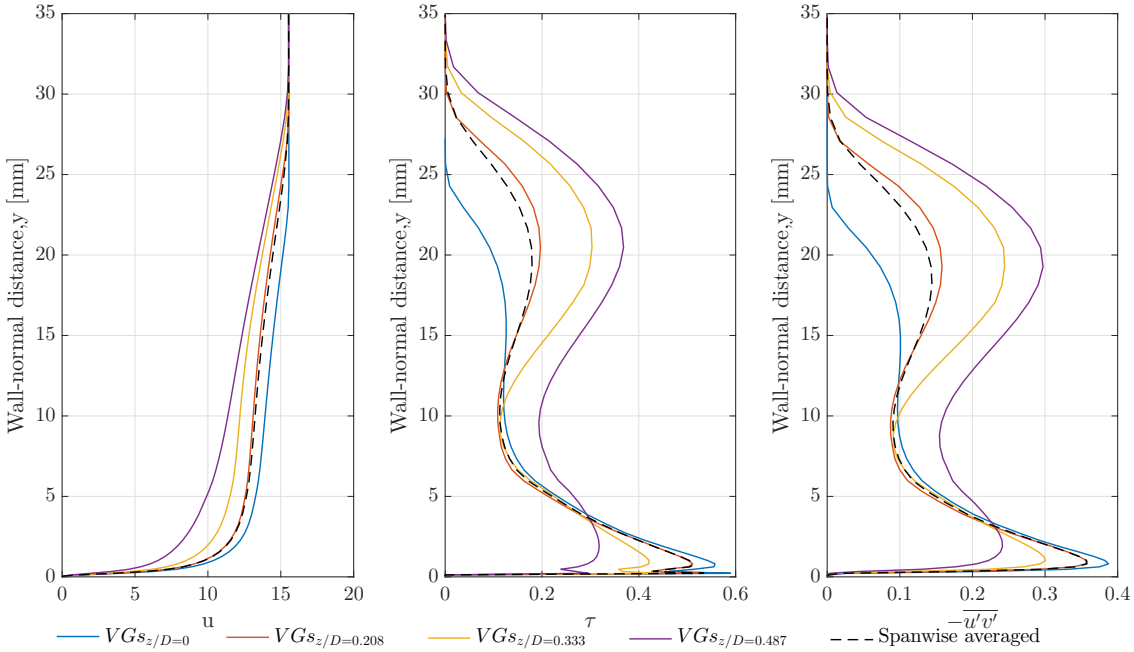

Figure F.11: *Velocity, total shear and Reynolds shear stress profile for VG test case [numerical dataset] at* $(x - x_{VG})/h = 100$ *for different spanwise locations compared with spanwise averaged profile.*

Appendix G

Wall and wake layer contribution for dissipation coefficient

This appendix shows the dimensionless profile of flow field around with vortex generators from the numerical dataset.

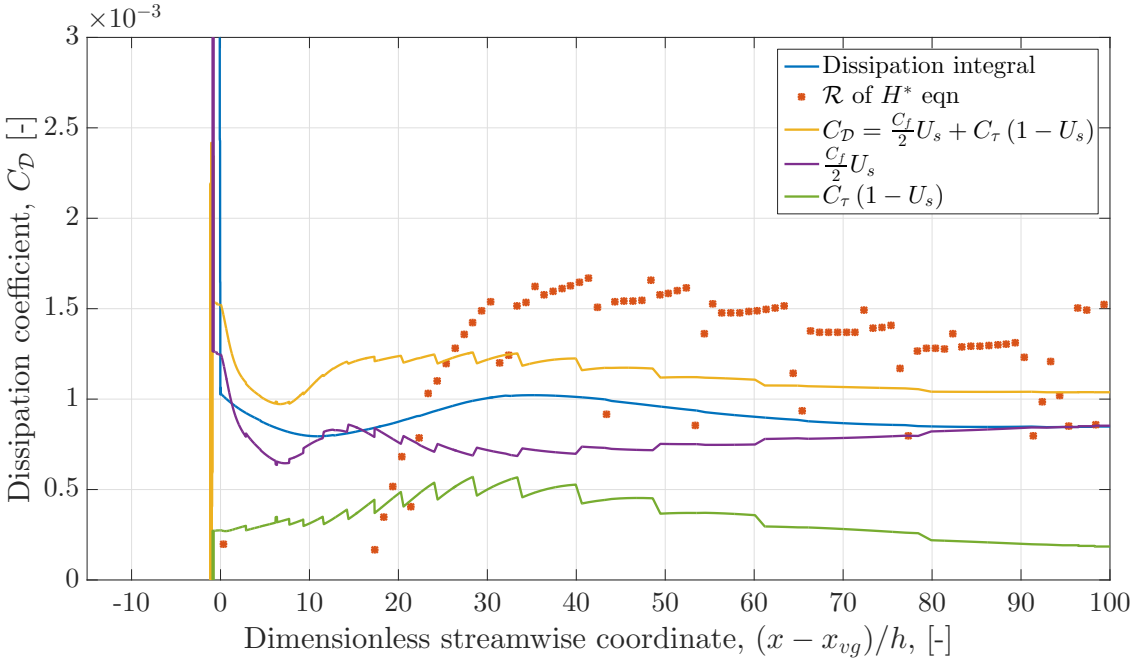

Figure G.1: *Comparison of $C_\mathcal{D}$ from dissipation integral compared with effective slip velocity method [U_s and C_τ determined from numerical dataset] at $z/D = 0.500$ in streamwise direction.*

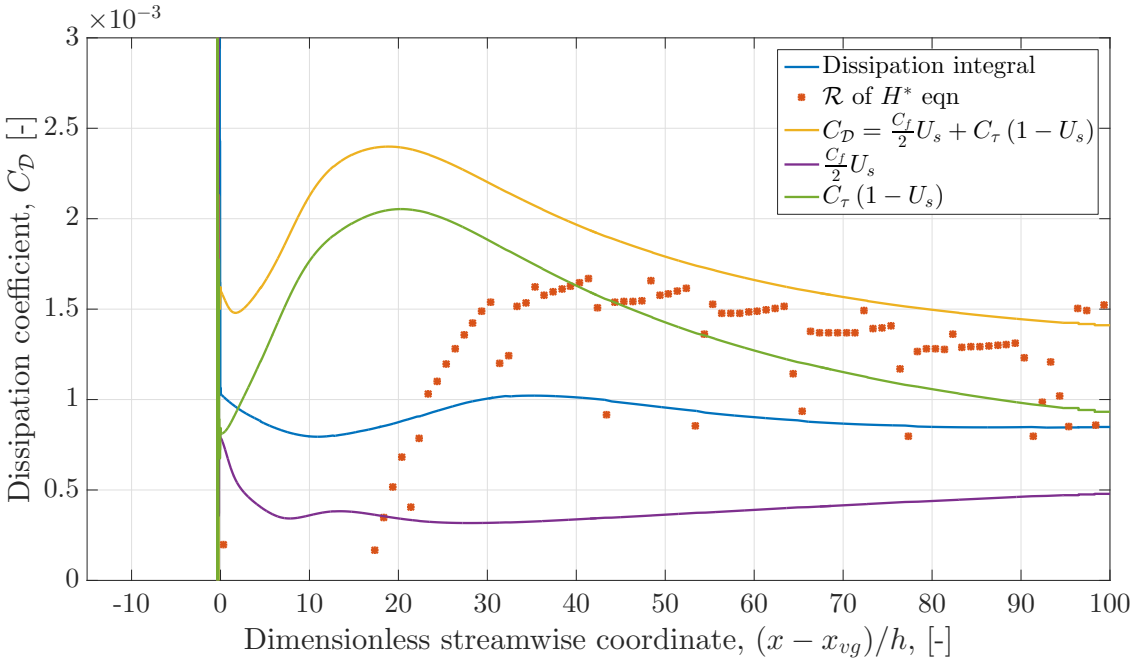

Figure G.2: *Comparison of $C_\mathcal{D}$ from dissipation integral compared with effective slip velocity method [U_s and $C_{\tau,eq}$ determined from [16] closure relations] at $z/D = 0.500$ in streamwise direction.*

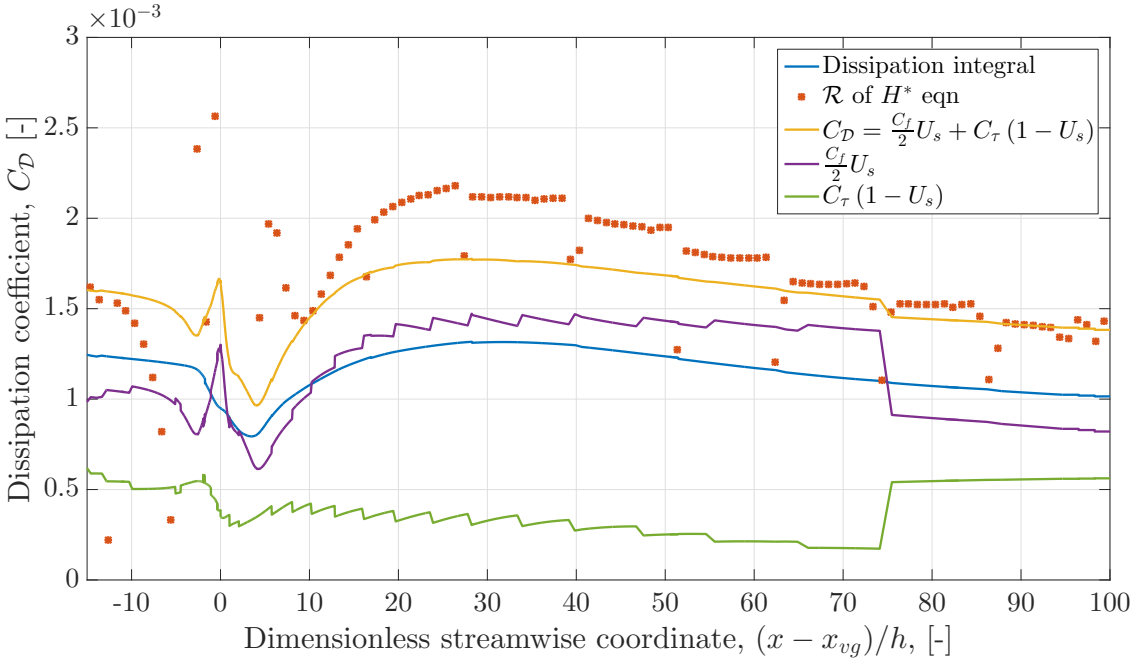

Figure G.3: *Comparison of $C_\mathcal{D}$ from dissipation integral compared with effective slip velocity method [U_s and C_τ determined from numerical dataset] at $z/D = 0.333$ in streamwise direction.*

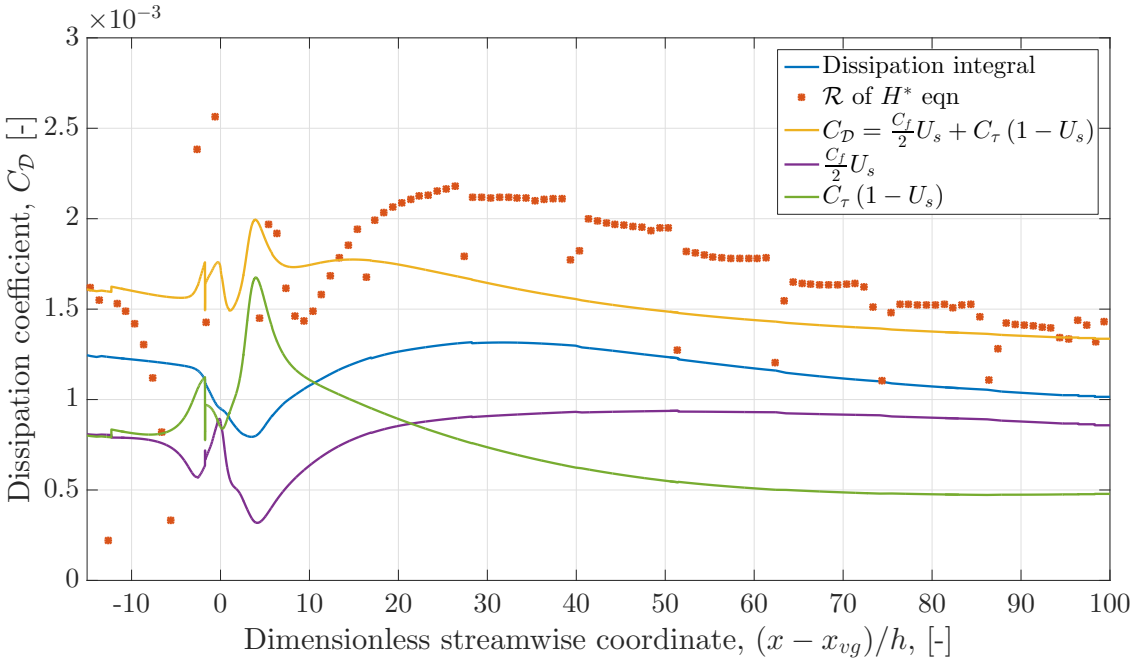

Figure G.4: *Comparison of $C_\mathcal{D}$ from dissipation integral compared with effective slip velocity method [U_s and $C_{\tau,eq}$ determined from [16] closure relations] at $z/D = 0.333$ in streamwise direction.*

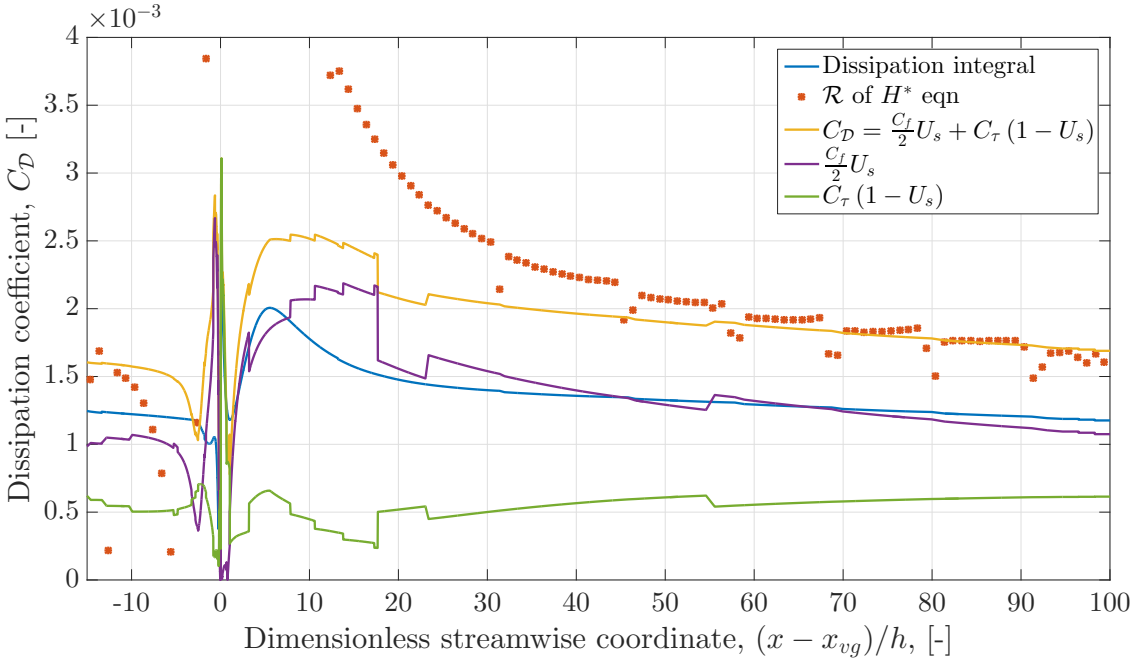

Figure G.5: *Comparison of $C_\mathcal{D}$ from dissipation integral compared with effective slip velocity method [U_s and C_τ determined from numerical dataset] at $z/D = 0.208$ in streamwise direction.*

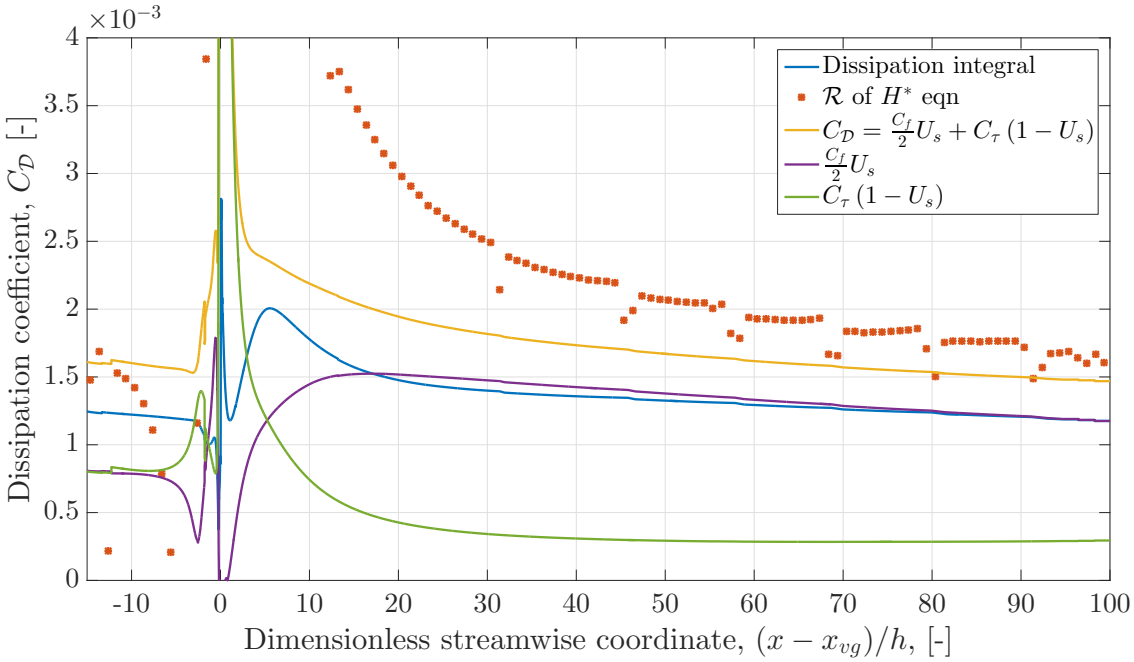

Figure G.6: *Comparison of $C_\mathcal{D}$ from dissipation integral compared with effective slip velocity method [U_s and $C_{\tau,eq}$ determined from [16] closure relations] at $z/D = 0.208$ in streamwise direction.*

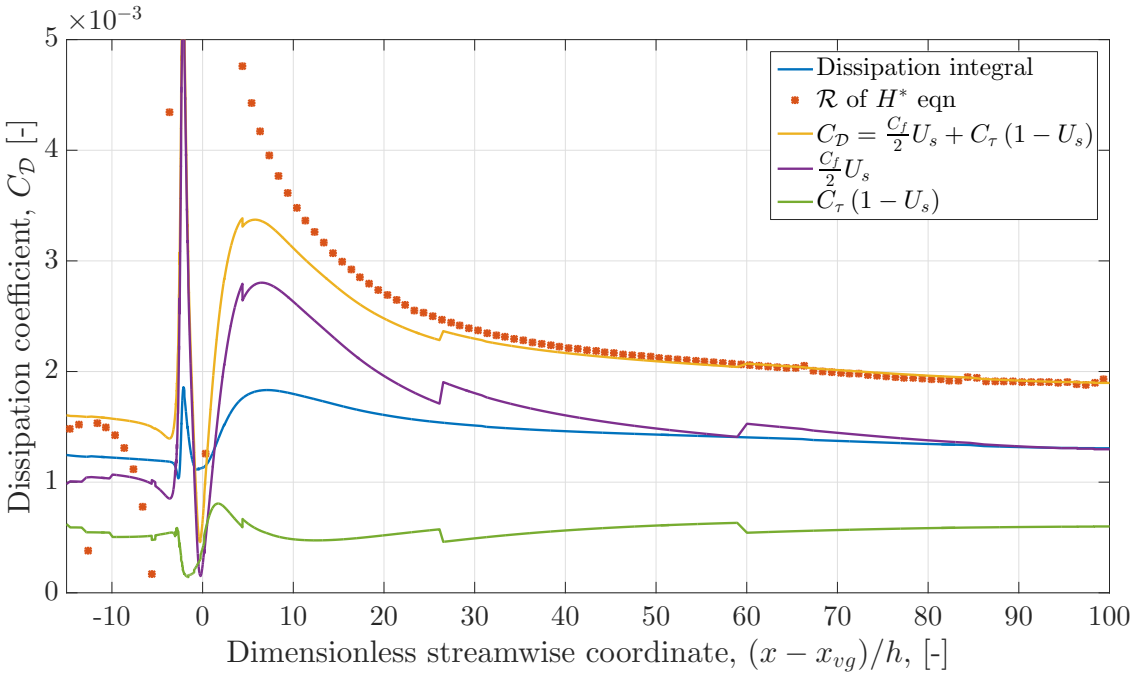

Figure G.7: *Comparison of $C_\mathcal{D}$ from dissipation integral compared with effective slip velocity method [U_s and C_τ determined from numerical dataset] at $z/D = 0$ in streamwise direction.*

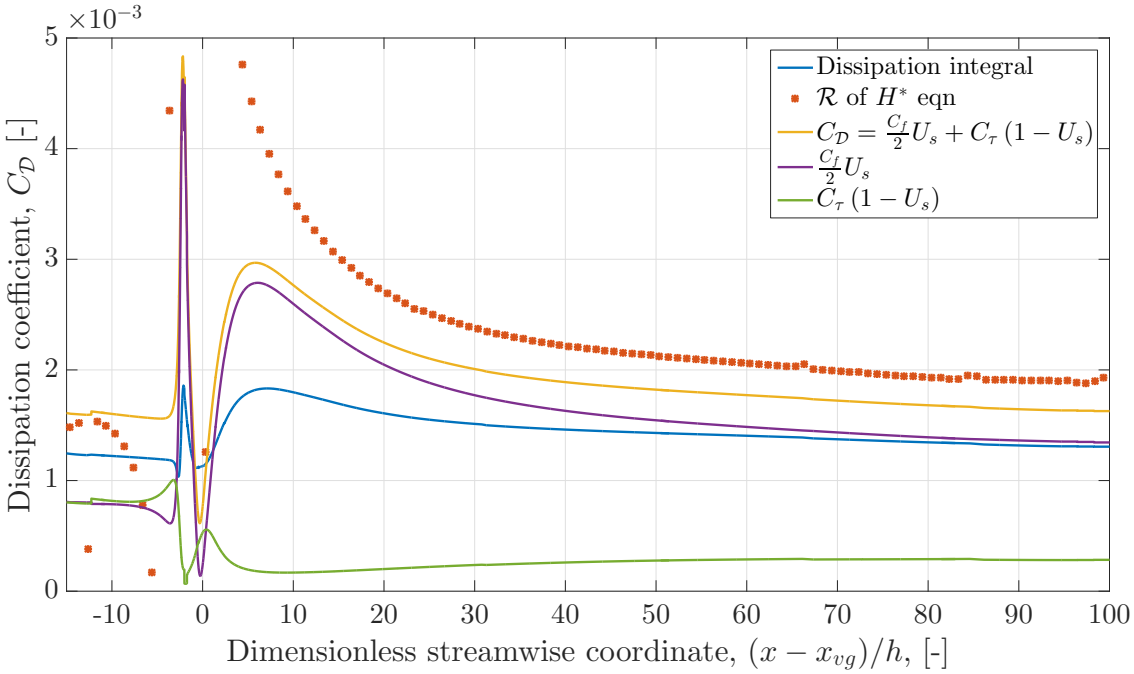

Figure G.8: *Comparison of $C_\mathcal{D}$ from dissipation integral compared with effective slip velocity method [U_s and $C_{\tau,eq}$ determined from [16] closure relations] at $z/D = 0$ in streamwise direction.*

References

[1] The global wind energy outlook, 2014.

[2] Annual Energy Outlook 2015. Levelized cost and levelized avoided cost of new generation resources in the annual energy outlook 2015. Technical report, U.S Energy Information Administration, April 2015.

[3] Patrick R Ashill, John L Fulker, and Kevin C Hackett. Research at dera on sub boundary layer vortex generators(sbvgs). In *AIAA, Aerospace Sciences Meeting and Exhibit, 39 th, Reno, NV*, 2001.

[4] PR Ashill, JL Fulker, and KC Hackett. Studies of flows induced by sub boundary layer vortex generators (sbvgs). *AIAA paper*, 968:2002, 2002.

[5] PR Ashill, JL Fulker, and KC Hackett. A review of recent developments in flow control. *Aeronautical Journal*, 109(1095):205–232, 2005.

[6] Daniel Baldacchino, Daniele Ragni, Carlos Simao Ferreira, and Gerard van Bussel. Towards integral boundary layer modelling of vane-type vortex generators. In *45th AIAA Fluid Dynamics Conference*, page 3345, 2015.

[7] DW Bechert, M Bruse, W Hage, and R Meyer. Fluid mechanics of biological surfaces and their technological application. *Naturwissenschaften*, 87(4):157–171, 2000.

[8] Peter Bradshaw, DH Ferriss, and NP Atwell. Calculation of boundary-layer development using the turbulent energy equation. *Journal of Fluid Mechanics*, 28(03): 593–616, 1967.

[9] Matthias Buschmann. Calculation of turbulent boundary layers using the dissipation integral method. *Journal of Thermal Science*, 8(4):223–230, 1999.

[10] Tuncer Cebeci and A.M.O. Smith. *Analysis of turbulent boundary layers*, volume 15. Elsevier, 1974.

[11] Francis H Clauser. Turbulent boundary layers in adverse pressure gradients. *Journal of the Aeronautical Sciences*, 21(2), 1954.

[12] DE Coles. Computation of turbulent boundary layers. In *1968 AFOSR-IFP-Stanford Conference Proceedings, Vol.2, Stanford Univ*, 1968.

[13] Donald Coles. The law of the wake in the turbulent boundary layer. *Journal of Fluid Mechanics*, 1(02):191–226, 1956.

[14] Mark Drela. Xfoil: An analysis and design system for low reynolds number airfoils. In *Low Reynolds number aerodynamics*, pages 1–12. Springer, 1989.

[15] Mark Drela. *Flight vehicle aerodynamics*. MIT Press, 2014.

[16] Mark Drela and Michael B Giles. Viscous-inviscid analysis of transonic and low reynolds number airfoils. *AIAA journal*, 25(10):1347–1355, 1987.

[17] Engineering Sciences Data Unit ESDU. Transonic data memorandum, vortex generators for control of shock-induced separation, part 1 introduction and aerodynamics, 1993.

[18] L Florentie, AH Van Zuijlen, and H Bijl. Towards a multi-fidelity approach for cfd simulations of vortex generator arrays. In *Proceedings-WCCM XI: 11th World Congress on Computational Mechanics; ECCM V: 5th European Conference on Computational Mechanics; ECFD VI: 6th European Conference on Computational Fluid Dynamics, Barcelona, Spain, 20-25 July 2014*, 2014.

[19] Koji Fukagata, Kaoru Iwamoto, and Nobuhide Kasagi. Contribution of reynolds stress distribution to the skin friction in wall-bounded flows. *Physics of Fluids (1994-present)*, 14(11):L73–L76, 2002.

[20] Néstor Ramos García. *Unsteady viscous-inviscid interaction technique for wind turbine airfoils*. PhD thesis, Ph. D. thesis, Technical university of Denmark, 2011.

[21] Mac Gaunaa, Christian Bak, et al. The effect of mounting vortex generators on the dtu 10mw reference wind turbine blade. In *Journal of Physics: Conference Series*, page 012034. IOP Publishing, 2014.

[22] Gilles Godard and Michel Stanislas. Control of a decelerating boundary layer. part 1: Optimization of passive vortex generators. *Aerospace Science and Technology*, 10 (3):181–191, 2006.

[23] JE Green, DJ Weeks, and JWF Brooman. Prediction of turbulent boundary layers and wakes in compressible flow by a lag-entrainment method. Technical report, Aeronautical Research Council, London, 1973.

[24] Th v Kármán. Über laminare und turbulente reibung. *ZAMM-Journal of Applied Mathematics and Mechanics/Zeitschrift für Angewandte Mathematik und Mechanik*, 1(4):233–252, 1921. English translation in NACA Technical Memo. 1092.

[25] Anthony Kendall and Manoochehr Koochesfahani. A method for estimating wall friction in turbulent wall-bounded flows. *Experiments in Fluids*, 44(5):773–780, 2008.

[26] Michael Kerho, Brian Kramer, and CA Torrance. Enhanced airfoil design incorporating boundary layer mixing devices. *AIAA Paper*, 211:2003, 2003.

[27] JC Le Balleur. Strong matching method for computing transonic viscous flows including wakes and separations. *La Recherche Aerospatiale*, 1981.

[28] L. S. Leibenson. The energy form of the integral condition in the theory of the boundary layer. *Doklady Akademii Nauk SSSR*, 1935.

[29] John C Lin. Review of research on low-profile vortex generators to control boundary-layer separation. *Progress in Aerospace Sciences*, 38(4):389–420, 2002.

[30] John C Lin, Gregory V Selby, and Floyd G Howard. Exploratory study of vortex-generating devices for turbulent flow separation control. *AIAA paper*, 42, 1991.

[31] Ola Lögdberg, Jens HM Fransson, and P Henrik Alfredsson. Streamwise evolution of longitudinal vortices in a turbulent boundary layer. *Journal of Fluid Mechanics*, 623:27–58, 2009.

[32] H Ludwieg and W Tillmann. Untersuchungen über die wandschubspannung in turbulenten reibungsschichten. *Archive of Applied Mechanics*, 17(4):288–299, 1949. English translation in NACA Technical Memo. 1285.

[33] MATLAB. *MATLAB*. The MathWorks, Inc., Natick, Massachusetts, United States, academic use (r2015b) edition, 2015.

[34] Doug McLean. *Understanding aerodynamics: arguing from the real physics*. John Wiley & Sons, 2012.

[35] AJ Musker. Explicit expression for the smooth wall velocity distribution in a turbulent boundary layer. *AIAA Journal*, 17(6):655–657, 1979.

[36] Hassan Nagib, Chris Christophorou, JD Rüedi, PA Monkewitz, and JM Österlund. Can we ever rely on results from wall-bounded turbulent flows without direct measurements of wall shear stress. *AIAA paper*, 2392, 2004.

[37] TB Nickels. Inner scaling for wall-bounded flows subject to large pressure gradients. *Journal of Fluid Mechanics*, 521:217–239, 2004.

[38] IG Nikolaou, ES Politis, and PK Chaviaropoulos. Modelling the flow around airfoils equipped with vortex generators using a modified 2d navier–stokes solver. *Journal of solar energy engineering*, 127(2):223–233, 2005.

[39] Ramis Örlü, Jens HM Fransson, and P Henrik Alfredsson. On near wall measurements of wall bounded flowsthe necessity of an accurate determination of the wall position. *Progress in Aerospace Sciences*, 46(8):353–387, 2010.

[40] Jens M Österlund. *Experimental studies of zero pressure-gradient turbulent boundary layer flow*. PhD thesis, Royal Institute of Technology, Department of Mechanics, 1999.

[41] Jens M Österlund, Arne V Johansson, Hassan M Nagib, and Michael H Hites. A note on the overlap region in turbulent boundary layers. *Physics of Fluids (1994-present)*, 12(1):1–4, 2000.

[42] S Øye. The effect of vortex generators on the performance of the elkraft 1000 kw turbine. In *9th IEA Symposium on Aerodynamics of Wind Turbines, Stockholm, ISSN*, pages 0590–8809, 1995.

[43] Martin J. Pasqualetti, Robert Righter, and Paul Gipe. Wind energy, history of. In Cutler J. Cleveland, editor, *Encyclopedia of Energy*, pages 419 – 433. Elsevier, New York, 2004. ISBN 978-0-12-176480-7.

[44] Eduardo Rodríguez-López, Paul JK Bruce, and Oliver RH Buxton. A robust post-processing method to determine skin friction in turbulent boundary layers from the velocity profile. *Experiments in Fluids*, 56(4):1–16, 2015.

[45] Galen Brandt Schubauer and WG Spangenberg. Forced mixing in boundary layers. *Journal of Fluid Mechanics*, 8(01):10–32, 1960.

[46] DB Spalding. A single formula for the law of the wall. *Journal of Applied Mechanics*, 28(3):455–458, 1961.

[47] Florian Von Stillfried, Stefan Wallin, and Arne V Johansson. Vortex-generator models for zero-and adverse-pressure-gradient flows. *AIAA journal*, 50(4):855–866, 2012.

[48] Timothy L Sullivan. Effect of vortex generators on the power conversion performance and structural dynamic loads of the mod-2 wind turbine. Technical report, National Aeronautics and Space Administration, Cleveland, OH (USA). Lewis Research Center, 1984.

[49] TW Swafford. Analytical approximation of two-dimensional separated turbulent boundary-layer velocity profiles. *AIAA journal*, 21(6):923–926, 1983.

[50] HD Taylor. Increasing the efficiency of the uac 8-ft wind tunnel fan by means of vortex generators. Technical report, Technical Report R-4012-4, UAC, 1947.

[51] JL Thomas. Integral boundary-layer models for turbulent separated flows. In *17th Fluid Dynamics, Plasma Dynamics, and Lasers Conference*, volume 1, 1984.

[52] Neil Titchener, Simon Colliss, and Holger Babinsky. On the calculation of boundary-layer parameters from discrete data. *Experiments in Fluids*, 56(8):1–18, 2015.

[53] Erich Truckenbrodt. A method of quadrature for calculation of the laminar and turbulent boundary layer in case of plane and rotationally symmetrical flow. Technical report, NACA Tech. Memo. No. 1379, 1955.

[54] Clara Marika Velte. *Characterization of vortex generator induced flow*. PhD thesis, Technical University of Denmark (DTU), 2009.

[55] Frank M White. *Viscous Fluid Flow*, volume 3. McGraw-Hill New York, 2006.

[56] David L Whitfield. Integral solution of compressible turbulent boundary layers using improved velocity profiles. Technical report, DTIC Document, 1978.

[57] DL Whitfield, TW Swafford, and JL Jacocks. Calculation of turbulent boundary layers with separation and viscous-inviscid interaction. *AIAA Journal*, 19(10):1315–1322, 1981.

End of document